Characterization of the human prion protein in its native-like state

Inaugural dissertation

for the attainment of the title of doctor
in the Faculty of Mathematics and Natural Sciences
at the Heinrich-Heine-Universität Düsseldorf

presented by

Najoua Bolakhrif

from Düsseldorf, Germany

Düsseldorf, January 2023

From the Institut für Physikalische Biologie at the Heinrich-Heine-Universität Düsseldorf

Published by permission of the Faculty of Mathematics and Natural Sciences at Heinrich-Heine-Universität Düsseldorf

Supervisor:

1. Prof. Dr. Dieter Willbold
2. Junior Prof. Dr. Wolfgang Hoyer

Date of the oral examination: 27th of January, 2023

Declaration

I declare under oath that I have compiled this dissertation independently and without any undue assistance by third parties under consideration of the "Fundamental principles for safeguarding good scientific practice at Heinrich-Heine-Universität Düsseldorf". Furthermore, neither this dissertation, nor a similar work, has been submitted to another faculty. I have not made any unsuccessful attempt to obtain a doctorate.

Düsseldorf, January 2, 2023

Najoua Bolakhrif

Acknowledgement

Firstly, would like to thank Prof. Dr. Dieter Willbold for the opportunity to work on this project and for the unconditional support when needed, the pragmatic results and the availability regardless of the day and time. He provided two institutes where I felt more than comfortable to work and develop.

Secondly, I would like to thank Jun. Prof. Dr. Wolfgang Hoyer as my mentor and second supervisor, who has an open ear not only for me but for everyone and offers his help when it is needed.

I thank Dr. Lothar Gremer for the original idea of the *Leishmania tarentolae* project and the many freedoms. I also thank him for his support in the laboratory.

I am grateful for the collaboration with Dr. Luitgard Nagel-Steger and the restful dinners. In addition to the fruitful discussions, her support in correcting the first versions of the polymorphism and *Leishmania tarentolae* manuscripts was indispensable and involved a lot of patience from her side and useful advice. Thanks to Prof. Dr. Holger Gohlke and Jesko Kaiser who helped to build a more complete picture of the polymorphism project.

I would like to thank Robin Backer, Joanna Zeyer, and Linda Reinecke for being fantastic office mates and great technical support in the lab. I am also thankful for the time outside of the lab, including coffee breaks, fishing trips, and dance classes.

Un grand merci à Luis Gardon, qui a été à mes côtés et a rendu mon séjour à l'IPB plus agréable.

To my delight, Lora Denson and Bianca Axinte have gone from being nice colleagues to good friends during my time at the IPB.

Dr. Emil Dandanell Agerschou has also been a great support in many ways, starting with my undergraduate studies, and still has a listening ear for me when I need it. I know I can always count on Bisfis and would never want to miss it.

Dr. Thomas Pauly is most likely the one with whom I may most closely associate this work. He is much more than a best friend and collaborator, so it is hard to express my gratitude in these few lines; not even the pages of 'Physical Biology of the Cell' would give me the space I need to say how lucky I am that he is such a big part of my life and has accompanied me in completing this work.

Finally, I would also like to thank my family for their unconditional support and for accompanying me on my way through my studies.

"Remember that the truth is in the details. No matter how you see the world or what style it imposes on your work, the truth is in the details. Of course, the devil is also there." - Stephen King

LIST OF PUBLICATIONS AND MANUSCRIPTS

Publications and manuscripts related to this thesis:

Bolakhrif N, Gremer L, Pauly T, Chu C, Nagel-Steger L, and Willbold D, *High-level expression and purification of native-like human prion protein using Leishmania tarentolae*, in preparation 2023

Pauly T, Bolakhrif N, Kaiser J, Gremer L, Nagel-Steger L, Gohlke H, and Willbold D, *Met/Val129 polymorphism of the full-length human prion protein dictates distinct pathways of amyloid formation*, Journal of Biological Chemistry, Published 2022

Bocharov E, Gremer L, Urban A, Okhrimenko I, Volynsky P, Nadezhdin K, Bocharova O, Kornilov D, Zagryadskaya Y, Kamynina A, Kuzmichev P, Kutzsche J, Bolakhrif N, Mueller-Schiffmann A, Dencher N, Arseniev A, Efremov R, Gordeliy V, and Willbold D, *All-D-enantiomeric peptide D3 designed for Alzheimer's disease treatment dynamically interacts with membrane-bound amyloid-β precursors D3*, Journal of Medicinal Chemistry, Published 2021

CONTENTS

LIST OF FIGURES

List of Tables

LIST OF ABBREVIATIONS

Aβ	Amyloid-β
AD	Alzheimer's disease
ADAM	A disintegrin-and-metalloproteinase
AFM	Atomic force microscopy
AICD	APP intracellular domain
AL	Amyloid light chain amyloidosis
APP	Amyloid precursor protein
APPmc	$APP_{672\text{-}726}$ fragment
APPjmtm	$APP_{686\text{-}726}$
AUC	Analytical ultracentrifugation
BACE	β-site APP cleaving enzyme 1
BSE	Bovine spongiform encephalopathy
CD	Circular dichroism
CJD	Creutzfeldt-Jakob disease
CR	Congo red
cryo-EM	Cryogenic-electron microscopy
CSF	Cerebrospinal fluid
CTF	C-terminal fragment
CWD	Chronic wasting disease
Da	Dalton
DDM	N-Dodecyl-β-D-maltoside
DPC	Zwitterionic dodecylphosphocholine
E. coli	*Escherichia coli*
ELISA	Enzyme-linked immunosorbent assay
ER	Endoplasmatic reticulum
fCJD	Familial Creutzfeldt-Jakob disease
FFI	Fatal familial insomnia
FP	Fluorescence polarization
Gal	Galactose

GdnHCl	Guanidine hydrochloride
GlcN	Glucosamine
GlcNac	N-acetylglucoseamine
Glu	Glucose
GPI	Glycosylphosphatidylinositol
GSS	Gerstmann-Sträussler-Scheinker disease
huPrP	Human prion protein
IDP	Intrinsically disordered protein
IMAC	Immobilized metal affinity chromatography
JM	Juxtamembrane
L. tarentolae	*Leishmania tarentolae*
Man	Mannose
MD	Molecular dynamics
MDS	Microfluidic diffusional sizing
mGluR5	Metabotropic glutamate receptor 5
MMP	Matrix metalloproteases
MST	Microscale thermophoresis
NMDA	N-methyl-D-aspartate
NTC	Nourseothricin
PAGE	Poly-Acrylamide Gel Electrophoresis
PI-PLC	Phosphatidylinositol-specific phospholipase C
PK	Proteinase K
PMCA	Protein misfolding cyclic amplification
PNGase F	N-glycosidase F
PRE	Paramagnetic relaxation enhancement
PrP	Prion protein
PrP^{C}	Cellular prion protein
PrP^{Sc}	Scrapie prion protein
PTM	Posttranslational modification
ROS	Reactive oxygen species
sCJD	Sporadic Creutzfeldt-Jakob disease
SEC	Size Exclusion Chromatography
SDS	Sodium dodecyl sulphate
Sia	Sialic acid
ssNMR	Solid-state magnetic resonance spectroscopy
SV	Sedimentation velocity

TCA	Trichloroacetic acid
ThT	Thioflavin T
TM	Transmembrane
TSEs	Transmissible spongiform encephalopathies
UV	Ultraviolet radiation
vCJD	Variant Creutzfeldt-Jakob disease

SUMMARY

The human prion protein (huPrP) is a membrane-bound glycoprotein found mainly in the nervous system. HuPrP in its native conformation (huPrP^{C}) contains a globular C-terminal domain rich in α-helical structure and an unstructured N-terminal domain. Its physiological function has not been fully elucidated. HuPrP^{C} can undergo structural conversion to an infectious form (huPrP^{Sc}) rich in β-sheets typical for amyloid structure. This misfolded PrP^{Sc} is associated with prion diseases known as transmissible spongiform encephalopathies (TSEs). Susceptibility to TSE in humans is strongly influenced by a polymorphism of huPrP at position 129, which involves either valine (V) or methionine (M).

In this work, different pathways of amyloid formation are presented for the 129V and 129M full-length variants of huPrP. Amyloid formation of the 129V variant starts directly from a destabilized monomeric state. The 129M variant undergoes a more complex aggregation process with oligomeric intermediates. The higher propensity of the 129M variant to form oligomers is already present prior to amyloid formation. A shorter construct of the 129M variant containing only the structured C-terminal domain lacks most oligomers and consequently exhibits similar aggregation behavior to the full-length 129V variant. This highlights the importance of the flexible N-terminus, which tends to go unnoticed in prion research, and emphasizes a possible interaction with the globular domain depending on the 129M/V polymorphism. These results contribute to the understanding of the differences between the two variants of the polymorphism at position 129 and a possible interaction between C- and N-terminus that might be related to the differences observed in pathology.

To approach huPrP studies on a close to physiological level, an eukaryotic expression system was used to provide native-like full-length huPrP with all major post-translational modifications, including glycosylphosphatidylinositol-anchoring and mammalian-like glycosylation. *Leishmania tarentolae* (*L. tarentolae*) was used for stable and high-level expression of native-like huPrP. A purification protocol was established, involving the incorporation of native-like huPrP into micelles. The purified native-like huPrP possessed a conformation dominated by α-helical and random coil structure and was predominantly monomeric (∼90 %). Comparison of native-like huPrP (expressed in *L. tarentolae*) and huPrP (expressed in *Escherichia coli* (*E. coli*)) revealed differences in secondary structure and solubility at physiological conditions. HuPrP expressed

in *E. coli* is less soluble at pH 7.4, containing a majority of aggregates ($\sim$71 %), while the remaining protein was mainly monomeric ($\sim$22 %). The soluble fraction of huPrP expressed in *E. coli* indicates an increased amount of β-sheet structure. The purified native-like huPrP expressed in *L. tarentolae* is superior to huPrP expressed in *E. coli* for studies under physiological conditions and holds great potential for studies focusing on high-resolution structures or kinetics of misfolding.

1

INTRODUCTION

1.1. Prion

The term 'prion' was introduced by Stanley Prusiner in 1982 to describe 'a small proteinaceous infectious particle that is resistant to inactivation by most procedures that modify nucleic acids' [1]. At the time, this was a very controversial statement as it seemed to imply a form of replication that did not require nucleic acids, something that has never been observed at the time. The diseases Prusiner was trying to understand were a group of infectious neurodegenerative diseases that were first observed in sheep and goats as scrapie. Later, prion diseases had been diagnosed in more and more species, including humans. Important milestones in prion research are summarized in Figure 1.1 containing some of the most important properties of prions which are: (I) lack of nucleic acid [2], (II) self-replication by recruiting monomers from the non-infectious isoform [3], (III) partial resistance to proteases [4], and (IV) transmissibility [5].

(I) Chemical and physical methods commonly used to alter nucleic acids, including those of bacteria and viruses, could not be used to inactivate prions. The first experiments in this regard were performed as early as 1966 and 1967 by Alper et al. [6, 7]. At that time, the definition of the term 'prion' was still unknown, so that the term 'scrapie agent' is used in this section. With the use of ionizing radiation and UV irradiation, the scrapie agent remained active, leading the authors to conclude that the scrapie agent may be too small to be a viral genome. However, it was still questionable whether the pathogen could be a protein, because the pathogen was also resistant to UV irradiation at 280 nm, which specifically targets proteins [2].

(II) Later in 1967, Griffith et al. presented a model of a self-replicating protein associated with the scrapie agent [8]. Together with the findings provided by Prusiner 15 years later, the link between a protein and the scrapie agent was demonstrated and the above-mentioned term 'prion'

for 'proteinaceous infectious particle' was introduced [1]. Once the protein was identified, it was named prion protein (PrP), and found to be a membrane-bound glycoprotein, which is originally encoded by the host in a non-pathogenic form [9, 10, 11]. The pathogenic and non-pathogenic isoform differ mainly in their conformation. The pathogenic isoform contains mainly β-sheets, while the non-pathogenic isoform is composed of α-helical and random coil structure. During the same period (1982-1984), the first purification protocols were published by Prusiner, which provided insights into additional properties of prions [12, 13, 14]. Further experiments revealed theories of prion propagation, involving the non-pathogenic isoform, PrP^{C}, in the conversion and propagation of the pathogenic isoform, PrP^{Sc}. This underlies the 'protein-only' hypothesis, explaining the protein self-replication without nucleic acid [15, 3, 2]. PrP^{C} undergoes a structural rearrangement to form PrP^{Sc}, which in turn accelerates further conversion of PrP^{C} [16, 17, 18].

(III) Thereafter, in early 1985, Oesch et al. performed experiments in which they treated PrP from infected and uninfected brain tissue with proteinase K (PK) and found complete degradation of PrP from the healthy brain, whereas partial resistance of PrP was observed from the infected brain [19]. The N-terminal region of infectious PrP is truncated after PK treatment, resulting in a PK-resistant core of 27-30 kDa, instead of 30-35 kDa which refers to the typical size of PrP. Since then, proteinase K resistance has been known as one of the most important features of prions [4].

(IV) Transmissibility is probably the most important property of prions and was formerly used to distinguish prions from amyloids. However, this presumably unique feature was later observed in other amyloidogenic proteins like amyloid-β (Aβ) [3, 20], which is further described in a subsequent chapter. In 1939, the transmissibility of scrapie was demonstrated [21]. There are natural and experimental circumstances in which prions can be transmitted. These events differ in their efficiency, i.e., incubation time, amount of infectious agent, and success in overcoming species barriers, with a trend for natural transmission to be less efficient overall. Experimental transmission, on the other hand, when prions are administered intracerebrally in different animal models, show a shorter incubation time, a higher amount of infectious agent, and a higher efficiency in interspecies transmission [5, 22, 23]. Natural transmission has been observed from consumption of contaminated meat. In the 1985, peroral transmission caused the bovine spongiform encephalopathy (BSE) crisis that resulted in 180,000 clinically diagnosed prion cases in cattle. Since 1996, approximately 200 human cases of the new variant form of Creutzfeldt-Jakob disease (vCJD) have been identified that have been linked to the consumption of BSE-infected products [24, 25, 26]. For the sake of completeness, the BSE-infected products have been experimentally shown to be also perorally transmissible in mice [27], sheep [28], calves [5] and non-human primates [29]. The kuru epidemic was caused by ritual cannibalism in

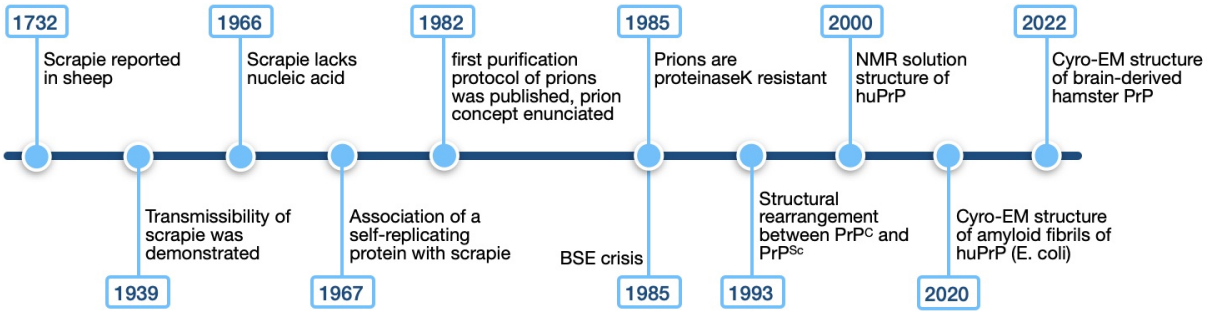

Figure 1.1: Timeline of prion research. The major milestones of the last 300 years related to prions are presented in a timeline beginning with the first observation of scrapie in sheep and extending to the recent high-resolution structural analysis of the infectious prion isolated from a hamster brain.

Papua New Guinea in the early 20th century [30]. The origin of kuru is believed to be due to one case of sporadic CJD [5]. Nearly 300 cases of iatrogenic tranmission of prions have been reported in which CJD was induced by medical interventions [5, 31]. Specifically, injections of human growth hormone from cadavers, transplantation of dura mater or cornea, and transmission through contaminated surgical instruments have attributed to the the transmission of prion and outbreak of iatrogenic CJD.

Considering all above-mentioned characteristics, the term 'prion' can be ascribed to the pathological isoform, PrP^{Sc}, but not the cellular isoform, PrP^{C}, although the chemical nature is identical [17, 2, 32]. PrP^{Sc} constitutes misfolded host-encoded PrP that replicate by templated protein polymerization.

1.1.1 Prion diseases

As mentioned in the previous chapter, prion diseases are based on a conformational rearrangement of the cellular isoform, PrP^{C}, into the pathological, insoluble scrapie isoform, PrP^{Sc}. Diseases caused by misfolding of the prion protein are collectively grouped as transmissible spongiform encephalopathies (TSEs). In human, several types are known based on the mode of infection and mutation of the *PRNP*-gene, encoding the prion protein [33, 34, 35]. In addition to the transmissible forms of CJD, namely variant CJD and iatrogenic CJD, there is also the sporadic form, which is most common. The cause of sporadic CJD (sCJD) is unknown, but it is assumed that this disease is either based on spontaneous conversion of PrP^{C} into PrP^{Sc}, a very rare event, or by somatic mutations [3, 36, 37, 38]. It should be noted that sCJD has been observed predominantly in homozygous carriers of the 129 polymorphism (both, valine or methionine homozygotes) [39]. The fourth form of CJD is familial CJD (fCJD) which is caused by autosomal

dominant inheritance. Other human prion diseases include kuru, Gerstmann-Sträussler-Scheinker (GSS) disease and fatal familial insomnia (FFI). Common to all prion diseases is widespread neurodegeneration leading to cognitive and motor dysfunction in patients [3, 39]. The genetic background of the inherited prion diseases is known, and all involve mutations in the PrP. GSS (P102L and 129V homozygosity) additionally involves slow progression of ataxia [40, 41], FFI (D178N and 129M homozygosity) also shows refractory insomnia and hallucinations [42], and fCJD (e.g. E200K and 129M homozygosity) is characterized by rapidly progressive dementia and sleep disturbance, among other features [43].

The already mentioned naturally occurring methionine (M)/valine (V) polymorphism at position 129 is a strong genetic susceptibility factor and modifies prion diseases, since, for example, patients with the mutation D178N develop either FFI or fCJD depending on the presence of M or V at position 129, respectively [44]. Apparently, only homozygous 129M patients were susceptible to vCJD [45, 46]. Heterozygous carriers appear to be protected from iCJD and generally show a slow progression compared with homozygous 129M and 129V carriers, resulting in a delay of disease onset by approximately one decade [47, 39]. This may also be the reason why the proportion of heterozygosity in the human population is highest at about 51 %[48]. About 12 % have a genotype of V/V, and the remaining 37 % are homozygous M/M individuals.

For completeness, it should be noted that not only humans but also many animals can develop different types of prion diseases. Scrapie in sheep and goats is the most common prion disease in animals and also the first animal prion disease described as early as 1732. There are further prominent prion diseases in animals, like BSE in cattle and the more recently spreading chronic wasting disease (CWD), which affects deer and elk [3, 49].

1.1.2 Prion Protein

The native human prion protein, huPrP^{C}, is a cell membrane-bound glycoprotein. It is encoded by the *PRNP* gene which is located in the short arm of human chromosome 20 and mainly expressed in neurons and glial cells of the brain and spinal cord [50, 51].

HuPrP^{C} initially consists of 253 amino acid residues. During maturation of the protein, the N-terminal and C-terminal signal sequences are cleaved off, resulting in the mature protein, consisting of 207 amino acid residues (huPrP(23-230)) (see Figure 1.2). The N-terminal signal sequence (amino acid residues 1 to 22) is responsible for the transport from ribosomes to endoplasmic reticulum (ER) [53]. The 23 amino acid residues long C-terminal signal sequence (amino acid residues 231 to 253) is replaced by a glycosylphosphatidylinositol (GPI)-anchor after

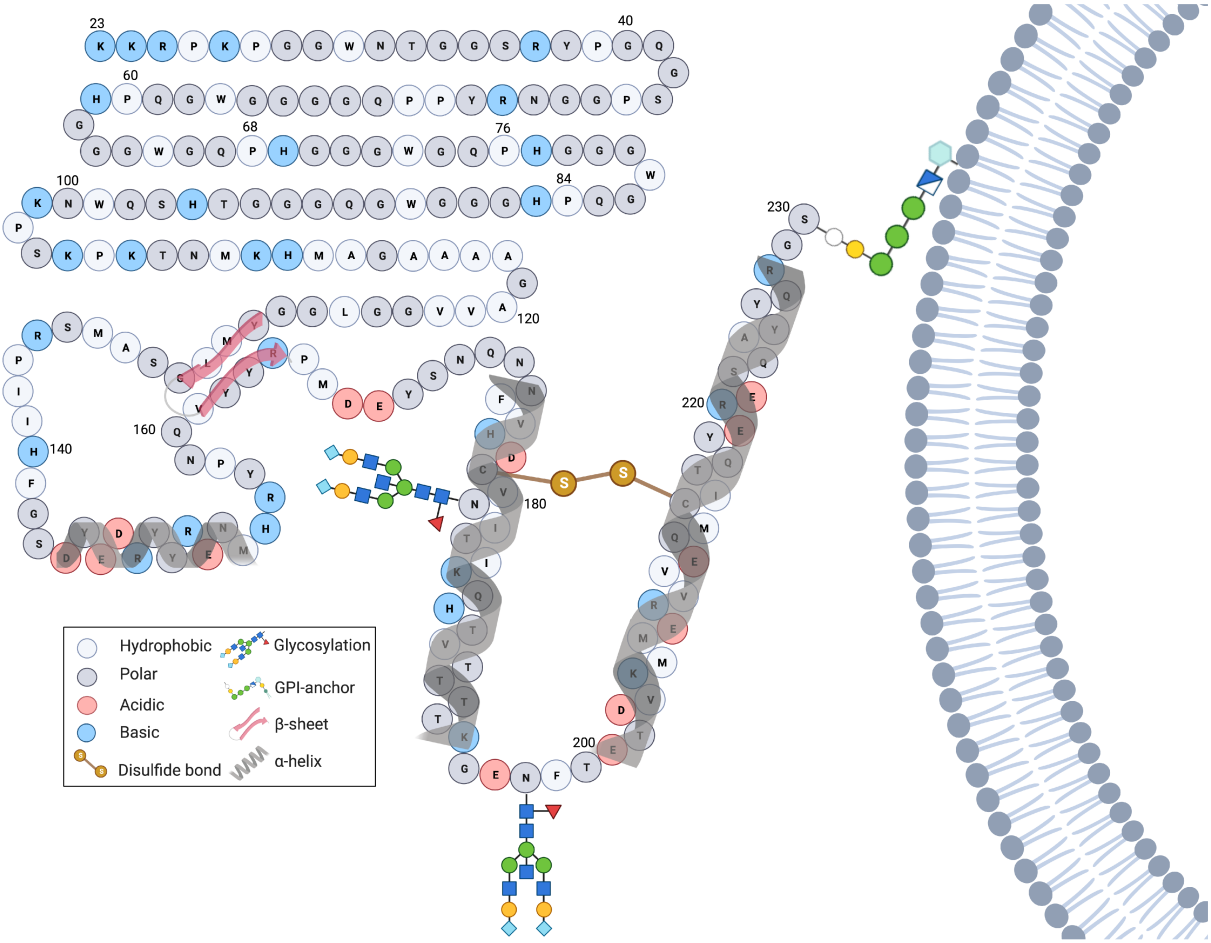

Figure 1.2: Schematic representation of the full-length human prion protein. Amino acid sequence, including secondary structure elements and post-translational modifications of full-length huPrP(23-230). The flexible N-terminal region spans from residue 23 to 127. The structured C-terminal region contains three α-helices (amino acid residues 144 to 154, 173 to 194, and 200 to 228) and a short anti-parallel β-sheet (amino acid residues 128 to 131 and 161 to 164). Membrane anchoring at the C-terminal end is provided by the GPI-anchor. Two glycans are present at N181 and N197. Image was created with BioRender.com, whereby structural elements were taken from Zahn et al., 2000 [52].

cleavage and connects the mature PrP to the outer cell membrane. Additional post-translational modifications (PTMs), in the form of N-glycosylations, are found on N181 and N197. The main sequence of huPrP(23-230) begins with a flexible, unstructured N-terminal region (amino acid residues 23 to 127) containing a series of five proline- and glycine-rich octapeptide repeats and a high number of basic amino acid residues [51, 52]. This is followed by a globular, structured C-terminal region extending from amino acid residues 128 to 228. Three α-helices (helix 1: amino acid residues 144 to 154, helix 2: amino acid residues 173 to 194, and helix 3: amino acid

residues 200 to 228) and a short antiparallel β-sheet (amino acid residues 128 to 131 and 161 to 164) are present in this region [52]. A disulphide bond between helix 2 and helix 3 (C179 and C214) stabilizes the globular domain. Interestingly, Zahn et al. showed in 2000 that both, the C-terminal domain and the N-terminal region, can interact to form a transient complex, so that the conformational state of helix 2 and 3 is highly dependent on the length of the N-terminal tail [52]. The N-terminal tail interestingly does not seem to be involved in the amyloid fibril structure after *in vitro* conversion of recombinant PrP^{C} to PrP^{Sc} [54]. Recent cryogenic electron microscopy data revealed homogeneous and unbranched amyloid fibrils including the misfolded C-terminal domain (see Figure 1.5 A) [54, 55].

Cleavage of the huPrP^{C}

In total, huPrP^{C} can undergo four post-translational cleavages. α-cleavage and β-cleavage take place in the N-terminal region and release N1, C1 and N2, C2 fragments of PrP, respectively. γ-cleavage and shedding take place in the C-terminal region and release N3, N4 and shedded PrP, respectively [56]. A disintegrin and metalloproteinase (ADAM) enzymes are involved in α-cleavage. Specifically, ADAM10 is responsible for constitutive N1 release, with ADAM17 contributing to N1 release upon stimulation [57, 58]. The cleavage site is located between H111 and M112 and releases the 11 kDa N-terminal N1 fragment. The 18 kDa C-terminal C1 fragment remains membrane bound. Interestingly, the flexible N-terminal part with polycationic patches (amino acid residues 23 to 27 as well as amino acid residues 95 to 110) of huPrP^{C} was shown to be essential for interaction with Aβ oligomers [59, 60].

In contrast, β-cleavage occurs just downstream of the octapeptide region (Q91 and G92), releasing a 9 kDa N2 fragment, lacking the second polycationic stretch (amino acid residues 95 to 110) involved in the interaction with Aβ oligomers, as well as a membrane-bound 20 kDa C2 fragment.

Because the γ-cleavage was only recently discovered, the exact cleavage site is not yet revealed. Nevertheless, the fragment size is known (N3 fragment at 20 kDa and the membrane-bound C3 fragment at 5 kDa), and therefore the cleavage is thought to occur in close proximity to the end of the C-terminal region (amino acid residues 170 to 200) [56, 61]. Members of the matrix metalloproteases (MMP) family are likely to be involved in this cleavage process [61]. Interestingly, γ-cleavage occurs mainly at unglycosylated prion protein, so it is reasonable to speculate that the cleavage site is sterically inaccessible due to its proximity to glycans at positions 181 and 197 [56]. Similarly, to α-cleavage, ADAM10 is also involved in the shedding of the PrP close to the GPI-anchor (between G228 and R229) [56].

Each cleavage process seems to have a biological function. The fragments released into the extracellular space, such as N1, N2, or shedded PrP, have been shown to have neuroprotective potential, for example, by scavenging toxic Aβ oligomers and preventing the interaction of these oligomers with the membrane-bound full-length huPrP^{C}. The complex formed by the interaction of Aβ oligomers with the membrane-anchored PrP leads to the activation of the neighboring membrane-bound metabotropic glutamate receptor 5 (mGluR5) [62]. This in turn leads to activation of Fyn kinase, which causes phosphorylation of the GluN2A and GluN2B subunits of N-methyl-D-aspartate (NMDA) receptors. This phosphorylation results in hyperactivation of NMDA receptors and causes increased calcium influx, which ultimately leads to cell death. On the other hand, the full-length huPrP^{C} also acts as a substrate for prion replication and therefore is an important mediator of toxicity in prion diseases. Thus, the presence of α-cleavage is neuroprotective, preventing both prion replication and oligomer-mediated toxicity and cell death [63, 56]. In addition, the membrane-bound C1 fragment was shown to inhibit prion replication in mice [64, 65]. Because β-cleavage is mediated by reactive oxygen species (ROS), it may be protective against oxidative stress in the cell [66]. To date, not much is known about γ-cleavage, but the resulting C3 fragment was observed in large amounts in CJD brains, suggesting an important role in prion disease pathology [61]. Finally, Linsenmeier et al. have recently shown that the release of shedded huPrP^{C} correlates negatively with conversion to huPrP^{Sc} [67].

Apart from the neuroprotective properties of huPrP^{C}, the general function of the full-length huPrP^{C} still remains elusive. However, several studies have shown that the flexible N-terminal part of PrP^{C} is involved in myelin homeostasis [68], circadian rhythm [69, 56], and metal ion homeostasis due to the affinity of the ocatpeptide region for copper ions [70, 71].

GPI-anchor

The GPI-anchor is covalently bound to the carboxyl end of S230 of huPrP, consisting of an ethanolamine phosphate (Figure 1.3 red frame), three mannose units with a glucosamine unit (Figure 1.3 blue frame), and phosphatidylinositol with two fatty acid chains (Figure 1.3 green frame) that attach the protein to the outer cell membrane [72]. Phosphatidylinositol-specific phospholipase C (PI-PLC) can be used to cleave GPI-anchored proteins from the cell membrane. PI-PLC cleavage occurs within the phosphatidylinositol region.

In mammalian cells, numerous plasma membrane proteins, especially those anchored by GPI, are associated with sphingolipid- and cholesterol-rich microdomains called lipid rafts [74]. Indeed, membrane bound huPrP^{C} is also predominantly found in these microdomains [75]. The GPI-anchor is added to the protein during translocation into the ER immediately after cleavage of the C-terminal signal sequence. Both, cleavage of the polypeptide and attachment of the preformed

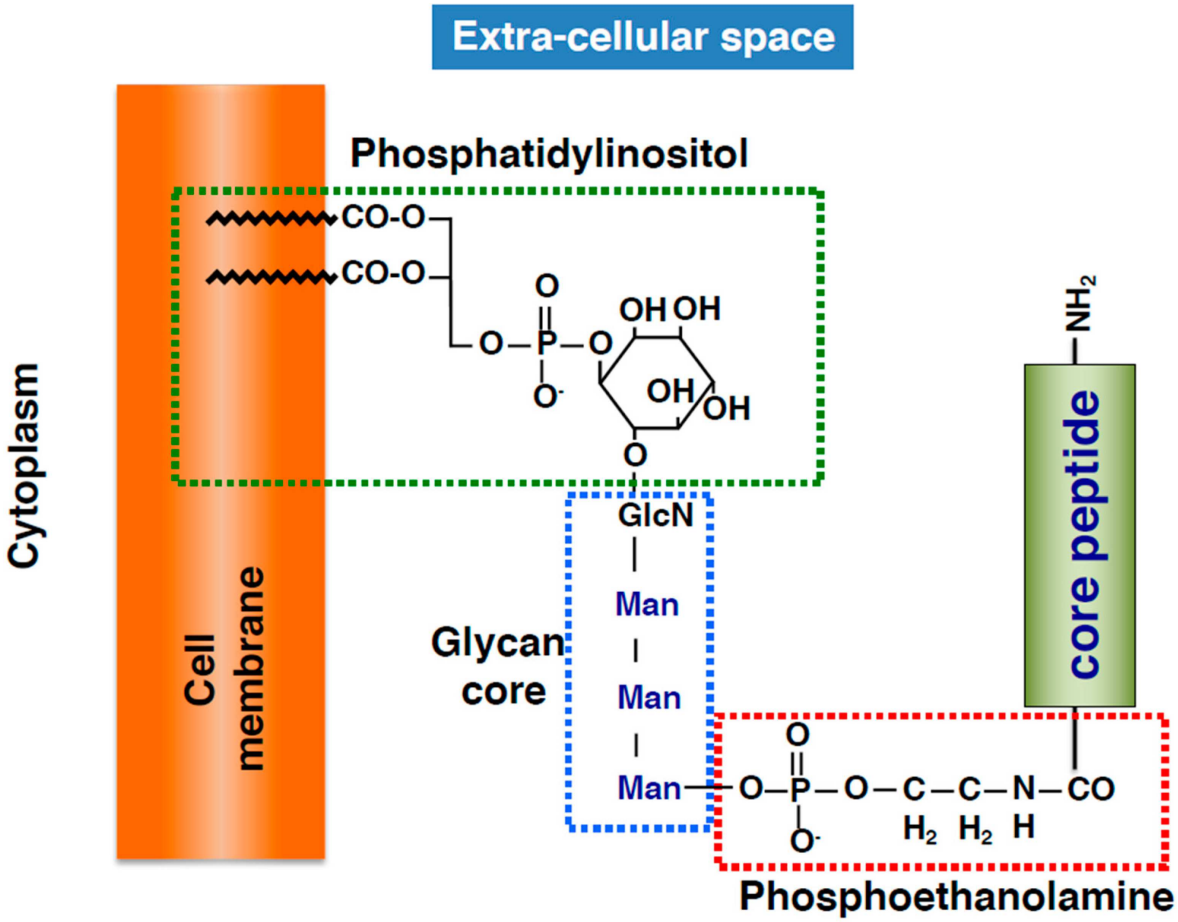

Figure 1.3: Schematic representation of the glycosylphosphatidylinositol (GPI)-anchor. The GPI-anchor consists of three units: phosphatidylinositol, glycan core and phosphoethanolamine. The C-terminal part of the protein binds to phosphoethanolamine (red frame). The glycan core consits of three mannose (Man) units and glucosamine (GlcN) (blue frame). The phosphatidylinositol is bound to the cell membrane by two fatty acids (green frame). Image taken from [73].

GPI-anchor occur at the ER membrane by a transamidase complex [75]. On the way to the cell surface, numerous modifications can be made to the core structure of the GPI-anchor, including the attachment of sialic acid to one of the mannose residues [76]. The GPI-anchor was also shown to be present in PrP^{Sc} and yet resistant to PI-PLC digestion, suggesting that the conformational change prevents the enzyme from reaching the cleavage site [77]. To date, there have been conflicting research findings regarding the importance of the GPI-anchor in prion propagation and prion disease, as Chesebro et al. 2005 showed that transgenic mice expressing anchorless mouse PrP^{C} indeed tend to misfold and deposit as amyloid plaques [78]. However, in the same

study, it was also shown that the clinical manifestation of scrapie was especially achieved by a combination of anchorless and GPI-anchored PrP^{C}. In general, there is a growing number of studies demonstrating the importance of GPI-anchoring in prion diseases. There is evidence that the location of PrP^{C} in lipid rafts is critical for the formation of PrP^{Sc} [79, 80, 81]. Other studies demonstrated that the substitution of the GPI-anchor and replacement with carboxy termini favoring transmembrane anchored PrP has an inhibitory effect on the formation of PrP^{Sc} [79, 82]. Considering the above-mentioned findings on the importance of the GPI-anchor and taking the neuroprotective properties of the fractions cleaved from the membrane-bound full-length PrP^{C} into account, it is reasonable to assume that the conversion of PrP^{C} to PrP^{Sc} and its propagation and toxicity are highly dependent on the presence of the GPI-anchor.

Glycosylation

Glycosylation, in addition to GPI-anchoring, is a PTM process that occurs in both the ER and the Golgi apparatus, where numerous glycosidases and glycosyltransferases covalently bind oligosaccharides to an amino acid within a protein [83, 84]. Several types of glycosylation are known, with N- and O-linked glycosylation being the most common in eukaryotes and they appear to have a major impact on the structure and function of proteins [85, 86, 87]. It should be noted that bacteria do not glycosylate proteins in this manner, so no glycoslation occurs at all upon recombinant expression in bacteria [88]. HuPrP contains two N-linked glycosylations, consisting of the binding of N-acetylglucosamine (GlcNAc) followed by further modifications at the nitrogen atom of asparagine (Asn) at positions 181 and 197. A prerequisite for N-glycosylation is a defined sequence of asparagine (Asn) - X - threonine (Thr)/ serine (Ser) - Y, where X and Y can be any amino acid except of proline (Pro) [85, 89].

Synthesis of the N-glycosylation precursor occurs by various transferases to dolichol pyrophosphate in the ER, resulting in 2 GlcNAc, 9 mannose (Man), and 3 glucose (Glu) molecules. After synthesis, the precursor is transferred *en bloc* from the dolichol pyrophosphate to the asparagine (Asn) of the target protein by oligosaccharyltransferase. After transfer, some Glu and Man residues are removed by glucosidases, exposing the core structure, which is later further modified in the Golgi apparatus. The core structure begins with the binding of GlcNAc to aspargine which is the most widespread carbohydrate-peptide bond in eukaryotic cells. This represents also the attachment point for a wide variety of complex oligosaccharides that depend on the protein, the cell in which it is expressed, and species ranging from high mannose glycans in yeast, to complex glycans in unicellular trypanosomes (e.g. *Leishmania tarentolae*) and mammals [85]. Despite this diversity, all N-glycans are synthesized *via* a common pathway with a typical core glycan structure. The core glycan structure essentially consists of 2 GlcNAc and 3 Man

residues, forming the uniform pentasaccharide core ($Man_3GlcNAc_2$). This core glycan is then further elaborated and modified in the Golgi apparatus, resulting in a variety of N-glycan structures, enabling two major classes of N-linked glycans [90]. The 'high mannose' glycan class, commonly found in yeast, is characterized by unsubstituted terminal multi-antennary mannose sugars after the $Man_3GlcNAc_2$ core (Figure 1.4). The 'complex' glycan class, commonly found in mammals, contains additional GlcNAc residues, galactose (Gal) molecules, and terminal sialic acid (Sia) residues after the $Man_3GlcNAc_2$ core. In addition, fucosylation (Fuc) can occur at the core GlcNAc residue in complex glycans (see Figure 1.4) [88]. As mentioned earlier, the initial N-glycosylation begins in the ER, involving processes within both the cytoplasmic and luminal domains of the ER. Thereafter, the protein, including the core glycan, undergoes further modifications that take place in the *cis* Golgi apparatus, followed by the *medial* Golgi, and finally the *trans* Golgi portion. Once the modifications in the Golgi complex are complete, the glycoprotein is transported to either the lysosomes, the secretory granules, or the plasma membrane [75]. The latter is the case for PrP.

The N-glycosylation of PrP is variable and leads to un-, mono-, or diglycosylated species, depending on how many oligosaccharide chains are occupied at the glycosylation sites. PrP^C and PrP^{Sc} digested with N-glycosidase F (PNGase F) exhibited reduced mass, indicating asparagine-linked glycans [92]. Glycosylation is present in both isoforms and has been shown to play a key role in regulating the replication rate, infectivity, and cross-species barrier of PrP [93, 94, 95]. Protein misfolding cyclic amplification (PMCA), which harness the ability of self-replication, is a technique for detecting the conversion of PrP^C to PrP^{Sc} *in vitro*. Camacho et al. demonstrated in 2019 a significant increase in PMCA amplification of various CJD strains when deglycosylated $huPrP^C$ was used as a substrate [95]. A few years earlier, in 2014, Katorcha et al. showed similar results in mice [94]. Here, they focused on the relevance of the sialylation level of N-glycans of PrP^C and showed that a decrease leads to an increased rate of prion replication and a reduction in species barrier when prion replication was seeded by heterologous seeds. However, a decrease in sialylation level also correlated with infectivity of PrP^{Sc} material produced *in vitro* [94]. Similar to the GPI-anchor studies in terms of relevance in prion diseases, the glycosylation studies also show controversial results. Lehmann and Harris showed in 1997 that Chinese hamster ovary cells expressing unglycosylated mouse PrP^C tend to develop properties similar to PrP^{Sc} [96]. On the other hand, mouse neuroblastoma cells did not show such PrP^{Sc} properties invoked by unglycosylated PrP^C [97]. Although PrP^C glycosylation is not required for the propagation of PrP^{Sc} or infection, there is evidence that the glycosylation can decelerate this conversion [98, 99]. Interestingly, there is a dependence of glycosylation on the GPI-anchor in PrP, since

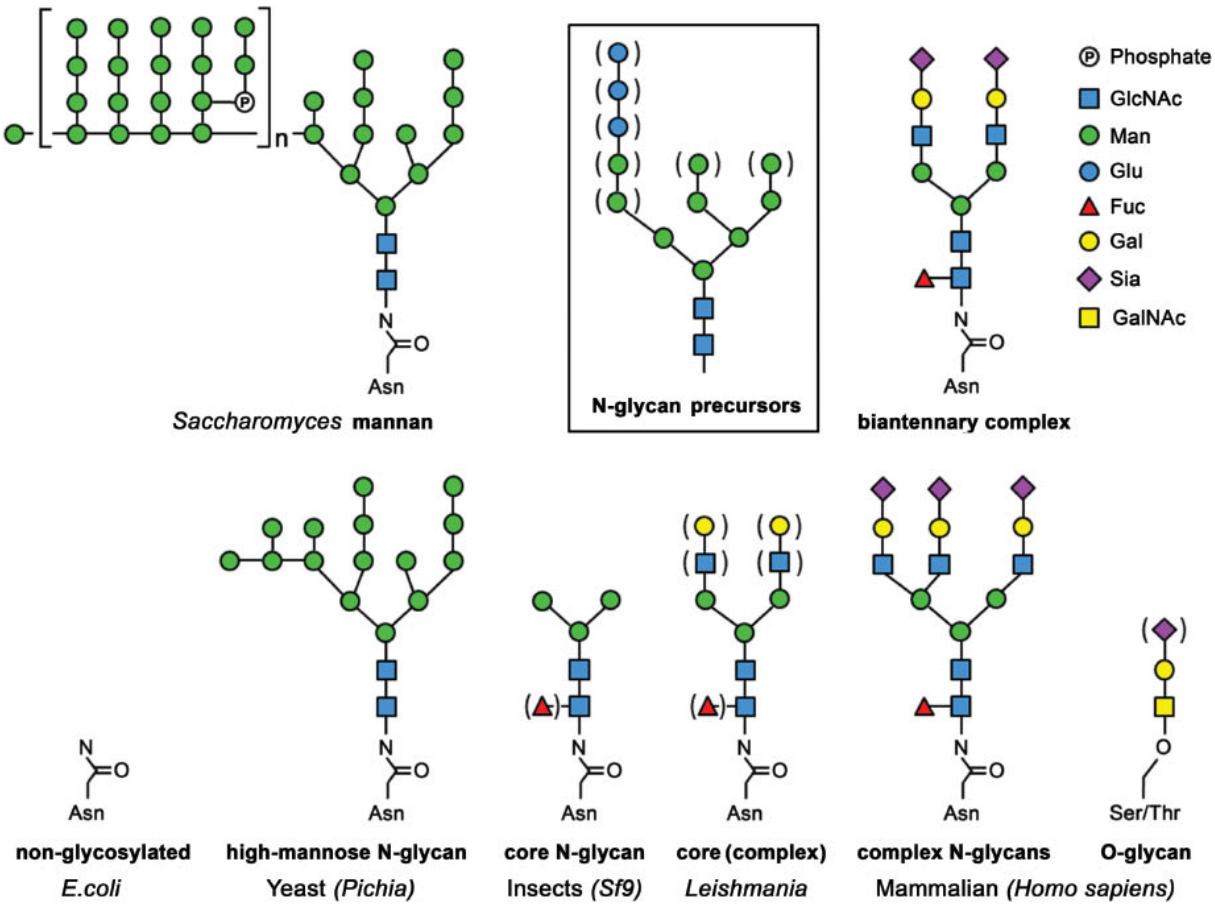

Figure 1.4: Schematic representation of N-glycan patterns of different species. The N-glycan precursor ($Glu_3Man_9GlcNAc_2$) shown in the top row yields the $Man_3GlcNAc_2$ core after further processing. This core is bound to asparagine (Asn) in all N-glycan patterns and is further modified to form mannose-rich (e.g. *Pichia pastoris*) or complex N-glycans (e.g. *L. tarentolae* or mammals). Mammals are also capable of forming O-glycans bound to threonine (Thr) or serine (Ser). *Escherichia coli* (*E. coli*) is not capable of any of these glycosylations. Image taken from [91].

expression of PrP lacking the C-terminal signal sequence responsible for GPI-anchoring also leads to expression of PrP lacking the glycosylation in a neuroblastoma cell line [99, 100].

Collectively, these studies underline the importance of GPI-anchoring as well as glycosylation of PrP^C and show that PrP including these PTMs must indeed be considered as a whole to act as a determinant of disease relevant conversion into the pathological isoform PrP^{Sc} and susceptibility to infection.

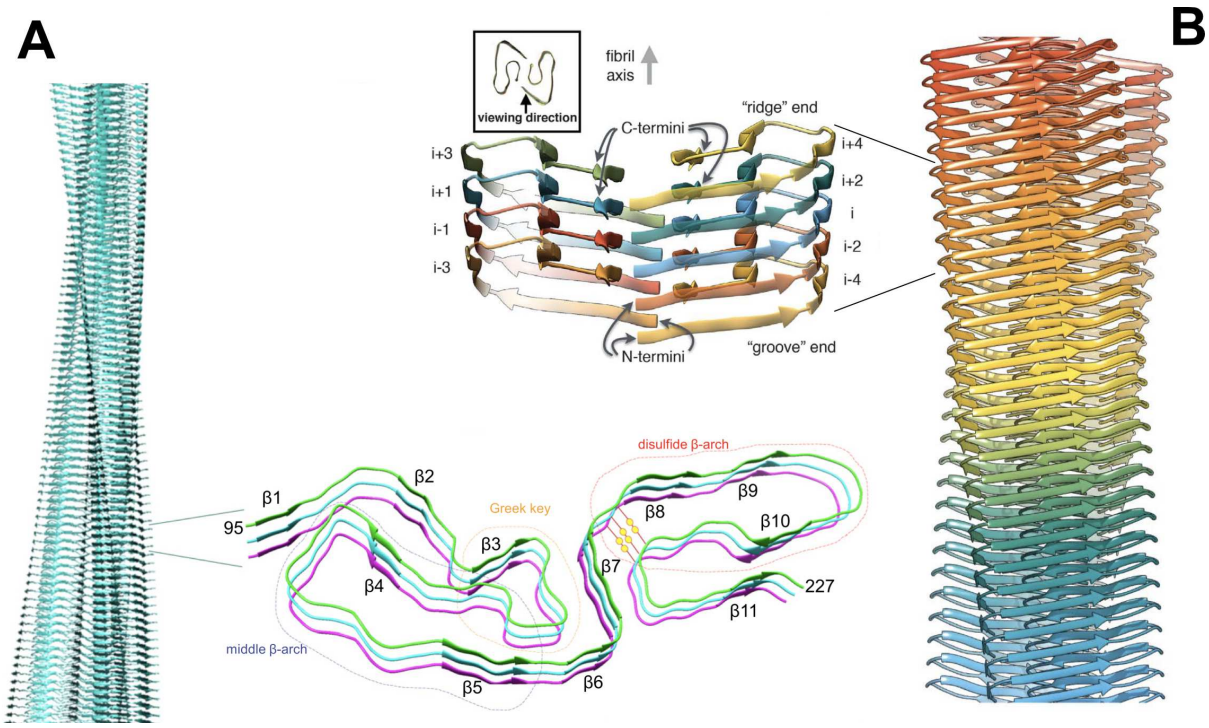

Figure 1.5: Typical cross-β-sheet fibril structure of the prion protein and Aβ. High-resolution cryogenic electron microscopy revealed a typical β-sheet structure of the monomers stacked perpendicularly on top of each other and stabilized by hydrogen bonds. A: Brain-derived mammalian prion protein fibril structure shows in the magnification a parallel in-register β-sheet conformation, containing one protofilament in the mature fibril. B: Aβ42 fibril structure shows an in-register β-sheet conformation in the magnification, consisting of two symmetric protofilaments in the mature fibril.
A: Recreated from Kraus et al., 2021 [55]. B: Recreated from Gremer et al., 2017 [107]

1.2. Amyloid

Amyloidogenic proteins are capable of conformational changes that result in the formation of highly structured fibrils possessing primarily a cross-β-sheet conformation [101]. These fibrils consist of monomeric subunits of the same protein stacked closely on top of each other and oriented perpendicular to the fibril axis (Figure 1.5). The typical β-sheet structure is usually not the native protein structure, but amyloid formation involves the structural conversion of intrinsically disordered, or even folded proteins. [102, 103, 32, 104]. Mature amyloid fibrils show a tendency to exist of protofilaments twisting around each other [105, 106].

Virchow introduced the term 'amyloid' in 1854 to describe abnormal deposits in the liver [108]. When the term was introduced, very little was known about its composition and its significance in various diseases. Originally, these deposits resulted in positive staining with iodine, a dye

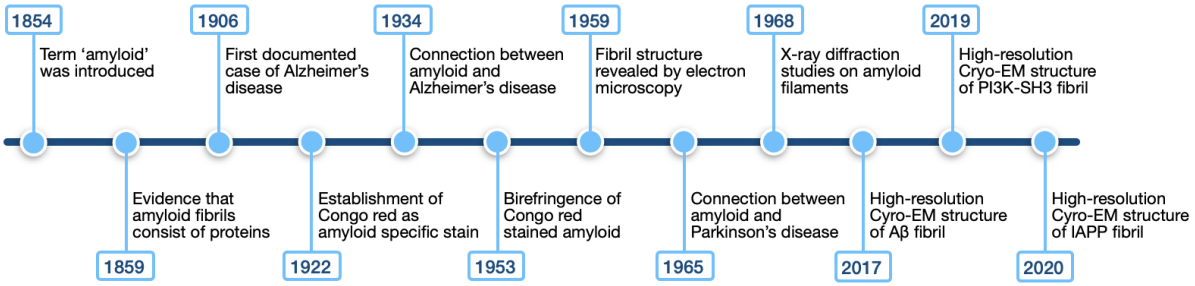

Figure 1.6: Timeline of amyloid research. The most important milestones related to amyloid from the last 145 years are presented in a timeline starting with the first observation of amyloid in the liver and extending to the latest high-resolution structures of amyloid fibrils.

that can be used to stain cellulose and starch. Five years later, in 1859, Friedreich and Kekulé dispelled this misunderstanding and demonstrated that amyloid fibrils were instead composed of proteins [109]. Almost 50 years after the term 'amyloid' was introduced, Alois Alzheimer reported the first case of Alzheimer's disease (AD) in his patient Auguste Deter in 1906 (Figure 1.6) [110, 111]. However, the link between AD and amyloid deposits in the brains of AD patients was not demonstrated until much later in 1934 [112]. During this time, other staining methods were established that allowed specific and long-lasting staining of amyloid, for example, the dye Congo red in 1934 [113]. Birefringence of Congo red-stained amyloids under polarized light in 1953 [114] laid the foundation for further research using electron microscopy, which revealed the fibrous structure in these samples in 1959 [115]. Since then, other properties have been characterized for amyloids, including the characteristic cross-β X-ray pattern with 4.7 Å distance between β-sheets [116]. Typical dimensions are 2 nm to 5 nm in width and multiples of that in length, which can end in the range of a few hundred nanometers [106]. In addition to Congo red staining, thioflavin T (ThT) has also been introduced as a very suitable dye for amyloid detection, leading to an increase in fluorescence and a shift in the wavelength of the emission peak after binding to the fibril structure [117, 118, 119].

1.2.1 Amyloid formation

Amyloid formation begins in a solution with monomers in their native conformation. The crucial event is the formation of a nucleus capable of recruiting further monomers by transferring structural information. This nucleus exhibits β-sheet structure typical for amyloid fibrils and can be characterized as the smallest assembly for which the addition of monomers is faster than the dissociation [120]. The lag phase is characterized by the absence of substantial amyloid growth. As soon as a nucleus capable of growth is formed, the aggregation mechanism enters the rapid

growth phase [120]. The lag phase constitutes the rate-determining step. The rapid growth phase is dominated by elongation of existing fibrils by addition of monomeric units to the fibril ends, fragmentation of the amyloid creating open ends for elongation, and secondary nucleation [32]. Secondary nucleation is nucleation on the fibril surface. Finally amyloid formation reaches a stable plateau, which is characterized by saturated amyloid fibril concentration in equilibrium with low monomer concentration [121]. This process of fibril formation can be followed by ThT fluoresence, which represents a sigmoidal curve that depicts the increase in amyloid over time. The time scale is highly variable and depends on several factors, such as monomer concentration and additional co-factors. Typically, the time scale of amyloid formation *in vivo* can be months to years [32]. *In vitro* studies usually have time scales ranging from a few hours, e.g. Aβ, to several weeks, e.g. PrP. To skip the lag phase, it is possible to add 'seeds' to a monomer solution. These seeds are short fibrils capable of exponential growth through elongation and other secondary pathways, as these pathways are highly dependent on the presence of amyloid fibrils [122]. In general, fibril formation is a thermodynamically favorable process, although a high energetic barrier still has to be overcome in the nucleation process to reach this thermodynamically stable amyloid state [123, 32, 124, 125].

In vitro models take advantage of much higher monomer concentration compared to physiological conditions to lower the energetic barrier. Under these supersaturated conditions, the growth-competent nucleus can form in a shorter time [126]. Increasing the monomer concentration also accelerates oligomer formation. Oligomers are small, soluble protein assemblies with heterogeneous structure, that consist of a wide range of monomeric units, and have a lower growth rate than amyloid fibrils [32, 120]. Depending on their contribution to fibril formation, they are either referred to as 'on-pathway' oligomers if they are becoming nuclei, or 'off-pathway' oligomers if they do not contribute to fibril formation. Whether oligomers are the primary source of toxicity in amyloid diseases such as Alzheimer's disease and not the highly structured fibrils is still controversial [127, 128, 129]. Nevertheless, their overall contribution to toxicity is widely recognized [130, 131, 132, 133]. However, the distinction between 'on-pathway' and 'off-pathway' oligomers does not necessarily correlate with toxicity. Most oligomers are 'off-pathway', and the remaining 'on-pathway' oligomers take a long time to solidify into small fibrils [32]. Some proteins that are not intrinsically disordered proteins, such as PrP, require a destabilized native conformation, which can be achieved by denaturation, pH change, and shaking for fibril formation [134]. Reducing structural constraints favors intermolecular interactions, e.g., hydrogen bonding, electrostatic interactions, and hydrophobic interactions, which can further promote fibril formation [135]. *In vivo*, the destabilized native conformation is often caused by mutations and therefore increases the susceptibility to misfolding diseases.

Structural details revealed by solid-state magnetic resonance spectroscopy (ssNMR) [136, 137], and (cryogenic) electron microscopy ((cryo-)EM) [107, 138, 139, 55] are one of the most important findings that paved the way for understanding the disease-causing structural transformation of many proteins. Some of the amyloid fibril structures that have been resolved by cryo-EM include the Aβ42 peptide [107], the Src-homology 3 domain of phosphatidyl-inositol-3-kinase (PI3K-SH3) [140], and the islet amyloid polypeptide (IAPP) [139]. To date, 50 different proteins or peptides are known to assemble into amyloid fibrils and are associated with severe human diseases. The formation of extracellular plaques, consisting of amyloid fibrils or intracellular amyloid-like deposits lead to a wide spectrum of human diseases. These diseases can be classified as either neurodegenerative diseases, non-neuropathic diseases, or non-neuropathic systemic amyloidosis, with a classification based on the location of the amyloid deposits [141]. In neurodegenerative diseases such as Alzheimer's disease, Parkinson's disease, or TSE, deposits of aggregated Aβ, α-synuclein, and PrP, respectively, are found in the brain. Non-neuropathic diseases such as type II diabetes are characterized by deposits in tissues other than the brain, whereas non-neuropathic systemic amyloidoses such as amyloid light chain amyloidosis (AL) occur in multiple tissues. In addition to the pathological aspects, amyloids are also known to be functional in prokaryotes and mammalian systems [141, 142]. This will not be further highlighted in this thesis, instead a focus will be placed on the misfolding of proteins that lead to neurodegenerative diseases, in particular PrP and Aβ.

Neurodegenerative amyloid diseases are based on the misfolding of a native protein into highly structured amyloid fibrils. Amyloid fibril formation *in vivo* usually occurs with increasing age and can be summarized as a slow and rare process [32]. The reason for this may also lie in the increasing concentration of the relevant monomeric proteins in the brain with increasing age [143]. For Aβ , concentrations between 10^{-11} and 10^{-9} M were found in the CSF [32], for PrP approximately 10^{-9} M (when assuming 125 mL as total volume of CSF, and a molecular weight of PrP of 22878 g/mol) [144]. The first event in fibril formation, namely the formation of an autocatalytic growth-competent nucleus, may be influenced in addition to age by co-factors such as RNA [145], traumatic brain injuries [146] or mutations [32]. Afterwards, fibril formation occurs, resulting in a broad range of different fibril morphs. However, only a few of these fibrils will proliferate and deposit. The prerequisites for proliferation are high thermodynamic stability, resistance to proteolytic enzymes and stabilization by co-factors [32].

1.2.2 Alzheimer‘s disease

Alzheimer's disease (AD) is characterized by extracellular deposits of the misfolded Aβ peptide. Besides the accumulation of Aβ, a proliferation of hyperphosphorylated tau proteins, called

neurofibrillary tangles, is found inside of neurons in the brains of AD patients [147]. In addition to these typical hallmarks, oxidative stress and neuroinflammation accompany AD [148]. All these biological processes eventually lead to the continuous degradation of neuronal tissue. This is reflected by various symptoms. First and foremost, dementia is often associated with Alzheimer's disease [149]. Almost 2/3 of reported dementia cases can be attributed to Alzheimer's disease. Due to the aging population, the prevalence of dementia is expected to double in Europe and triple worldwide (from 50 million to 150 million cases) by 2050 [150, 149]. The risk of developing Alzheimer's disease is 60-80 % dependent on heritable factors, and more than 40 genetic risk loci have already been identified associated with AD, of which the APOE alleles have the strongest association with the disease [149]. Another key risk factor for AD is age, such that the incidence of AD is about 14 times higher in people aged 85 years or older compared in people aged 65 to 69 years [151]. Other symptoms besides dementia in AD patients include loss of general cognitive function as well as language comprehension [152, 153].

A very promising treatment for Alzheimer's disease are all-D-enantiomeric peptides. They have two major advantages. Firstly, they are more resistant to proteolytic enzymes and secondly, they have a lower immunogenic potential compared to L-enantiomeric peptides [154, 155, 156]. Using mirror-image phage display, D-peptides from a peptide library containing more than one billion different 12 amino acid residues long peptides were screened against the monomeric Aβ42 [157]. D3 (sequence: rprtrlhthrnr) is one of these all-D-enantiomeric peptides consisting of 12 D-enatiomeric amino acid residues with high affinity for binding Aβ due to electrostatic interactions of positively charged arginine residues with negatively charged aspartate and glutamate residues of Aβ [158]. D3 showed a reduction of cytotoxic Aβ oligomers *in vitro* as well as a reduction of amyloid plaque load and cerebral inflammation *in vivo* [158, 159, 160, 161].

1.2.3 Amyloid-β peptide

Amyloid plaques in Alzheimer's disease patients consist of extracellular accumulations of misfolded Aβ . Several forms of variable lengths of this peptide are present *in vivo*. The 42 amino acid residue variant (Aβ42) is most prone to form amyloid, while the 40 amino acid residue variant (Aβ40) is most abundant in humans [162, 163, 164]. These Aβ peptides originate from cleavage of the amyloid precursor protein (APP). The 100-140 kDa APP is a transmembrane protein that is especially expressed in the central nervous system. APP is especially known to function as a regulator of synaptic formation and repair [165], as well as iron export [166]. However, it is best known for being involved in the formation of Aβ peptides. It consists of a large globular and glycosylated N-terminal region and a short C-terminal region, which is integrated into the cell membrane [167]. These sections can be cleaved by several secretases. In

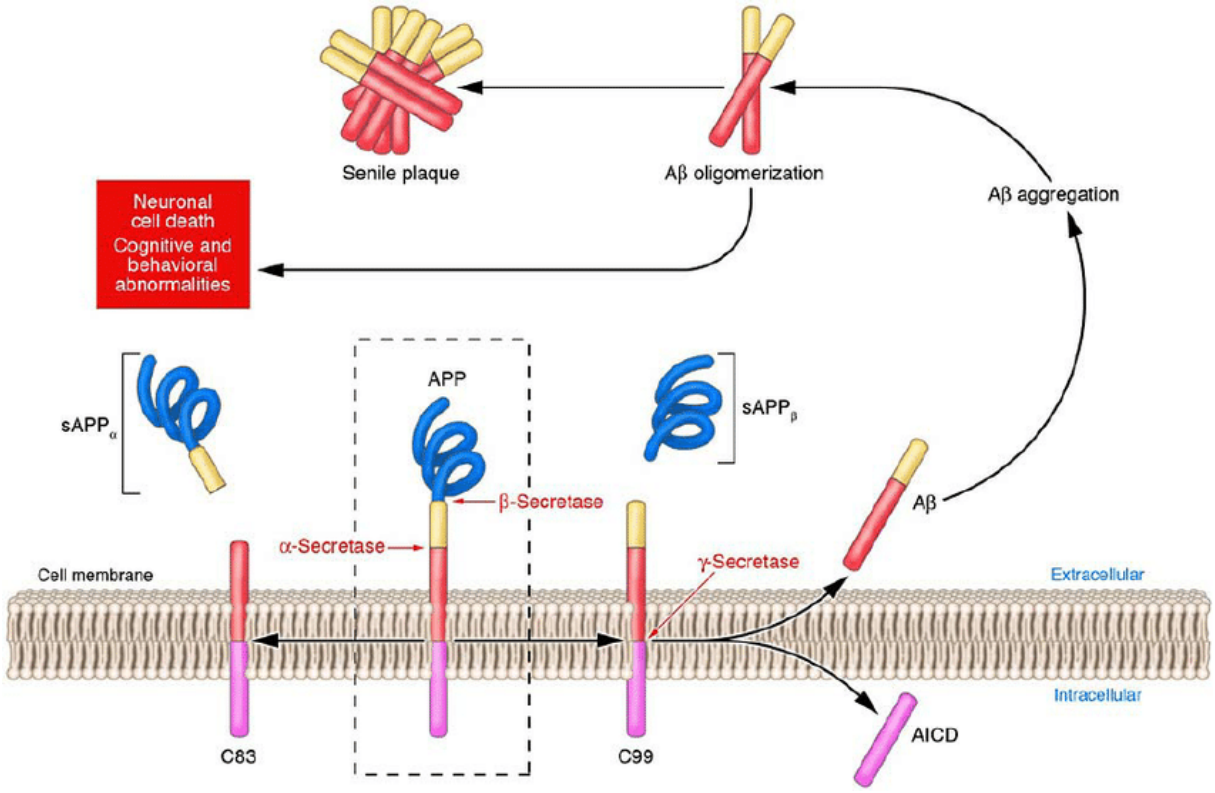

Figure 1.7: Cellular processing of the amyloid precursor protein (APP) and the production of Amyloid-β . APP is a transmembrane protein that can be cleaved by α-, β-, and γ-secretase. After cleavage by β-secretase, the remaining membrane-bound fraction can be further processed by γ-secretase to yield two soluble variants of the Amyloid-β peptide, the Aβ40 or the Aβ42 peptide. The formation of Amyloid-β is summarized as the amyloidogenic pathway because aggregation of Amyloid-β is related to the formation of amyloid plaques and eventually leads to neuronal death. The non-amyloidogenic pathway involves γ-cleavage succeeding α-cleavage. Image taken from Spies, 2012 [168].

the amyloidogenic pathway, two secretases, β-secretase and γ-secretase, are sequentially involved [168]. In the non-amyloidogenic pathway, however, α-secretase precedes before γ-secretase (Figure 1.7).

After the first cleavage by α-secretase, a C-terminal 83 amino acid long fragment remains membrane bound and the N-terminal $sAPP_{\alpha}$ is released into the extracellular space followed by the γ-secretase, which further cleaves the C83 fragment (Figure 1.7) [167]. These secretases encompass the non-amyloidogenic APP pathway. The β-secretase mediates the amyloidogenic pathway. It cleaves the APP closer to the N-terminal end of APP and exposes the $sAPP_{\beta}$ fragment. The remaining 99 amino acid long C-terminal transmembrane fraction is further processed by γ-secretase to yield the soluble Aβ40 peptide or Aβ42 peptide, depending on the cleavage site

[169]. Once amyloid plaques of Aβ have formed, they can mainly be found in the neocortex of AD patients [162].

The Aβ peptide is an intrinsically disordered protein (IDP) whose physiological function is still unknown. However, it is thought to be involved in synaptic plasticity [170, 171]. Its pathological function is crucial, which is why efforts have been made to resolve the high-resolution structures of the misfolded and AD-associated amyloid state. Gremer et al. showed in 2017 that amyloid fibrils of Aβ42 formed *in vitro* comprise typical amyloid fibril structure with parallel, in register cross-β-sheet conformation of monomeric units [107, 32]. Such fibrils showed a very conspicuous LS shape, consisting of two protofilaments (see Figure 1.5 B)[107].

1.3. Prion-like properties of amyloidogenic proteins

The debate about the summarization and delimitation of *prion* and *amyloid* still occupies many contemporary scientists and is still not fully resolved. Here, I will try to summarize some common features of amyloid and prion, assuming that some of the prion-like properties mentioned below may well be attributed to amyloid.

Starting with the fundamental protein-only hypothesis, which includes the concept of autocatalytic self-propagation of a misfolded state, which can be attributed to both, prions and amyloid. The transmission of structural information to other monomers without nucleic acid is therefore the most prevalent similarity [32, 172]. It is noteworthy that in both cases the native form of the monomer is non-infectious, whereas the end product which eventually is amyloid structure in both cases, is often associated with pathogenicity.

More recently, some amyloidogenic proteins have also been attributed with transmissibility, like Aβ [3, 20], which served as the main differentiator in the initial separation of amyloid and prion. Another example is the intercellular transmissibility of α-synuclein, which was recently demonstrated [173].

In addition to transmissibility, prions are also known to occur sporadically, similar to amyloidosis. These amyloid-associated diseases are characterized by rare occurrence of spontaneous onset and rapid spread with little possibility of treatment or recovery. Similar to prion, these diseases may also be hereditary or even transmissible, as previously mentioned for α-synuclein in Parkinson's disease or Aβ in AD.

1.4. *Leishmania tarentolae* as eukaryotic expression system

Leishmania tarentolae (*L. tarentolae*) is a parasite of the gecko *Tarentola annularis*. *Leishmania* belongs to the order of trypanosomatids together with *Trypanosoma*. Trypanosomatids in turn are a subgroup of the class Kinetoplastida, which are the earliest branches of eukaryotes together with mitochondria [174].

The non-pathogenic eukaryotic protozoan *L. tarentolae* has a life cycle that varies between sand flies and geckos. Sandflies contain the promastigote phenotype characterized by a monoflagellate, teardrop-shaped structure with a length of 4-12 µm and a width of 0.5-3 µm [88]. This phenotype is usually found in suspension cell cultures. *L. tarentolae* was introduced in 2002 as a platform for recombinant protein expression [175]. Ten years later, the genome of *L. tarentolae* was sequenced, revealing the loss of genes associated with human pathogenic species, as many other Leishmania species are known to cause various forms of leishmaniasis in humans [176, 88]. Since then, *L. tarentolae* has found a wide range of applications and has been used to produce therapeutic antibodies [88] and the soluble and glycosylated α-cleavage product of APP, namely $sAPP_{\alpha}$, among others (Figure 1.7) [177].

The use of *L. tarentolae* as a system for recombinant protein expression offers two major advantages:

Firstly, it is able to generate mammalian-type PTMs, such as phosphorylation, GPI-anchoring, and N- as well as O-glycosylations [88, 178, 179]. Because of the parasitic lifestyle of *L. tarentolae*, the oligosaccharide structures of their glycoproteins often resemble those of mammals and in some cases may contain the human-like complex biantenary N-glycans, only lacking the terminal sialic acids (Figure 1.4) [175, 178]. This leads to high similarity to the native-like state of human glycoproteins, like huPrP [180]. However, it is possible to fully humanize glycans in *L. tarentolae* by integrating a trans-salidase gene that allows the transfer of sialic acid to endogenous glycoproteins [181, 182, 183]. Considering that N-glycosylation contributes greatly to protein folding, which in turn prolongs half-life and regulates interaction with cell receptors, it is crucial to consider these PTMs when studying the structural properties of native-like human proteins [88, 184].

Secondly, LEXSY (*Leishmania* expression system), developed by the Max Planck Institute of Molecular Physiology and the German company Jena Bioscience, allows easy handling and wide application, which has been used since 2002 [175, 185]. These modes include secretory or intracellular expression of proteins by constitutive or inducible expression systems, which can also be genomically integrated or episomally introduced [88]. For the cultivation of the cells,

a temperature of only 26°C and the avoidance of light are required. This also allows for a fast growth rate, with a doubling time of 6 h when agitated and high cell densities due to suspension culture (up to 10^9 cells/ml). This, in turn leads to high protein yields (in the range of mg protein per liter of culture) [175, 186].

1.5. Aims

Considering, that a single amino acid exchange of huPrP is associated with various disease susceptibilities and pathologies in humans, it is of general interest to understand the molecular mechanisms underlying the diseases associated with the 129M/V polymorphism. This work aims to answer the question, if the polymorphism at position 129 of huPrP dictates distinct pathways of amyloid formation, which eventually translates into different disease development.

The great obstacle to overcome includes the solubility of full-length huPrP (expressed in *E. coli*) under physiological pH. More importantly, relevant post-translational modifications, such as glycosylation and membrane anchoring, are commonly neglected due to the bacterial expression system. The second part of this work aims to bring advance to prion research by introducing a suitable eukaryotic expression system and purification protocol to provide native-like full-length huPrP (129M) including all major PTMs. Finally, the cellular conformation of both, full-length huPrP expressed in *E. coli* and full-length native-like huPrP expressed in *L. tarentolae*, will be biophysically characterized at physiological pH.

2

MET/VAL129 POLYMORPHISM OF THE FULL-LENGTH HUMAN PRION PROTEIN DICTATES DISTINCT PATHWAYS OF AMYLOID FORMATION

2.1. Article information

Title of manuscript: Met/Val129 polymorphism of the full-length human prion protein dictates distinct pathways of amyloid formation

Authors: Thomas Pauly[1,2,‡], Najoua Bolakhrif[1,2,‡], Jesko Kaiser[3], Luitgard Nagel-Steger[1,2], Lothar Gremer[1,2], Holger Gohlke[3,4,5,6], and Dieter Willbold[1,2,*]

Journal: Journal of Biological Chemistry

Status: Published (August 2022)

[1] Institut für Physikalische Biologie, Heinrich-Heine-Universität Düsseldorf, 40225 Düsseldorf, Germany

[2] Institute of Biological Information Processing (IBI-7: Structural Biochemistry), Research Center Jülich, 52425 Jülich, Germany

[3] Institute for Pharmaceutical and Medicinal Chemistry, Heinrich-Heine-Universität Düsseldorf, 40225 Düsseldorf, Germany

[4] Jülich Supercomputing Centre (JSC), Forschungszentrum Jülich GmbH, 52425 Jülich, Germany

[5] Institute of Bio- and Geosciences (IBG-4: Bioinformatics), Forschungszentrum Jülich GmbH, 52425 Jülich, Germany

[6] John von Neumann Institute for Computing (NIC), Forschungszentrum Jülich GmbH, 52425

Jülich, Germany
* d.willbold@fz-juelich.de
‡ Authors contributed equally

2.2. Declaration of article contributions

2.2.1 Experimental

AUC experiments, kinetics, CD measurements, and absorbance measurements were performed by me and Thomas Pauly.

2.2.2 Data analysis

Data analysis of AUC experiments, kinetics, CD measurements, and absorbance measurements was performed by me and Thomas Pauly.

2.2.3 Manuscript preparation

All figures were prepared by me and Thomas Pauly. I wrote the complete manuscript in collaboration with Thomas Pauly, Jesko Kaiser, Holger Gohlke, Luitgard Nagel-Steger, Lothar Gremer, and Dieter Willbold.

2.3. Abstract

Methionine/valine polymorphism at position 129 of the human prion protein, huPrP, is tightly associated with the pathogenic phenotype, disease progress, and age of onset of neurodegenerative diseases such as Creutzfeldt-Jakob disease or Fatal Familial Insomnia. This raises the question of whether and how the amino acid type at position 129 influences the structural properties of huPrP, affecting its folding, stability, and amyloid formation behavior. Detailed biophysical characterization of the 129M and 129V variant of recombinant full-length huPrP(23-230) by amyloid formation kinetics, circular dichroism spectroscopy, molecular dynamics simulations, and sedimentation velocity analysis reveal differences in their aggregation propensity and oligomer content, leading to deviating pathways for the conversion into amyloid at acidic pH. The 129M variant exhibits less secondary structure content before amyloid formation and higher resistance to thermal denaturation compared to the 129V variant, whereas the amyloid conformation of both variants shows similar thermal stability. Molecular dynamics simulations and rigidity analyses at the atomistic level identify intramolecular interactions responsible for the enhanced monomer

stability of the 129M variant, involving more frequent minimum distances between E196 and R156, forming a salt bridge. Removal of the N- terminal half of the 129M full-length variant diminishes its differences compared to the 129V full-length variant and highlights the relevance of the flexible N-terminus in huPrP.

2.4. Introduction

Transmissible spongiform encephalopathies are also known as prion diseases since they are based on the misfolding of the prion protein [9]. HuPrP is a membrane-bound glycoprotein, located mainly in nervous tissues, such as the brain and spinal cord. Two isoforms are known: the cellular form ($huPrP^{C}$) is non-pathogenic, rich in α-helices (42 %) and contains a single, small β-sheet (3 %) [187]. The other isoform, associated with the disease ($huPrP^{Sc}$), contains 34 % to 43 % β-sheets and 20 % to 30 % α-helices [187, 188]. Prions are defined as proteinaceous infectious particles [189], which in contrast to viruses lack any genetic information provided by nucleic acids. The structural conversion from $huPrP^{C}$ into $huPrP^{Sc}$ and aggregation into toxic oligomers and fibrils is governed by autocatalytic processes [32]. Recently published high-resolution structures of PrP amyloid fibrils by cyro-EM revealed a typical β-sheet structure [55, 54]. Several neurodegenerative diseases such as CJD, FFI, Gerstmann-Sträussler-Scheinker syndrome and Kuru are human prion diseases and associated with these amyloid structures. The well-known methionine/valine polymorphism at position 129 appears in the cellular conformation at the beginning of the first β-strand (Figure 1A). About 51 % of the human population are heterozygous at position 129, 12 % have a genotype of valine/valine, and the remaining 37 % a genotype of methionine/methionine [48]. This methionine/valine polymorphism is associated with the age of onset, the disease progress and which pathogenic phenotype is developed in patients [190, 191, 192, 193]. The polymorphism at position 129 raises the question of how it determines the pathogenic roles, especially with respect to the aggregation behavior during the conversion of $huPrP^{C}$ into $huPrP^{Sc}$. In several studies properties of the amyloid fibril structure [194] and unfolded state [195, 196] of different prion protein variants had been investigated, revealing not only different amyloid fibril morphologies [197] within these variants and other mutations [198], but also further requirements for fibril formation such as a disulfide bond [196]. This work presents a detailed biophysical characterization of full-length huPrP(23-230) for both variants and a comparison with a shorter construct, lacking the unstructured N-terminal region, huPrP(121- 230) for the 129M variant. Understanding the impact of a single amino acid residue exchange on the propensity of huPrP to convert into the pathogenic amyloid structure in vitro will help to gain insights into the pathomechanisms of prion diseases. Since the recombinantly produced full-length huPrP(23-230) does not aggregate spontaneously at physiological pH within

manageable time ranges, we established an in vitro conversion system at acidic pH with additional destabilization by guanidine hydrochloride (GdnHCl). Amyloid formation kinetics monitored by the fluorescence dye ThT was used to examine aggregation pathways. CD spectroscopy was used to determine the secondary structure content before and during the amyloid formation process as well as the thermal stability before and after amyloid formation. Additionally, molecular dynamics (MD) simulations and rigidity analyses were performed to investigate the stability of both variants in detail. SV analysis was performed to investigate the monomeric and oligomeric states before amyloid formation.

2.5. Results

Differences in amyloid formation kinetics of both variants monitored by ThT fluorescence are presented in Figure 2.1B. At pH 2.0 we used 0.5 M GdnHCl for an additional weak destabilization of 15 µM huPrP(23-230) to accelerate conversion into an amyloid structure (different conditions for huPrP and GdnHCl concentrations were tested, see Figure 2.5, 2.6, 2.7). Strikingly, both variants behave distinctly in the ThT kinetic assay. However, both variants have in common that neither amyloid formation nor an initial fluorescence plateau occurred in the controls without GdnHCl (Figure 2.5), indicating no conversion of huPrP(23-230) without destabilization within the observation time. The 129M variant shows a more complex amyloid formation behavior, resembling kinetics with multiple phases. The kinetics to reach the final plateau are retarded compared to the 129V variant and passing through two interim plateaus. The 129M variant shows clear initial ThT fluorescence identical to the triplicates. The first steep increase starts reproducibly at about 25 h. Differences are observed in the duration of the single growth phases, their number and heights of interim and final plateaus. The time point of the second increase is approximately 55 h. Overall, the reproducibility within the triplicates is low. In contrast, the 129V variant shows an immediate steep ThT fluorescence increase without any lag phase. The amyloid formation of the 129V variant exhibits a single-phase aggregation behavior. The reproducibility among the triplicates is high. Nevertheless, despite the obvious differences, both variants result in rather similar ThT fluorescence after 120 h. Measuring the concentration of the soluble fraction after 120 h revealed 72.5 % and 84.1 % of aggregated protein for the 129M and 129V variants, respectively (Figure 2.8).

CD spectra were measured to determine the secondary structure content of huPrP (Figure 2.1C). Here, 10 µM huPrP(23-230) without GdnHCl before amyloid formation at pH 2 was analyzed for both variants (Figure 2.1C, left). Since CD is a bulk method, the signal represents the weighted average in secondary structure content for the sample. Oligomeric species with

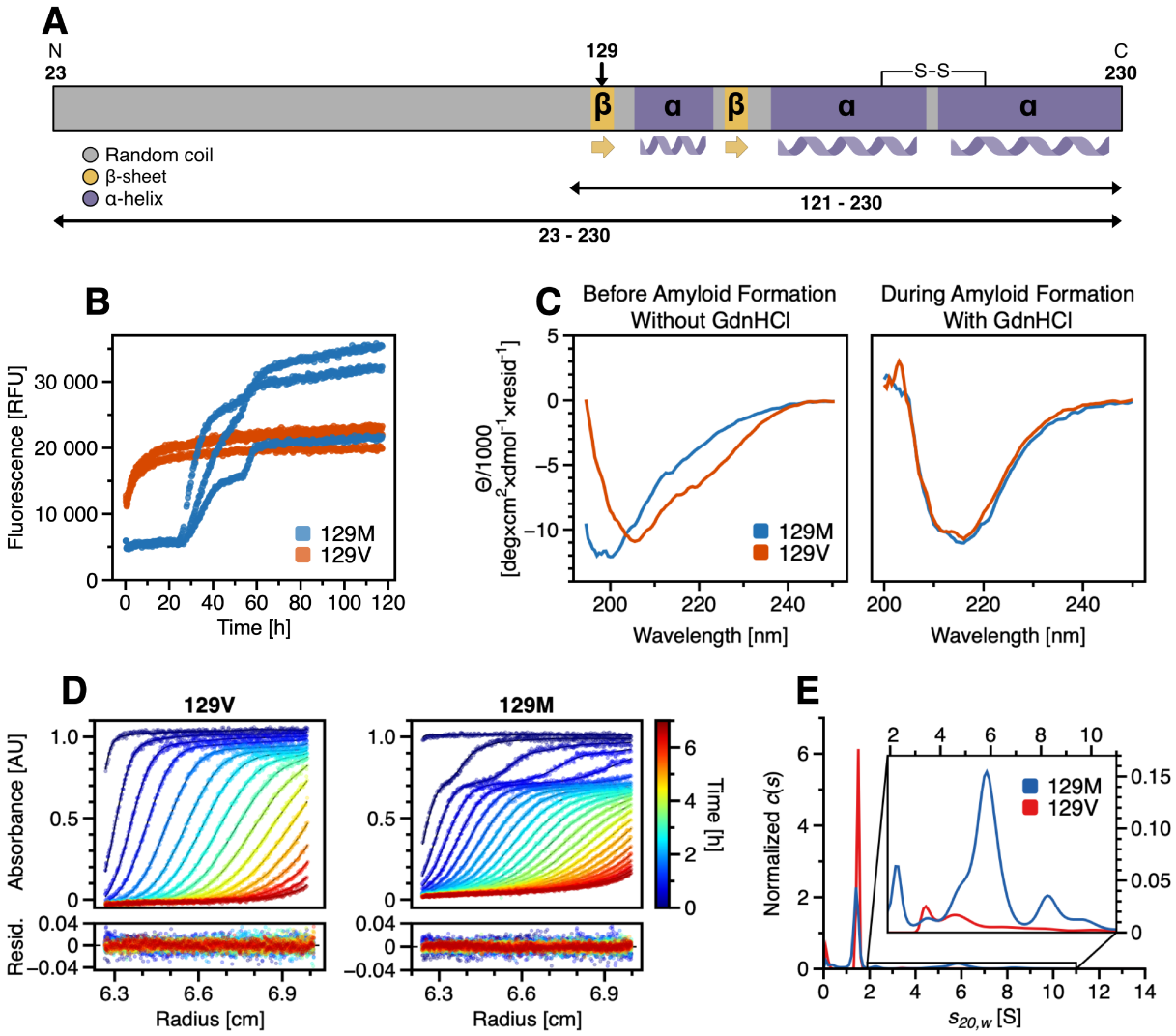

Figure 2.1: Aggregation behavior of full-length huPrP(23-230). (A) Scheme of full-length huPrP(23-230) secondary structure elements. huPrP(23-230) comprises the unstructured N-terminal half and structured C-terminal domain, containing a disulfide bond between C179 and C214; huPrP(121-230) lacks the unstructured N-terminal region. (B) Amyloid formation kinetics are monitored by ThT fluorescence for triplicates of the 129M variant (blue) and 129V variant (red). 15 M huPrP(23- 230) was incubated with 0.5 M GdnHCl for destabilization and initialization of amyloid formation. (C) Secondary structure are represented in CD spectra of 10 µM huPrP(23-230) without (left) and with 0.5 M GdnHCl after 5 h incubation (right) for both variants. The incubation conditions are identical to amyloid formation kinetics. (D) SV analysis of 7.5 µM of both variants without GdnHCl. Raw data from SV analysis with fitted Lamm-equation solutions from $c(s)$ model are color-coded for the duration of sedimentation. (E) The result of data fitting is an s-value distribution.

different monomer conformations might contribute to the measured spectra. For both variants we observed CD spectra with a shape resembling a mixture of mainly α-helical and random

coil structure. The position of the first minimum differs; it is at about 200 nm for the 129M variant and about 207 nm for the 129V variant. Additionally, a more positive signal between about 207 nm and 240 nm is observed for the 129M variant, suggesting a somewhat higher content of random coil structure. The secondary structure content was also investigated at time points during the amyloid formation process in the presence of 0.5 M GdnHCl (Figure 2.1C, right, Figure 2.10). Five hours after the addition of GdnHCl, a horizontal shift of the minimum from 200 nm to approximately 218 nm is observed for both variants, indicating an increase in β-strand conformation. This shift barely changes for longer incubation time but a drop of the peak signal at 218 nm was observed together with a loss of the accompanying uv absorbance signal (Figure 2.10), so that one can assume a loss of soluble protein due to aggregation [199]. These results support the conversion into amyloid for both variants. Although the amyloid formation behavior of the 129M variant seems retarded and follows a more complex and time-consuming mechanism, the difference in amyloid formation behavior between both variants is not reflected in the secondary structure of converted forms.

SV analysis was performed to characterize the hydrodynamic properties of both variants at pH 2 and examine the molecular assemblies present before amyloid formation (Figure 2.1D and E). These conditions can be referred to as starting conditions before GdnHCl is added for destabilization and initialization of amyloid formation. Figure 2.1D shows raw data as sedimentation profiles with fitted Lamm-equation solutions. The resulting distribution of standardized sedimentation coefficients ($s^{20,w}$) presents differences in the degree of oligomerization between both variants (Figure 2.1E). Molar mass is calculated based on the globally determined frictional ratio (f/f_0), which is proportional to the hydrodynamic radius. At pH 2 f/f_0 was about 2.2 for both variants, indicating an elongated shape. The 129M variant shows a faster sedimenting oligomer boundary, representing 31.6 % of the total signal and corresponding to s-values between 2 S and 15 S (potentially dimers to 15-mers). The remaining 68.3 % of the sample can be assigned to the monomer state at 1.41 S. In contrast, most of the 129V variant is monomeric (93.1 %) at 1.49 S and only 6.8 % are oligomers between ∼2 S and ∼15 S. A closer examination of the oligomer distribution yields significant differences for the smallest detectable species. A distinct peak can be assigned at 2.3 S for the 129M variant with a molar mass corresponding to a dimer. The smallest oligomer of the 129V variant can be assigned to a peak at 3.5 S with a molar mass appropriate for a trimer. The peak at 3.5 S can also be found in the distribution of the 129M variant. The 129M variant is more susceptible to oligomerization than the 129V variant and forms dimers at pH 2 without GdnHCl. The addition of GdnHCl had no impact on the monomer sedimentation coefficient corrected for increased density and viscosity of both variants. This indicates a similar shape of the monomer both in the presence and absence of GdnHCl and, thus,

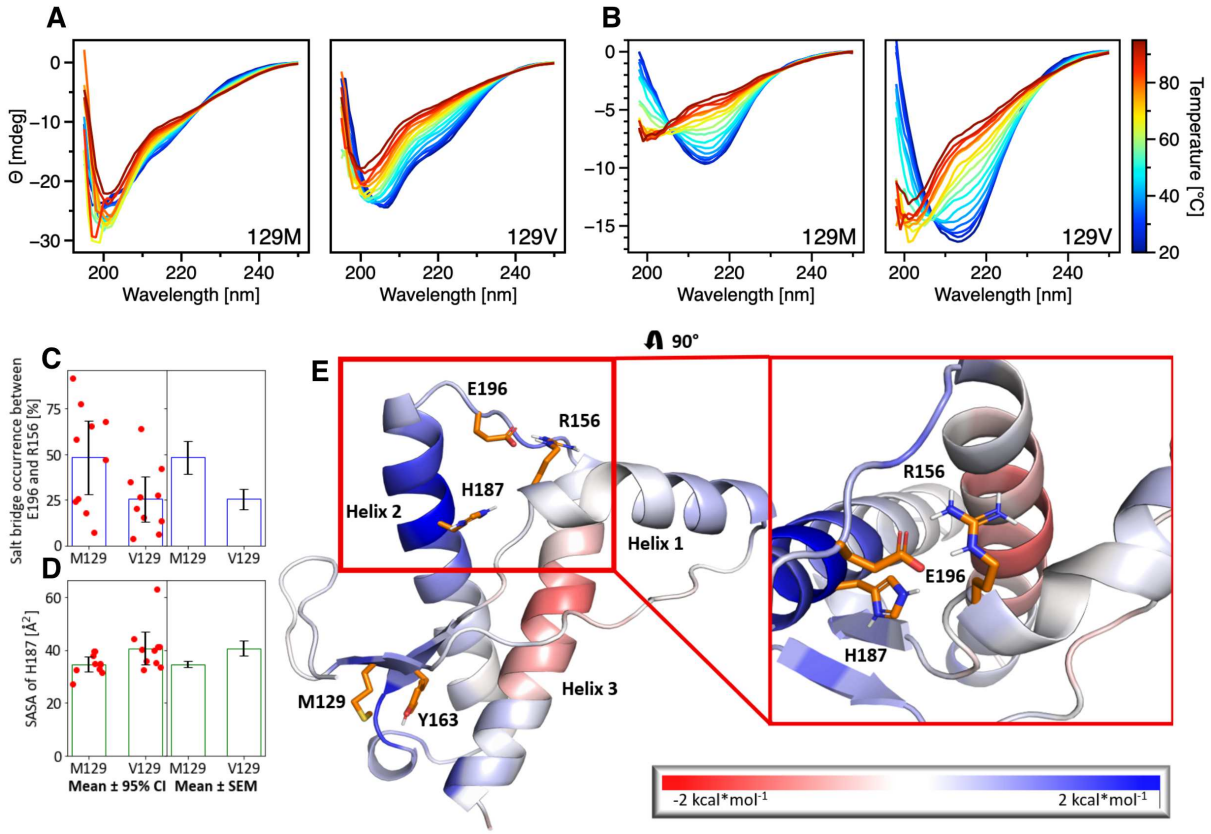

Figure 2.2: Stability of huPrP. (A) Thermal denaturation over a temperature range from 20°C to 95°C before amyloid formation at pH 2 and (B) after amyloid formation at the end of kinetic experiments (after 120 h) of both variants of full-length huPrP(23-230). CD spectra of 10 µM of the 129M (A, left) and 129V (A, right) variant. CD spectra of end products from amyloid formation kinetics of 20 µM of the 129M (B, left) and 129V (B, right) variant. (C) Occurrence of salt bridge formation between E196 and R156 and (D) SASA values of H187 during MD simulations for both polymorphs. In (C) and (D), the mean 95 % CI and all data points (left), and the mean ± standard error of the mean (right) are shown; the two mean values differ significantly, respectively (see text). (E) Differences of the residue–wise structural stability as determined from rcij,neighbor maps from CNA mapped onto the non-amyloid conformation of huPrP(118- 224). Blue indicates that the respective area is more stable in the 129M variant.

only minor changes in the fold induced by GdnHCl facilitate amyloid formation. A similar effect was published before with urea as a denaturant [199].

To probe differences in thermal stability, CD spectra of 10 µM huPrP(23-230) for each variant were recorded over a temperature range from 20°C to 95°C (Figure 2.2A). The same stability test was performed for the amyloid conformation obtained after 120 h incubation (Figure 2.2B). Samples with amyloid conformation were taken from kinetic experiments. Before amyloid formation, the 129M variant shows at 20°C a spectrum that indicates higher random coil content

than the 129V variant, and the spectrum only weakly changes with increasing temperature (Figure 2.2A, left). The CD spectrum before amyloid formation of the 129V variant at 20°C exhibits more initial secondary structure and changes clearly during temperature increase (Figure 2.2A, right). For both variants a rise of the CD signal at about 210 nm is observed during temperature increase, indicating an increase in random coil structure [200]. The CD spectra at 20°C of the amyloid conformation show a high content of β-sheet structure which is similar for both variants (Figure 2.2B). The amyloid structure of both variants exhibits clearly a structural change upon temperature increase. The final spectrum at 95°C resembles the secondary structure content of samples before amyloid formation, indicating reversibility of the amyloid structure for both variants at pH 2. Note that the signal of the amyloid conformation is higher for the 129V variant which hints at a larger amount of amyloid structures at the end of kinetic experiments, in agreement with the concentration left in the soluble fraction (see Figure 2.8). The lower impact of thermal denaturation on the 129M variant before amyloid formation compared to the 129V variant may explain the retarded conversion into amyloid structure observed in kinetic experiments. Despite the differences between both variants in amyloid formation kinetics, the final products present similar structure and thermal stabilities.

To investigate underlying reasons at the atomistic level for the different thermostability of the variants before amyloid formation, we performed ten replicas of 1 µs long all-atom molecular dynamics (MD) simulations for the protein fold at pH 2 of PrP(118-224) of both variants. Subsequently, we performed rigidity analyses using Constraint Network Analysis (CNA) [201] to compute the chemical potential energy averaged over the conformational ensemble, which correlates with the thermostability of proteins [201, 202]. Accordingly, the folded domain of the 129M variant is more stable (ECNA = –1003.3 kcal/mol) than the 129V variant (ECNA = -966.1 kcal/mol). To elucidate the molecular interactions that lead to this enhanced stability, we computed the differences in the neighbor stability maps (rcij,neighbor) generated by CNA [201]. rcij,neighbor indicates if a rigid contact between two residues is weaker or stronger. A contact is considered to be rigid when both residues belong to the same rigid cluster along the constraint dilution trajectory [201, 203] and, therefore, indicates the structural stability of the involved residue pair. M129 stabilizes the region located close to the substitution site. The longer side chain of methionine allows more apolar interactions with neighboring amino acids. Furthermore, methionine can form interactions with the aromatic side chain of Y163 (Figure 2.2E), further stabilizing the 129M variant [204]. M129 also has an allosteric stabilizing impact reaching over 20 Å to the C-terminal part of helix2 (Figure 2.2E). This region, especially H187, has been described to play a role in stabilizing the protein [205, 206]. Because of a pKa value of about 5, H187 is protonated at acidic but not at physiological pH [207]. The protonated form of H187

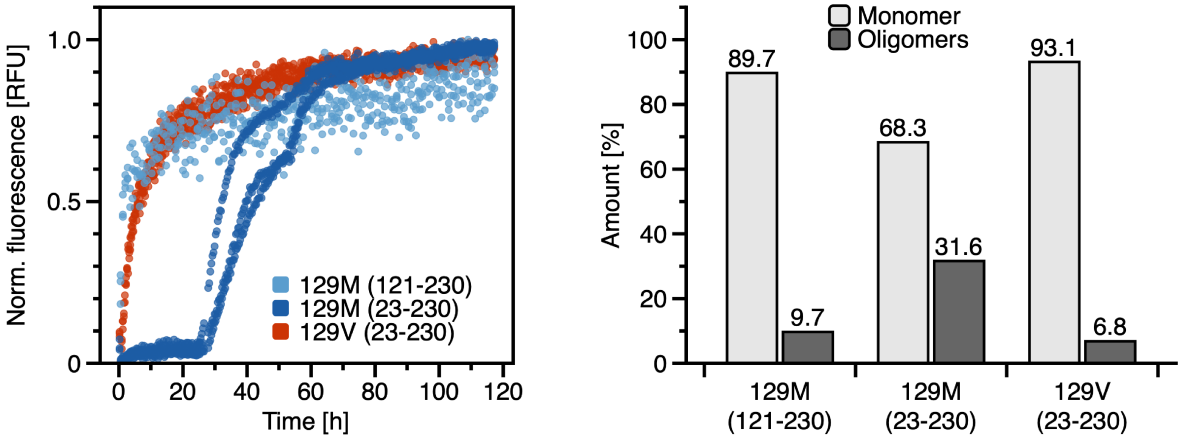

Figure 2.3: Relevance of the unstructured N-terminal region. (A) Amyloid formation kinetics monitored by ThT fluorescence of the 129M variant huPrP(121-230) lacking the unstructured N-terminal region (light blue). Kinetics for full-length huPrP(23- 230) 129M variant (dark blue) and 129V variant (red) from Figure 2.1B is shown again for comparison. Kinetic data is normalized to 1 for the highest signal. 15 µM huPrP was incubated with 0.5 M GdnHCl for destabilization and initialization of amyloid formation. (B) Amount of monomer and oligomers of 129M and 129V variants huPrP(23-230) and the 129M variant huPrP(121-230). The amount is the result of integration of $c(s)$distributions from SV analysis of 7.5 µM huPrP without GdnHCl at pH 2 (Supporting Figure 2.9).

can disrupt the salt bridge between R156 and E196, which acts as an anchor between helix1 and helix2/helix3, by interacting with E196 [204]. Furthermore, the solvent-accessible surface area (SASA) of H187 has been reported to increase in partially unfolded structures because H187 initially forms a hydrophobic core located between helix2 and helix3 with the residues P158, F198 and M206; the protonation of H187 decreases the hydrophobicity and potentially leads to a destabilization of this hydrophobic core [206]. Thus, we analyzed the mean values of the percentage of salt bridge formation between E196 and R156 and the SASA of H187 during our MD simulations. The results show a significantly higher percentage of salt bridge formation for the 129M polymorph (48.2 ± 9.0 % , 95 % confidence interval (CI): 27.9 % - 68.5 %) in comparison to the 129V polymorph (26.0 ± 5.5 %, 95 % CI: 13.5 % - 38.5 %). The mean values for both polymorphs differ significantly (p = 0.02; unpaired t-test) (Figure 2.2C). Furthermore, the SASA of H187 is significantly decreased in the 129M polymorph (34.6 ± 1.2 $Å^2$, 95 % CI: 31.8 $Å^2$ – 37.3 $Å^2$) compared to the 129V polymorph (40.7 ± 2.8 $Å^2$, 95 % CI 34.4 $Å^2$ – 47.0 $Å^2$) (p = 0.03; unpaired t-test) (Figure 2.2D), confirming the increased structural stability in this region for huPrP(118-224) (Figure 2.2E). The lower stability of the investigated 129V variant might favor amyloid formation by lowering energetic barriers considering the single amino acid exchange at position 129 [208].

Studies investigating the polymorphism at position 129 generally used a shorter construct of huPrP, lacking the unstructured N-terminal domain [35, 34]. To test the effect of the unstructured N-terminal domain on aggregation kinetics and oligomer formation, we compared a shorter construct of the 129M variant without the N-terminal half, huPrP(121-230), to our full-length proteins (Figure 2.3). The lack of the unstructured N-terminal domain of the 129M variant significantly alters the amyloid formation kinetics (Figure 2.3A). The shorter construct of the 129M variant does not present multiphasic, complex kinetics but shows an immediate onset of amyloid formation as already observed for the full-length 129V variant. SV experiments report a lower degree of oligomerization and a higher monomer content for huPrP(121-230) of the 129M variant compared to full-length huPrP(23-230) (Figure 2.3B and Supporting Figure 2.9). The monomer and oligomer content of the shorter 129M variant is similar to the full-length 129V variant, which agrees with the similarities found in amyloid formation kinetics. We conclude that the presence of the unstructured N-terminal region affects the structural properties of the protein, leading to significant changes in oligomerization and hence in amyloid formation kinetics.

2.6. Discussion

In summary, our study revealed clear differences in the pathway of amyloid formation at pH 2 of full-length huPrP(23-230) associated with the single Met/Val amino acid exchange at position 129, which provide insights into possible mechanisms underlying prion diseases. Additionally, we observed a significant impact of the unstructured, 98 amino acid long N-terminal region on the aggregation propensity of the 129M variant, superimposing the direct effect of the polymorphism at position 129. The deviating stability of both variants of huPrP(118-224) observed during MD simulations suggest a different unfolding behavior based on this polymorphism. We observed an initial ThT fluorescence plateau in kinetic measurements upon the addition of GdnHCl for the 129M variant. The early ThT signal supports an immediate formation of oligomers with partial binding sites for ThT, which was already reported for the 129M variant [209]. After the initial formation of aggregates, no further decrease of the soluble fraction was observed. As a consequence, the increase in ThT fluorescence leading to interim and final plateaus observed in the multi-phasic kinetics of the 129M variant originates from structural rearrangements of already existing larger oligomers. A stronger tendency for oligomerization of the 129M polymorphism was also observed in SV experiments without GdnHCl. The capability of larger oligomers to assemble into amyloid fibrils was previously shown for ovine PrP [210]. We conclude that the amyloid formation pathway for the 129M variant is different to the 129V variant and characterized by the presence of oligomeric intermediates undergoing further structural conversion. The increased population of non-native states but not yet fully amyloid structure

for the 129M variant might explain differences in pathology associated with this polymorphism. Interestingly, the existence of a detectable amount of dimers was already reported to interfere with the conversion of huPrP^{C} into huPrP^{Sc} [211]. Observed *s*-values appropriate for dimers in SV experiments were exclusively found for the 129M variant, providing a further explanation for higher resistance to amyloid formation and more complex kinetics.

The differences in structure and global stability of huPrP^{C} as a consequence of the polymorphism at position 129 were already investigated in NMR studies [35]. It was reported that the polymorphism at position 129 in a shorter construct excluding the unstructured N-terminal domain, huPrP(90-230), neither impacts on structure nor stability. It should be noted that the polymorphism was investigated at pH 5.5 At this pH, H187 is not completely in a protonated state. It was further reported that the polymorphism might affect amyloid formation kinetics or the formation of intermediates on the pathway of conversion of huPrP^{C} into huPrP^{Sc}. The overall structure of the C-terminal globular domain of huPrP(125-228) is not affected by constructs of different lengths but a transient contact between the flexible, unstructured N-terminal region and the globular C-terminal domain was observed in NMR studies [52]. The length of the unstructured, N-terminal region affects helix2 (187-193) and helix3 (219-226) in the globular domain. Hence, the usage of full-length huPrP(23-230) leads to a more complete picture of the underlying structural rearrangements by including the complete, flexible N-terminus.

This study aimed to investigate the differences between the two variants with regard to their aggregation propensity and possible amyloid formation pathways. We concluded an oligomer-mediated pathway for the 129M variant but could only observe such behavior for the full-length variant. The described data result as a consequence of both described effects, the exchange of a single amino acid as well as the presence of the N-terminal half, however, the effect of the single amino acid exchange seems to be superimposed by the depletion of the 98 amino acid long N-terminal half. Our results emphasize the relevance of the considered full-length huPrP(23-230) construct to perceive different aggregation propensities.

2.7. Material and methods

All experiments were performed at pH 2 in 10 mM aqueous HCl.

2.7.1 Expression and purification of human prion protein

Both recombinant huPrP(23-230) variants 129M and 129V as well as the huPrP(121-230) 129M variant were expressed and purified as previously described [212]. The protein folding following

this purification protocol and acidic pH was previously confirmed by NMR [212]. Final sample purity was confirmed by SDS-PAGE (Figure S1).

2.7.2 Amyloid formation kinetics

Amyloid formation kinetics of both huPrP(23-230) variants and huPrP(121-230) 129M variant were monitored by ThT fluorescence using a plate reader (BMG, Offenburg, Germany). ThT fluorescence was measured by excitation at 445 nm and detection at 485 nm. 15 µM and 20 µM huPrP with 0.5 M GdnHCl and 30 µM ThT were measured. The measurements were performed in triplicates in a 96-well plate (No. 3881, Corning) sealed with a plastic film at 37°C and continuous shaking at 300 rpm.

2.7.3 Circular dichroism spectroscopy

CD spectra of 10 M huPrP(23-230) for both variants were recorded in a Jasco J-815 (Jasco, Tokyo, Japan) spectropolarimeter at 20°C without GdnHCl and after 5 h in the presence of 0.5 M GdnHCl. Thermal stability was investigated over a temperature range from 20°C to 95°C. The thermal stability was investigated before amyloid formation of 10 µM huPrP(23-230). To investigate the thermal stability of the amyloid conformation, 100 µl were taken from amyloid formation kinetics of 20 µM huPrP(23-230) after 120 h and centrifuged at 15,000×g for 25 minutes and 20°C. The pelleted amyloid structures were dissolved in 100 µl 10 mM HCl (pH 2). A quartz glass cuvette with 1 mm path length was used. Spectra were measured at 50 nm/min with 2 nm bandwidth and 4 s digital integration time (D.I.T.). Spectral resolution was 1 nm and temperature resolution was 5°C. The temperature was increased with 2°C/min and 30 s waiting time before measurement. Ten accumulations were measured for each spectrum.

2.7.4 Analytical ultracentrifugation

Sedimentation velocity (SV) experiments were performed in an analytical ultracentrifuge Proteome Lab XL- A (Beckman-Coulter, Brea, US). Experiments included 7.5 µM huPrP. Samples were measured in standard double sector cells (Titanium) with an optical path length of 12 mm using an An-60Ti rotor. Temperature was set to 20°C. The speed was 60,000 rpm corresponding to about 260,000×g. Data analysis was performed using a continuous distribution Lamm equation model, $c(s)$, implemented in the software Sedfit (version 16p35) [213].

2.7.5 Molecular dynamics simulations

Structural information for PrP(118-224) 129M was taken from PDB entry 4N9O [214]. For the 129V polymorph, the amino acid at position 129 was mutated to valine using MOE, version 2019.01 [215]. We selected the energetically most favored rotamer and subsequently minimized the side chain; both polymorphs were protonated according to pH 2, and the N- and C termini were capped with NME and ACE, respectively, using MOE, version 2019.01 [215]. With a predicted pKa value of 2.09, E196 can be protonated or deprotonated at pH 2 [216]. As E196 forms a salt bridge with R156 in our starting structure, which stabilizes a negative charge at E196, it is likely that E196 is deprotonated in the starting structure. The polymorphs were then neutralized using Cl^- as counter ions and solvated in an octahedral box of OPC water [217] with a minimal water shell of 12 Å around the protein. The Amber package of MD simulation software [218] and the ff19SB force field [219] were used to perform MD simulations. For further details of our simulation methods, see supporting information and Figure 2.11.

2.7.6 Structural analyses

To ensure that the starting structures of both polymorphs do not influence the results, we removed the first 500 ns of MD simulations prior to the analyses. Every 5 ns, a frame was extracted from the trajectories using CPPTRAJ [220], and counter ions and water molecules were stripped. From the protein conformations, neighbor stability maps rcij,neighbour were calculated using CNA [201]. CNA is a software package that functions as front- and backend for the FIRST software and helps to analyze structural features critical for protein stability; neighbor stability maps are derived from all extracted trajectories along the simulation and contain information about the persistence of rigid contacts between pairs of residues [221, 201]. In order to exclude pairs of structurally non-neighboring residues, only interactions were considered in rcij,neighbour where at least one of the pairs of heavy atoms of the residue pair R(i,j) is separated by less than 5 Å. The chemical potential energy ECNA, a measure for thermostability, was calculated according to equation 2.1 as done previously [202].

$$E_{C,N,A} = \sum_{i}^{n} \sum_{j>i}^{n} rc_{ij,neighbor} \tag{2.1}$$

The distance between the carboxy oxygens of E196 and the side chain nitrogen atoms of R156 was calculated using the nativecontacts mindist command as implemented in CPPTRAJ [220]. We consider a salt bridge formed if the distance between respective charged heavy atoms is <4 Å [222]. The SASA of H187 was analyzed using the surf command as implemented in CPPTRAJ [220]. We calculated the one-sided t-test for both measurements with the null hypothesis that

the values of the two stability-indicating measurements are in favor of the more stable 129M polymorph.

2.8. Supporting information

2.8.1 Supporting methods

Molecular dynamics simulations

Molecular dynamics simulations were performed using the ”Particle Mesh Ewald” method to consider long-range interactions; the SHAKE algorithm was applied to bonds involving hydrogen atoms [223]. The time step during thermalization and equilibration was set to 2 fs with a direct-space, non-bonded cutoff of 9.0 Å; the time step during the production runs was set to 4 fs as hydrogen mass repartitioning was used with a direct-space, non-bonded cutoff off 8.0 Å [224]. First, 102,500 steps of steepest descent and conjugate gradient minimization were performed; during 2,500, 50,000, and 50,000 steps positional harmonic restraints with force constants of 5 kcal×mol^{-1}×Å^{-2}, 1 kcal×mol^{-1}×Å^{-2}, and 0 kcal×mol^{-1}×Å^{-2}, respectively, were applied to the protein atoms. Then, 50 ps of NVT-MD (constant number of particles, volume, and temperature) were performed to heat the system to 100 K, followed by 250 ps of NPT-MD (constant number of particles, volume, and temperature) simulations to heat the system to 300 K and to adjust the density of the simulation box to a pressure of 1 atm. During these steps, a harmonic potential with a force constant of 1 kcal×mol^{-1}×Å^{-2} was applied to protein atoms. Thereafter, 300 ps of NVT-MD simulations were conducted. During the first 250 ps of this step, the harmonic restraints were gradually reduced to zero. Then, ten independent replica of MD simulation production runs of 1 µs length were performed for each polymorph. The starting temperature of each run was varied by a fraction of a Kelvin.

To ensure that the dihedral angle of the mutated side chain does not impact the outcome of the MD simulations, we analyzed the dihedral angle between the planes defined by N, CA, CB and CA, CB, CG1 during the MD simulations using CPPTRAJ [220] (Figure 2.11). As all favored dihedral angles are found in this analysis (180°, -60°, and 60°) and there are frequent exchanges between these states, indicating that the side-chain of V129 is in equilibrium, the starting conformation of valine at position 129 should not influence the results. To be noted, the MD simulations do not include the glycosylation of the protein, as all experiments were performed with unglycosylated huPrP.

UV/Vis-absorbance measurement

UV/Vis-absorbance of soluble fraction was measured for both huPrP(23-230) variants during amyloid formation using the UV-1900i UV-VIS-Spectrophotometer (Shimadzu, Kyōto, Japan). 15 µM huPrP with 0.5 M GdnHCl were used. Samples were incubated in 1.5 ml Lobind Eppendorf tubes, at 37°C and continuous shaking at 300 rpm. After 1 h, 5 h, 19 h, 55 h, 96 h and 120 h, 100 µl was taken and centrifuged (30 minutes, 15,000×g, 25°C). The supernatant was used to measure the remaining monomer and small oligomer content. The measurement was performed in duplicates in a quartz glass cuvette with 1 mm path length.

2.8.2 Supporting results

Different protein concentration and GdnHCl concentrations reveal distinct amyloid kinetics Different conditions were investigated for the amyloid formation kinetics. Supporting Figure 2.5 shows a concentration series of different GdnHCl concentrations with 15 µM of huPrP(23-230) 129M variant. These results indicate that a certain amount of GdnHCl is needed for sufficient destabilization and initialization of amyloid formation. The amount should not be too high to enable seed formation. Additionally, a concentration series with relatively low concentrations of both variants was established with a constant ratio of GdnHCl (Supporting Figure 2.6). Supporting Figure 2.7 confirms the importance of a certain huPrP/GdnHCl ratio for the 129M variant, as the lowest protein concentration tested with the highest applied GdnHCl concentration shows a significantly delayed fluorescence increase. For the highest protein concentration, the amount of GdnHCl alters the fluorescence signal of the initial plateau as well as the time of increase and duration of the interim and final plateau.

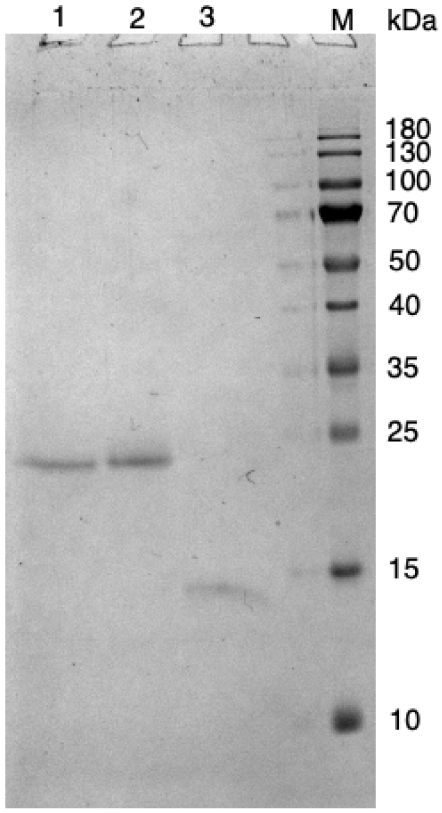

Figure 2.4: Final purity of huPrP constructs. Coomassie stained 15 % Tris/Glycine SDS-PAGE of 3 µM huPrP. 1, huPrP(23-230) 129V; 2, huPrP(23-230) 129M; 3, huPrP(121-230) 129M; M, marker protein.

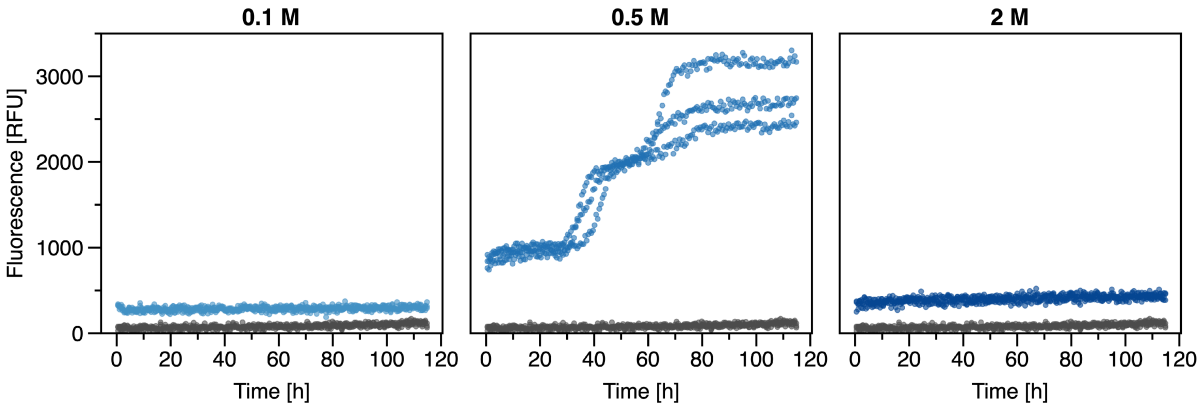

Figure 2.5: Destabilization of huPrP. Amyloid formation kinetics monitored by ThT fluorescence of 15 µM huPrP(23-230) 129M variant in the presence of different GdnHCl concentrations at pH 2. huPrP(23-230) 129M without GdnHCl shows no amyloid formation (grey).

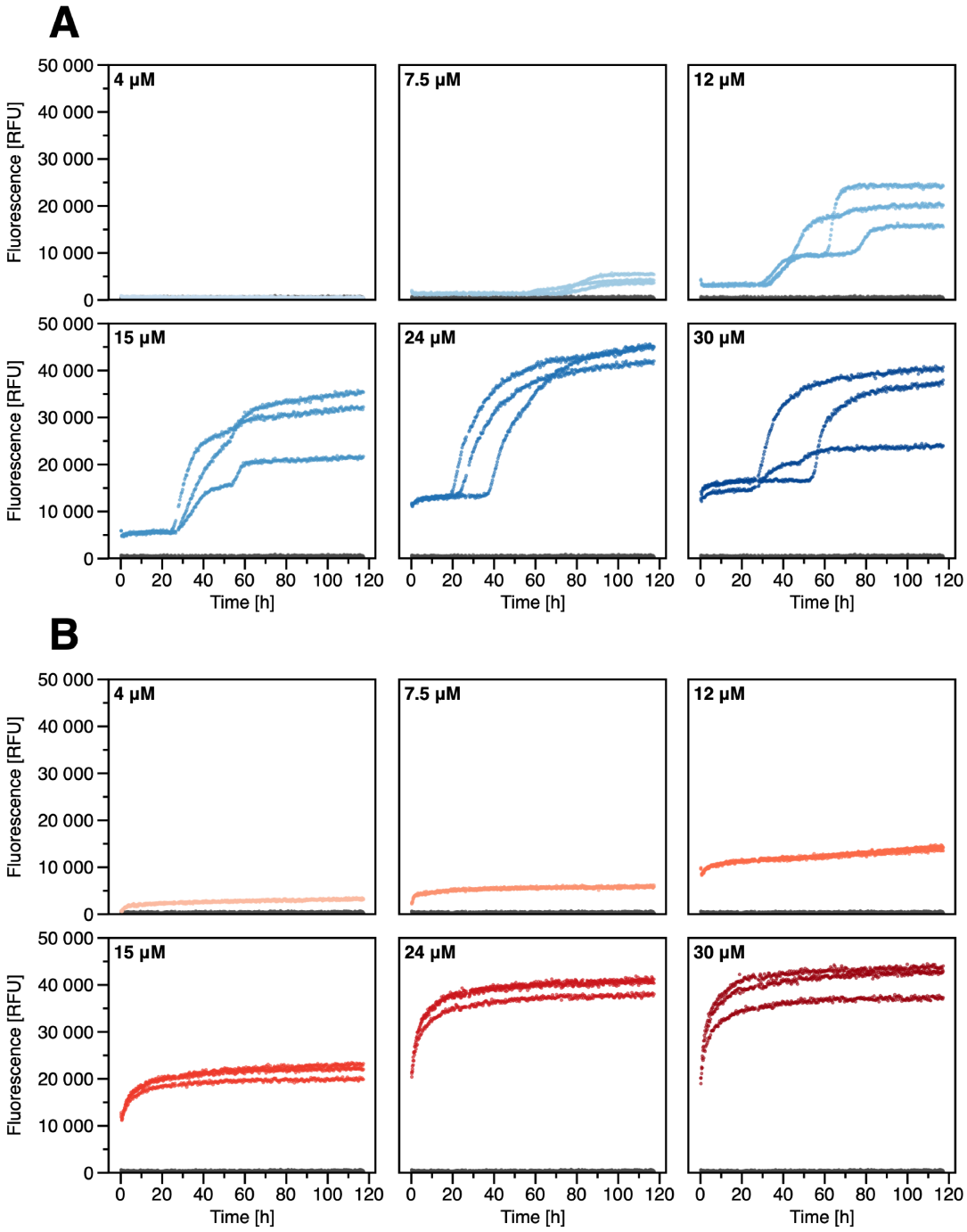

Figure 2.6: Concentration series of huPrP. (A) Amyloid formation kinetics monitored by ThT fluorescence of different huPrP(23-230) concentrations for the 129M variant and (B) 129V variant at pH 2. The ratio between protein and GdnHCl is constant at 1 to 33,333. HuPrP(23-230) without GdnHCl shows no amyloid formation (grey).

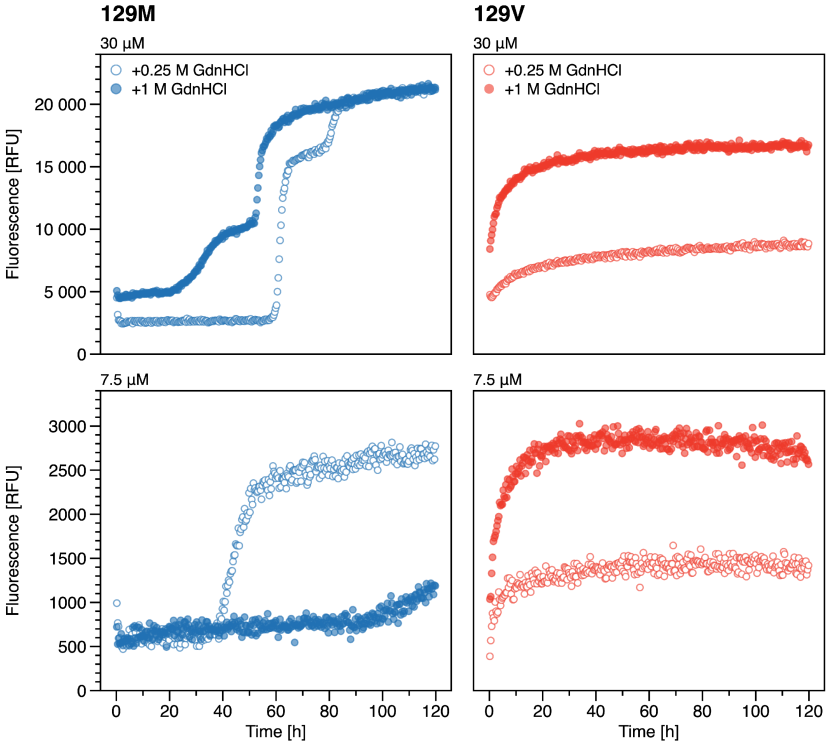

Figure 2.7: Comparison of different huPrP and GdnHCl concentrations. Amyloid formation kinetics monitored by ThT fluorescence of 7.5 µand 30 µM huPrP(23-230) for both variants in the presence of 0.25 M and 1 M GdnHCl at pH 2.

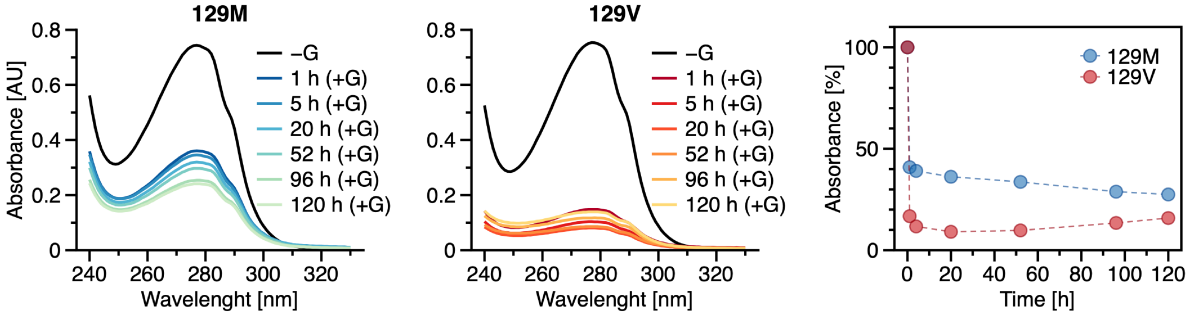

Figure 2.8: Soluble fraction during amyloid formation. Absorbance spectra of 15 µM huPrP (23-230) 129M and 129V variant at pH 2. Spectra were measured before amyloid formation without GdnHCl and after 1 h, 5 h, 19 h, 55 h, 96 h and 120 h during amyloid formation in the presence of 0.5 M GdnHCl. Left and middle graphs show the absorbance plotted against the wavelengths (in nm) for the 129M and the 129V variant, respectively. Right graph represents the relative absorbance (in %) plotted against the time (in h).

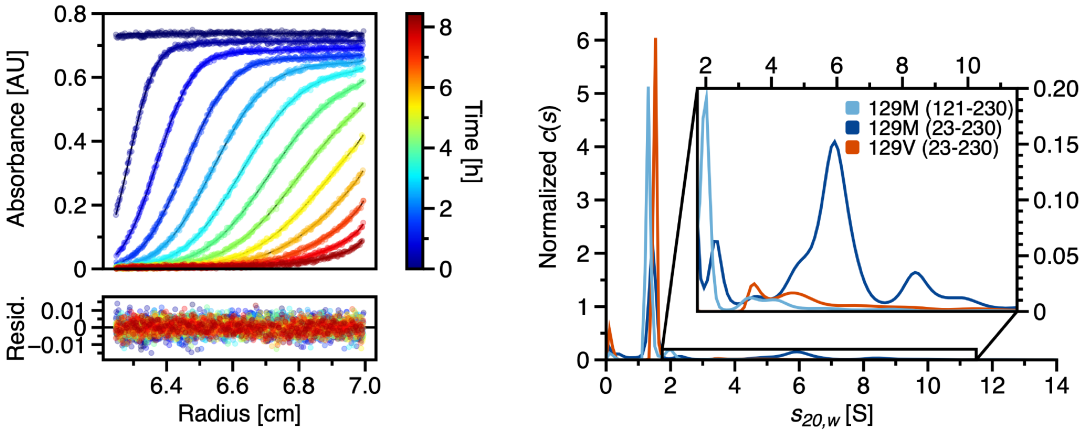

Figure 2.9: Impact of the unstructured N-terminal region on oligomerization. (A) Comparison of results from SV analysis of 7.5 µM of the 129M variant huPrP(121-230) (light blue) and huPrP(23-230) (dark blue) and the 129V variant huPrP(23-230) (orange) at pH 2. Raw data of the 129M variant huPrP(121-230) with fitted Lamm-equation solutions from $c(s)$ model are color-coded for the duration of sedimentation. (B) The result of data fitting is an s-value distribution. The distributions of huPrP(23-230) for both variants are shown for comparison.

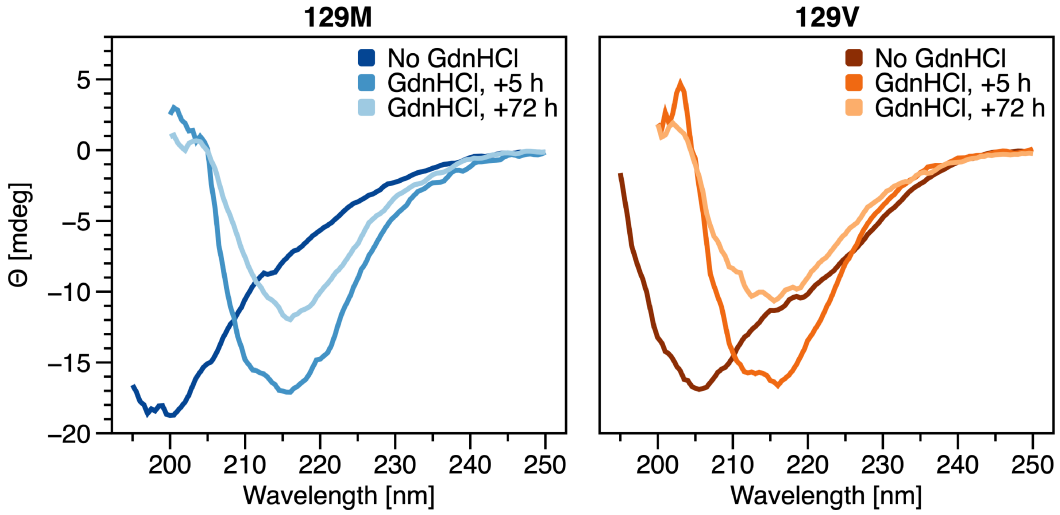

Figure 2.10: Secondary structure content before and during amyloid formation. CD spectra of 10 µM huPrP(23-230) 129M and 129V variant at pH 2. Spectra were measured before amyloid formation without GdnHCl and after 5 and 72 h during amyloid formation in the presence of 0.5 M GdnHCl.

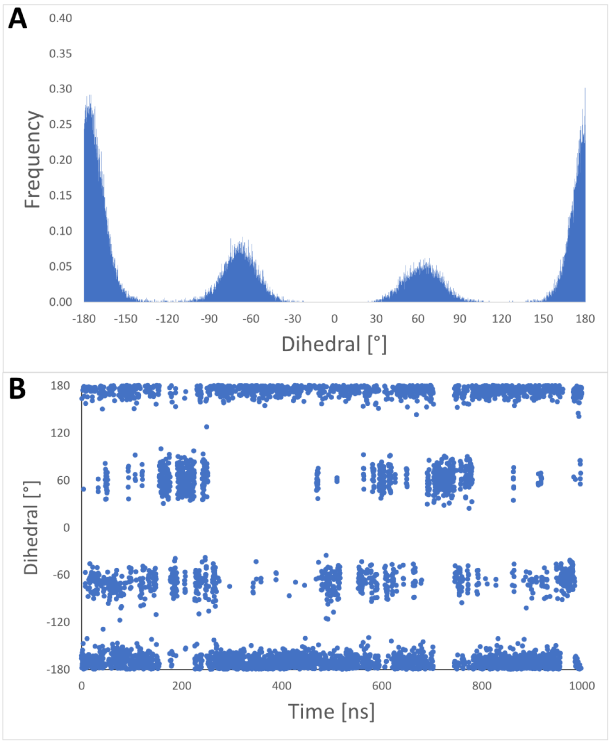

Figure 2.11: Dihedral angles. (A) Frequency distribution of dihedral angles in all replicas and (B) appearance of the dihedral angle over time during one replica; the dihedral angle was determined between the planes spanned by N, CA, CB and CA, CB, CG1 during MD simulations.

3

HIGH-LEVEL EXPRESSION AND PURIFICATION OF NATIVE-LIKE HUMAN PRION PROTEIN USING *Leishmania tarentolae*

3.1. Article information

Title of manuscript: High-level expression and purification of native-like human prion protein using *Leishmania tarentolae*

Authors: Najoua Bolakhrif[1,2], Lothar Gremer[1,2], Thomas Pauly[1,2], Ci Chu[1], Luitgard Nagel-Steger[1,2], and Dieter Willbold[1,2,*]

Status: in preparation (January 2022)

[1] Institut für Physikalische Biologie, Heinrich-Heine-Universität Düsseldorf, 40225 Düsseldorf, Germany

[2] Institute of Biological Information Processing (IBI-7: Structural Biochemistry), Research Center Jülich, 52425 Jülich, Germany

[*] d.willbold@fz-juelich.de

3.2. Declaration of article contributions

3.2.1 Experimental

Cultivation, transfection, expression, and purification was performed by me. Characterization including, CD measurements and enzymatic digestions with subsequent western blot analysis was performed by me.

3.2.2 Data analysis

Data analysis was performed by me and Thomas Pauly.

3.2.3 Manuscript preparation

All figures were prepared by me and Thomas Pauly. I wrote the complete manuscript in collaboration with Lothar Gremer, Thomas Pauly, Ci Chu, Luitgard Nagel-Steger, and Dieter Willbold.

3.3. Abstract

The human prion protein (PrP) is a GPI-linked membrane-bound glycoprotein, containing two glycosylation sites. Human PrP is associated with a number of neurodegenerative diseases, called transmissible spongiform encephalopathies (TSE). Pathogenesis involves a structural conversion of the cellular form (PrP^{C}), rich in α-helical and random coil structure, into the scrapie form (PrP^{Sc}) characterized by β-sheet conformation. To get a better understanding of this structural conversion, it is crucial to first characterize the non-pathogenic cellular isoform including all post-translational modifications, like GPI-anchoring and native-like human glycosylation pattern. So far, studies on PrP^{C} or PrP^{Sc} as well as the transition from one state to the other rely on non-native constructs of PrP studied far away from physiological conditions. We, therefore, established the expression of GPI-linked human PrP with close to native glycosylation pattern (native-like human PrP) using the eukaryotic expression system *Leishmania tarentolae*. This expression system has the added advantage that it allows for large-scale production of the native-like human PrP, which results in 1 mg purified protein per liter culture. Sedimentation velocity analysis and circular dichroism spectroscopy confirm high homogeneity and the proposed conformation of the purified native-like human PrP.

3.4. Introduction

The human prion protein (huPrP) consists of 253 amino acid residues and is a membrane-bound glycoprotein mainly located in the nervous system. It is most known for its direct involvement in a number of neurodegenerative diseases including Creutzfeldt-Jakob's disease. These prion diseases are transmissible spongiform encephalopathies (TSEs) involving the abnormal accumulation of misfolded huPrP as amyloid fibrils [54]. Prions are infectious, misfolded aggregates of the prion protein that are partially resistant to proteinase K digestion and further have the ability to transfer structural identity to recruit native protein by autocatalytic processes [225, 32]. The native, or cellular form of huPrP ($huPrP^{C}$) is characterized mainly by α-helical and random coil structural elements [52]. The first 22 amino acid residues of the N-terminal domain are responsible for the transport to the endoplasmic reticulum (ER) [53]. Adjacent to the transport signal sequence is an unstructured (random coil) region known as the hydrophobic N-terminal domain which comprises five octameric repeats (amino acid residues 23 to 127). A small anti-parallel β-sheet (amino acid residues 128 to 131 and amino acid residues 161 to 164), represents about 3 % of the total structure [52, 187]. The C-terminal domain has approximately 42 % α-helical structure, including helix 1 (amino acid residues 144 to 154), helix 2 (amino acid residues 173 to 194), and helix 3 (amino acid residues 200 to 228). Lastly, membrane attachment is achieved *via* a glycosylphosphatidylinositol (GPI)-anchor present at the C-terminal end (amino acid residues 231 to 253) with a molecular weight of approximately 2 kDa [76]. The total size of huPrP varies between approximately 30 and 35 kDa, depending on the number of glycans at glycosylation sites N181 and N197 (excluding the GPI anchor). The native structure of mainly α-helices and random coil holds for the cellular isoform ($huPrP^{C}$), however, the misfolded form, or scrapie ($huPrP^{Sc}$), is dominated by β-sheet structure [187, 226]. The details of this structural conversion of $huPrP^{C}$ into $huPrP^{Sc}$ still remains elusive. Recent studies suggest that spontaneous conversion occurs in close proximity to the cell membrane [227]. Interestingly, experiments on full-length PrP where the GPI-anchor was excluded do not show any spontaneous conversion under physiological conditions [82, 79, 228]. As a consequence, studies focusing on the full-length huPrP made use of destabilization by acidic pH or denaturants to induce the amyloid formation [229, 230]. An alternative approach has been to exclude the globular C-terminal domain and use shorter constructs of huPrP to facilitate the spontaneous conversion of the unstructured N-terminal region from an unstructured monomeric state into an amyloid state [231]. Furthermore, investigations on the conversion of $huPrP^{C}$ into $huPrP^{Sc}$ usually rely on bacterially expressed recombinant huPrP, lacking post-translational modifications (PTMs). Expression systems involving PTMs commonly rely on *Pichia pastoris*, but the glycosylation patterns are clearly different from mammalians [232, 233]. To overcome these shortages, we

established the expression of the membrane-bound full-length huPrP^C with human-like PTMs in the eukaryotic trypanosomatid parasite *Leishmania tarentolae*. *L. tarentolae* is one of the very few expression systems providing glycosylation patterns similar to those in humans, except for missing the terminal sialic acid [234, 88]. We found *L. tarentolae* to be an appropriate eukaryotic expression system for producing large quantities of homogeneous, fully processed huPrP^C for accurate studies on the structure and conversion underlying human prion diseases. Several studies support the capability of *L. tarentolae* to yield biologically active eukaryotic proteins as well as mammalian-like N-glycans [175, 235, 236]. Hence, we aim to introduce this new expression system for native-like huPrP^C, including its purification and confirmation of homogeneity and conformation by sedimentation velocity analysis and circular dichroism spectroscopy. This work intends to improve the understanding of human prion diseases by bringing *in vitro* studies closer to physiological conditions.

3.5. Results

3.5.1 Vector design and expression of native-like huPrP^C

The full-length huPrP sequence including the N-terminal and C-terminal signal sequences was cloned into the *L. tarentolae* expression vector pLEXSY-neo 2.1. The flexible N-terminal region contains a signal sequence, responsible for the transport to the ER. After the N-terminal signal sequence, we inserted a 6× histidine tag (His-tag) followed by a factor Xa cleavage site (3.1A). This allows for purification and subsequent cleavage of the His-tag. To guarantee the permanent genomic integration of the huPrP sequence, the expression cassette was integrated into the *odc* locus of chromosome 12 of *L. tarentolae*. The integration was confirmed by diagnostic PCR, after the preparation of genomic DNA from a dense culture, resulting in 1.1 kbp and 2.4 kbp characteristic fragments for the positive clones. Clones that were not genome-integrated did not show bands with respective sizes (Figure 3.1B). After induction of expression of native-like huPrP with tetracycline, SDS-PAGE and western blot of the cells as well as of the culture supernatant was performed. This revealed intracellular expression with no secretion of the protein into the culturing medium (Figure 3.1C). Furthermore, a background expression was detected, without induction, enabling the selection by geneticin, G-418. Enzymatic digestion using phospholipase C (PI-PLC), which is a phosphatidylinositol-specific enzyme, was used to confirm membrane anchoring by cleaving off the GPI-anchor. This resulted in native-like huPrP released into the supernatant after centrifugation, while no treatment showed only signal in the cell pellet (Figure 3.1D). Moreover, the western blot revealed multiple bands between 25 kDa and 35 kDa, which are characteristic for cellular and glycosylated huPrP (Figure 3.1D). Lastly,

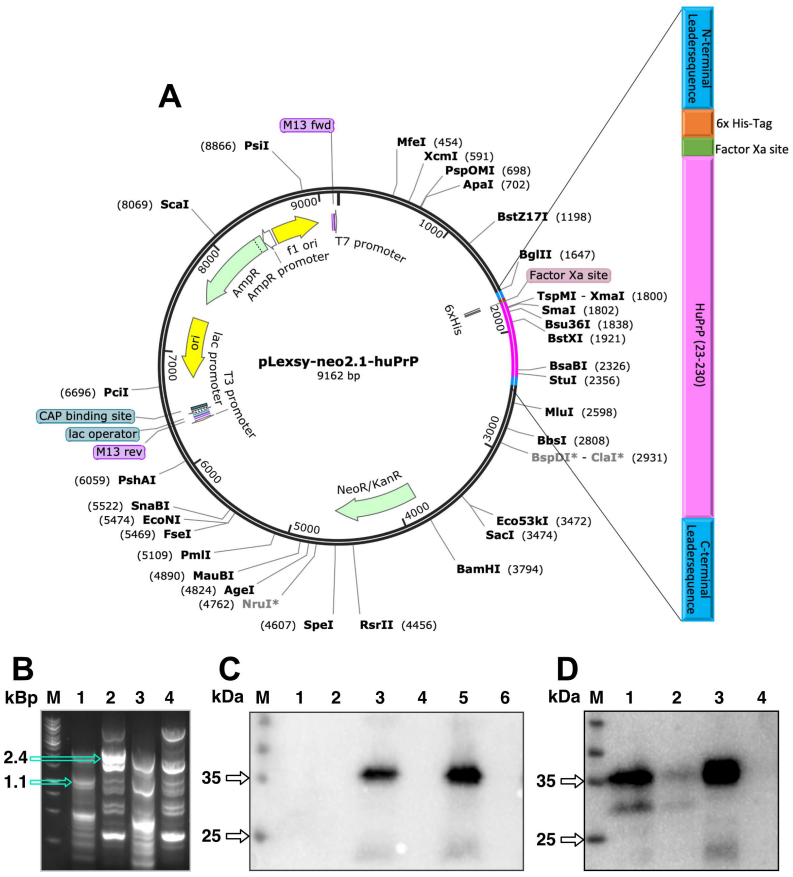

Figure 3.1: Human prion protein: cloning and expression in *L. tarentolae*. (A) Gene map of the pLexsy neo.2.1 vector including the human prion protein sequence, inserted using the restriction sites NcoI/ NotI. (B) Confirmation of genome integration by diagnostic PCR. 1: Positive clone, control region: 5'*odc* – *utr*1 resulting in fragment size of 1.1 kBp; 2: Positive clone, control region: neo – 3'*odc* resulting in fragment size of 2.4 kBp; 3: Negative clone, control region: 5'*odc* – *utr*1; 4: Negative clone, control region: neo – 3'*odc*. (C) Evaluation of human prion protein expression by western blot. 1: cellular detection of human prion protein in *L. tarentolae* before vector integration; 2: secretory detection of human prion protein in *L. tarentolae* before vector integration; 3: cellular detection of human prion protein in *L. tarentolae* after vector integration and before induction with tetracycline; 4: secretory detection of human prion protein in *L. tarentolae* after vector integration and before induction with tetracycline; 5: cellular detection of human prion protein in *L. tarentolae* after vector integration and after induction with tetracycline; 6: secretory detection of human prion protein in *L. tarentolae* after vector integration and after induction with tetracycline. (D) Characterization of post-translational modifications of human prion protein expressed in *L. tarentolae* by western blot. 1: Pellet of *L. tarentolae* expressing native-like huPrP after 1 h treatment with PI-PLC; 2: Supernatant of *L. tarentolae* after 1 h treatment with PI-PLC; 3: Pellet of *L. tarentolae* expressing native-like huPrP without treatment with PI-PLC; 4: Supernatant of *L. tarentolae* without treatment with PI-PLC.

proteolysis of the expressed native-like huPrP with proteinase K shows no resistance to digestion supporting the cellular conformation (Figure 3.4).

3.5.2 Solubilization and purification of native-like huPrP^C

Since huPrP is linked to the membrane *via* a GPI-anchor, differential centrifugation was applied after cell disruption to obtain the membrane fraction. A final step of 100.000 $\times$g is applied to pellet the membrane fraction (see methods for further details). To prevent aggregation, membrane proteins are usually transferred from the native cellular membrane to membrane mimetics. Several detergents were tested for the ability to solubilize native-like huPrP (Figure 3.5). n-Dodecyl-β-D-maltoside (DDM) is the detergent of choice. It is a mild and non-denaturing detergent, which is often able to preserve the correct protein folding, with a relatively high critical micellar concentration (0.08 mM in a NaCl solution), which is crucial for subsequent removal and replacement of the detergent [237]. Lastly, the optical properties of DDM do not interfere with most spectroscopic methods commonly used to study protein structure and hydrodynamic properties, unlike Triton X-100 or NP-40. After solubilization, native-like huPrP was purified using immobilized metal affinity chromatography (IMAC). Applying an imidazole gradient for elution resulted in a prominent peak containing native-like huPrP (Figure 3.2A). The fractions corresponding to the peak from the IMAC were then subjected to size exclusion chromatography (SEC) where two major peaks with retention volumes of approximately 10 ml and 15 ml were seen (Figure 3.2B). Using a dot blot, the second peak was found to contain native-like huPrP (Figure 3.6). The purity after each step was analyzed by semi-denaturing SDS-PAGE and subsequent Coomassie staining. After the IMAC, a prominent band at around 40 kDa, corresponding to huPrP, is present (Figure 3.2C). After SEC, most of the remaining impurities were removed resulting in only one apparent band at approximately 40 kDa. It should be noted that since huPrP is incorporated in DDM micelles, the samples could not be heated to 95°C, as is commonly done in preparing samples for SDS-PAGE but were instead loaded onto the gel directly after the addition of reducing SDS-PAGE sample buffer. The consequence is a slightly increased molecular mass of huPrP (40 kDa versus 30-35 kDa), which is a typical hallmark for membrane proteins [238] (Figure 3.2C). UV-Vis absorbance spectroscopy of the purified native-like huPrP shows a distinctive profile with two local maxima at 273 nm and 283 nm, while the full-length huPrP expressed in *E. coli* shows a characteristic profile with one major peak at 280 nm (Figure 3.7). The described purification protocol yielded 0.63 mg of highly pure native-like huPrP from a 600 ml *L. tarentolae* culture. The hydrodynamic properties and protein conformation were further analyzed using biophysical methods.

3.5.3 Biophysical characterization of native-like huPrP

When studying recombinant huPrP from *E. coli*, it is common to shift the pH towards more acidic values, considerably away from a physiological relevant value, in order to ensure solubility

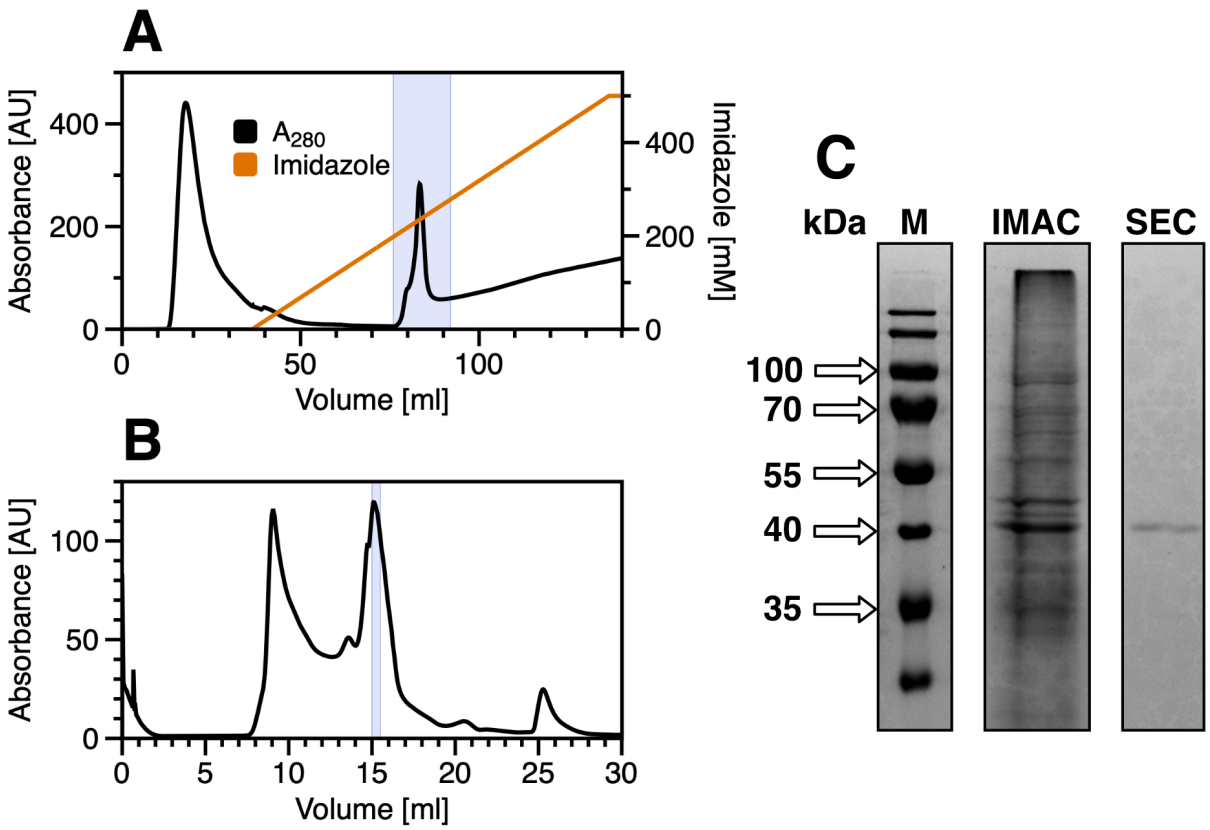

Figure 3.2: Isolation and purification of recombinant human prion protein produced in *L. tarentolae*. (A) Purification by immobilized metal affinity chromatography (IMAC) after solubilization of the membrane fraction. Absorbance at 280 nm and imidazole concentration is plotted against the elution volume. The peak including human prion protein is highlighted in light blue. (B) Purification of the highlighted IMAC peak by size exclusion chromatography (SEC). Absorbance at 280 nm is plotted against the elution volume. Peak including human prion protein is highlighted in light blue. (C) Determination of purification by Coomassie-stained SDS-PAGE of the highlighted peaks after IMAC and SEC.

[239, 240]. It should be noted that the secondary structure of recombinant huPrP from *E. coli* at pH 4.5 was previously studied by NMR spectroscopy, which revealed that the protein mainly adopted a structure composed of α-helical and random coil elements with a single small antiparallel β-sheet [52]. For investigating the secondary structure of purified native-like huPrP from *L. tarentolae* solubilized in DDM micelles, CD spectra were recorded at physiological pH (pH 7.4) and compared to full-length huPrP expressed in *E. coli* under similar conditions (Figure 3.3A). The spectra of native-like huPrP show negative bands at 208 nm and 222 nm, typical for α-helical structure [241]. Due to buffer absorbance at low wavelength, it was not possible to analyze typical bands below 200 nm. As disordered proteins have a slightly positive

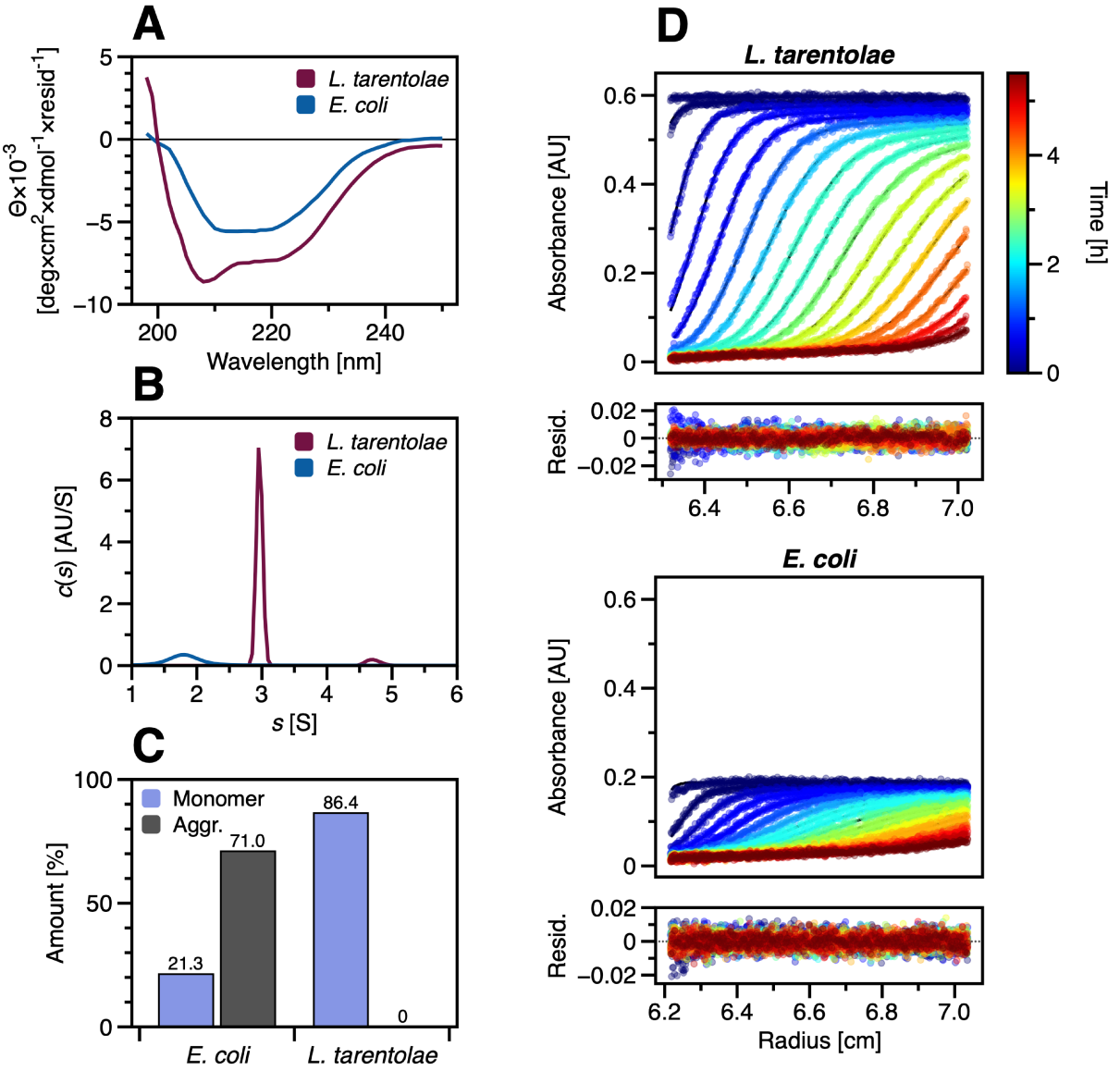

Figure 3.3: Analytical comparison of human prion protein from *L. tarentolae* and *E. coli*. (A) CD spectra of 10 µM of human prion protein from *L. tarentolae* (purple) and *E. coli* (blue). (B) The result of fitting sedimentation profiles is a distribution of *s*-values. (C) Integration of s-value distributions yields fractions of the sample. The loss of signal during acceleration of the centrifuge gives rise to the aggregate amount. (D) Sedimentation profiles of 10 µM protein show raw data as points with fitted Lamm-equation solutions as lines from SV experiments. The timestamp of each scan is color-coded.

signal above 210 nm, this structural element could contribute to the observed CD spectrum reporting on weighted average protein structure. In comparison, full-length huPrP from *E. coli* was not fully soluble using the same buffer conditions with physiological ionic strength (50 mM

Tris-HCl, 150 mM NaCl, pH 7.4). Therefore, the experimental conditions were shifted to 10 mM Tris-HCl, pH 7.4 for CD measurements of full-length huPrP from *E. coli*. Full-length huPrP shows a higher fraction of β-sheet structure under these conditions, indicated by a shift of the two negative bands closer to 218 nm, which is the typical minimum for β-sheet structure. The structure comprises a mixture of α-helical, random coil and β-sheet structure with increased β-sheet content compared to native-like huPrP. The hydrodynamic properties of native-like huPrP and full-length huPrP were studied by sedimentation velocity (SV) experiments at identical physiological conditions (Figures 3.3 B, C, and D). The majority of native-like huPrP is detected at an apparent sedimentation coefficient (*s*-value) of 2.96 S with a calculated mass appropriate for the monomeric protein (86.4 % of total signal). The remaining signal accounts for a larger species at 4.72 S with a calculated mass appropriate for a dimer. In contrast to native-like huPrP from *L. tarentolae*, full-length huPrP from *E. coli* suffers from reduced solubility at physiological pH and salt concentration. Full-length huPrP from *E. coli* showed a majority of large aggregates (71.0 % of total signal), which was determined as a loss of signal during acceleration of the centrifuge. The major part of the remaining soluble fraction was detected at 1.81 S with a calculated mass appropriate for the monomeric protein (21.8 % of total signal).

3.6. Discussion

The most frequent prion disease in humans is sporadic Creutzfeldt-Jakob disease, which involves the spontaneous conversion of huPrP^{C} into huPrP^{Sc} [242]. However, genetic predisposition is known to affect susceptibility to certain prion diseases [190]. To understand the onset of the disease, it is crucial to understand the mode of action in detail that leads to the structural conversion of the native protein. The pathological isoform, PrP^{Sc}, has been investigated by several studies, revealing its highly stable amyloid structure [54, 243, 244]. Most of these studies suffer from a trade-off between two drawbacks: First, high protein yields are available from recombinant production using *E. coli*, which consequently lacks conformity with PrP found in humans; or second, relevant PTMs are present, which usually come with the cost of low protein yields, e.g. *ex vivo*. Another approach, which is no less important, focuses on the structural properties of the cellular isoform and its misfolding. This approach encounters further obstacles to overcome, including the solubility of full-length huPrP expressed in *E. coli* at physiological pH. To avoid these problems, most studies focused on the investigation of shorter constructs of PrP [196, 195], PrP from other species [210], or lowered pH [196, 229]. Despite the fundamental insights that such *in vitro* studies revealed regarding the protein structure and misfolding mechanisms, there is an obvious discrepancy to *in vivo* conditions. *In vitro* studies applying high-resolution structural methods are in urgent need of closing the gap to physiological

conditions to yield significant advances in understanding prion diseases. So far, NMR studies revealed a predominantly α-helical structure of the cellular isoform, although these experiments were also conducted at an acidic pH (pH 4.5) [52]. At physiological conditions using CD spectroscopy, we were not able to observe such secondary structure for full-length huPrP from *E. coli*, but only for native-like huPrP from *L .tarentolae* including membrane-anchoring. It should be noted that full-length huPrP from *E. coli* is not completely soluble under these conditions, so CD spectra might report on the secondary structure of a mixture of oligomers or aggregates in solution. The advantage of improved solubility and a low amount of aggregates and oligomers is supported by SV experiments, revealing the monomer as the most prevalent species (86 % of total signal) for native-like huPrP from *L. tarentolae*. In contrast, full-length huPrP from *E. coli* was reported to involve only a small number of monomers (21.8 % of total signal) and a large number of aggregates (about 71.0 % of total signal), which sediment already during acceleration of the centrifuge. From that we conclude that native-like huPrP expressed in *L. tarentolae* is superior to full-length huPrP expressed in *E. coli* with regard to studies under physiological conditions. We demonstrated that native-like huPrP expressed in *L. tarentolae* combines the desirable advantages of high protein yields with PTMs that are close to their human counterparts. To be noted, the 6× His-tag was not removed, as we do neither expect it to have an influence on the overall protein stability, like it was shown for PrP by NMR [245] nor on the structure, like it was shown for Sup35 [246]. A purification protocol was presented, which yields highly pure native-like huPrP solubilized in DDM micelles, where the vast majority is in a monomeric state. Furthermore, these conditions allow for direct transfer into controlled membrane environments such as nanodiscs, as previously shown for the ion-channel accessory subunit barttin[247]. Isotopic labeling of native-like huPrP for NMR studies in *L. tarentolae* could likely be employed by already established protocols for this organism [248, 249]. Thus, by elucidating structural details of native-like huPrP^{C} in its physiologically relevant environment, the way for future studies on disease-related processes as conversion into PrP^{Sc} and mediation of other neurodegenerative diseases by interaction with disease-related proteins is paved.

3.7. Material and methods

3.7.1 Cloning of huPrP and amplification of pLEXSY_l-neo2.1

The sequence was designed as shown in Figure 3.1A. HuPrP DNA coding sequence (129 Met variant of the naturally occurring polymorphism) was optimized to *L. tarentolae* codon usage (GeneArt—ThermoFisherScientific). Gene synthesis and cloning into the pLEXSY_l-neo2.1 vector, using NcoI/NotI cloning sites, was performed by the company GenScript. NcoI is used for intra-

cellular expression, while NotI was chosen to remove the 6xHis stretch from the backbone. Flanking regions of 5' CC and 3' GCGGCCGC were added to form NcoI and NotI sites on the insert. For plasmid amplification, competent XL-1 *E. coli* were transformed with 0.8 µg plasmid. Recombinant *E. coli* clones were selected using ampicillin at 30 °C for plasmid stability reasons. Plasmid identity was confirmed by sequencing (Mycrosynth) using 5'-CCGACTGCAACAAGGTGTAG-3' as forward primer and 3'-CATCTATAGAGAAGTACACGTAAAAG-5' as reverse primer. After sequence confirmation, 9 µg plasmid was purified from a 50 ml *E. coli* culture using the QIAGEN Plasmid Midi Kit (cat. no. 12143).

3.7.2 Preparation of the expression plasmid for transfection of *L. tarentolae*

The huPrP was expressed using the inducible LEXSY expression system according to the manufacturer's instructions (LEXSinduce Expression Kit, Jena Bioscience). 9 µg pLEXSY_l-neo2.1 plasmid including the huPrP gene was digested using SwaI, to remove the 2 kbp *E. coli* fragment. Efficiency was confirmed by Agarose gel electrophoresis. Enzymes and buffer salts were subsequently removed using the Macherey-Nagel NucleoSpin Gel and PCR Clean-up Kit (cat. no. 740609) and eluted using 50 µl 10 mM Tris buffer, pH 8. The remaining linearized expression cassette was used for the transfection of *L. tarentolae*.

3.7.3 Cultivation and transfection of *L. tarentolae*

Culturing of *L. tarentolae* was performed according to the manufacturer's instructions (LEXSinduce Expression Kit, cat. no. EGE-245). Briefly, *L. tarentolae* was cultured in BHI medium, supplemented with hemin, Pen-Strep, nourseothricin (NTC), and hygromycin (Hygro) were added for the maintenance of T7-TR polymerase, and TET repressor genes. Culturing of 10 ml cultures was performed in 75 cm^2 ventilated tissue culture flasks at 26 °C in the dark and under aerated conditions. For the cultivation pre- and post-electroporation, 10% FCS was added. After an optical density of 1.3 (approx. 6 x 10^7 cells) was reached, the cells were centrifuged at 2000 $\times$g, RT for 3 minutes, and resuspended in half of the remaining medium. Cells, plasmid, and electroporation cuvette with a path length of 2 mm were incubated on ice for 10 min. 350 µl cells were mixed with 50 µl plasmid and incubated in the electroporation cuvette for 10 min on ice. Electroporation was conducted at 450V, 450 µF, for 3.76 msec. After another incubation step on ice for 10 min, the electroporated cells were transferred into a 75 cm^2 ventilated tissue culture flask, containing 10 ml BHI medium (+ hemin, NTC, Hygro, Pen-Strep, and 10% FCS). Electroporated cells were incubated at 26 °C in the dark for 6 hours before 5 ml of the culture was diluted into 15 ml BHI medium (+ hemin, NTC, Hygro, Pen-Strep, 10% FCS, and 50 µg/ml selection antibiotics, geneticin G-418). Subsequently, the culture was transferred into a

96-well plate, with 200 µl per well and the plate was additionally sealed using Parafilm. The plate was incubated at 26 °C in the dark. After one week, dense cultures became visible and wells containing viable cells were transferred into 10 ml ventilated tissue flasks. Genomic DNA integration was tested, by diagnostic PCR, after genomic DNA extraction using phenol/ chloroform extraction. Primer pairs for diagnostic PCR were provided by the manufacturer (LEXSinduce Expression Kit, cat. no. EGE-245). Forward primer for the 5' odc- utr1 control region was 5'-TCCGCCATTCATGGCTGGTG-3', reverse primer for the 5' odc- utr1 control region was 5'-TATTCGTTGTCAGATGGCGCAC-3'. Forward primer for the antibiotic- 3' odc control region was 5'- GGATCCAATATGGGATCGGCCATTG -3' and the reverse primer for the antibiotic- 3' odc control region was 5'-GTGCACCCATAGTAGAGGTGC-3'. This resulted in 1.1 kbp and 2.4 kbp fragments, respectively. After validation of genomic integration, larger volumes (50-600 ml) were cultured in Erlenmeyer flasks at 26 °C in the dark, under aerated conditions, and under agitation at 130 rpm. The T7 promoter-driven transcription was induced by the addition of tetracycline at a final concentration of 15 µg/ml. After 48 h, cells were harvested with centrifugation at 3000 ×g, RT for 10 min.

3.7.4 Analysis of protein expression

Western blotting was performed to analyze whether the expressed huPrP is located intracellularly or extracellularly. For intracellular expression analysis, a 2 ml culture with an optical density of 1.0 was centrifuged at 3000 ×g, RT for 10 min. Pelleted cells were resuspended in 0.2 ml reducing SDS-PAGE sample buffer. For secretory protein expression analysis, 8 ml culture was centrifuged at 3000 ×g, RT for 10 min. The supernatant was mixed with 2 ml of 50% trichloroacetic acid (TCA) and incubated on ice for 30 min. Then, the supernatant was centrifuged at 15000 ×g, 4 °C for 15 min. The pellet was washed with 80% acetone and centrifuged again at 15000 ×g, 4 °C for 15 min. 80 µl of reducing SDS-PAGE sample buffer was added to the pellet. Cell and supernatant samples were incubated at 95 °C for 10 minutes before SDS-PAGE was performed.

3.7.5 SDS-PAGE and western blot analysis

Analysis of samples was conducted using a 12% Tris/Glycine SDS-PAGE at 120 V and subsequently transferred onto a PVDF membrane (PALL Life Sciences) *via* a semi-dry transfer unit (TE70X, Hoefer). After blotting, the membrane was blocked for 1 h with 5% milk powder in TBS-T, washed once with TBS-T, and incubated with anti-PrP antibody (SAF32, 0.1 µg/ml) in TBS-T overnight at 4 °C. The membrane was then washed three times with TBS-T before secondary antibody goat anti-mouse HRP conjugate (Jackson, Immuno Research Inc., 0.1 µg/ml)

was added and incubated for 1 h at RT. After three washing steps, the protein detection was performed using a SuperSignal West Pico Chemiluminescent Substrate Kit (Thermo Fisher Scientific). Visualization was conducted on a LAS 4000 (Fuji Film). For dot blot, a concentration series was applied on a dry nitrocellulose membrane. The starting concentration was 0.85 µg in 2 µl in 50 mM Tris-HCl, 150 mM NaCl, 0.02% DDM, pH 7.4, and was further diluted 1:2 in the same buffer. After that, the membrane was blocked with 5% milk powder in TBS-T and the following steps were identical to the western blot.

3.7.6 Cell lysis and membrane isolation

After centrifuging 600 ml culture with an optical density of 1.73, at 3000 ×g, RT for 10 min, the pellet was resuspended in 10 ml lysis buffer (0.33 M sucrose, 0.15 M Tris-HCl, 0.1 M aminocaproic acid, 1 mM EDTA, pH 7.4). Afterward, glass beads were added into a 15 ml falcon tube, and cells were lysed using a cell disrupter (FastPrep 24; MP Biomedicals) for 3 times 20 sec at 4 M/s. Subsequently, differential centrifugation was conducted to isolate the membrane fraction. First, the cells were centrifuged at 3000 ×g, 4 °C for 5 min, to remove big cell compartments and glass beads. Then, the supernatant was centrifuged at 5000 ×g, 4 °C for 10 minutes, followed by an ultracentrifugation step of the supernatant at 100,000 ×g, 4 °C for 1 h. The pellet contained the membrane fraction which was used for the solubilization of the huPrP.

3.7.7 Solubilization of membrane-bound huPrP

The pellet containing the membrane fraction was suspended in 6 ml buffer (50 mM Tris-HCl, 150 mM NaCl, 1 % DDM, pH 7.4). The sample was incubated for 3 h at 4 °C before they were centrifuged at 100000 ×g, 4 °C for 1 h.

The following detergents were also tested:

Denaturing detergents: 6 M Gdn-HCl, 6 M Urea, 1 % SDS,

Non-denaturing, non-ionic detergents: 1 % Triton X-100, Tween-20, Igepal,

Non-denaturing, zwitterionic detergents: 1 % CHAPS, 1 % Zwittergent 3-14,

Non-denaturing, anionic detergents: 1 % Sodium cholate.

Solubilization results can be seen in Figure 3.5. These samples were incubated for 1 h at 4 °C before they were centrifuged at 100000 ×g, 4 °C for 1 h. Finally, the supernatant (containing the solubilized huPrP) was separated from the pellet (containing the non-solubilized huPrP) and both fractions were analyzed by western blot.

3.7.8 GPI- anchoring analysis

For analysis of the GPI-anchoring, 20 µl of supernatant after the 5000 ×g centrifugation step was incubated with 40 µl 0.1 M HEPES- NaOH buffer, pH 7.6, 20 µl of 0.8 % sodium deoxycholate and 20 µl of 1 nM PI-PLC (cat. no. P6466) in 0.1 % BSA for 1 h, 300 rpm at RT. Afterwards, samples were centrifuged at 5000 ×g for 10 min at RT. Phosphatidylinositol-specific phospholipase C enzyme (PI-PLC) (from Bacillus cereus) is supposed to specifically cleave phosphatidylinositol into two molecules, resulting in the cleavage of GPI-anchored proteins. Pellets and supernatants were afterward analyzed by western blotting.

3.7.9 Purification

After solubilization with 1% DDM, the supernatant was separated by immobilized metal affinity chromatography (IMAC) using a 5 ml Protino Ni-NTA column (Macherey-Nagel) after equilibration of the column with 50 mM Tris-HCl, 150 mM NaCl, 0.1% DDM, pH 7.4. The protein was eluted with a linear gradient from 0 mM to 500 mM imidazole, 50 mM Tris-HCl, 150 mM NaCl, 0.1% DDM, pH 7.4, within 100 ml. The fractions containing native-like huPrP were pooled and subsequently concentrated using a centrifugal concentrator (Vivaspin 2, Sartorius) with a 10 kDa cut-off at 2000 ×g, 4 °C for 10 minutes. After reaching a total volume of 400 µl, size exclusion chromatography (SEC) was used for further purification. The concentrated fractions were loaded on a Superdex 200 Increase 10/ 300 GL column and separated using 50 mM Tris-HCl, 150 mM NaCl, 0.02% DDM, pH 7.4. After each step, analytical samples were collected for analysis by SDS-PAGE. Samples for SV experiments, CD measurements, and dot blot were taken directly after the SEC from the second peak with elution volume from 14.5 ml to 16 ml. Concentration was determined using UV/-Vis spectroscopy and a theoretical extinction coefficient of 57995 M^{-1} cm^{-1} at 280 nm. Recombinant huPrP (23-230) from *E. coli*, was expressed and purified as previously described [212].

3.7.10 Circular Dichroism (CD) Spectroscopy

Spectra of 10 µM huPrP from *L. tarentolae* and *E. coli* were recorded in a Jasco J-815 (Jasco) spectropolarimeter. 100 µl sample of the SEC fraction including the native-like huPrP (in 50 mM Tris-HCl, 150 mM NaCl, 0.02% DDM, pH 7.4) and full-length huPrP from *E. coli* (in 10 mM Tris-HCl, pH 7.4) were filled into a 1 mm quartz glass cuvette and measured ten times at 20 °C, 50 nm/min scanning speed, with 2 nm bandwidth and 4 s digital integration time.

3.7.11 Analytical ultracentrifugation (AUC)

Sedimentation velocity experiments were performed in an analytical ultracentrifuge Proteome Lab XL-A (Beckman-Coulter, Brea, US). Samples of 10 µM huPrP from *L. tarentolae* and *E. coli* (in 50 mM Tris-HCl, 150 mM NaCl, 0.02% DDM, pH 7.4) were measured in standard double sector cells (Aluminium) with an optical path length of 12 mm using an An-60Ti rotor. The duration of temperature equilibration to 20 °C was 1 h. Data was recorded at 50,000 rpm for 5.5 h. Data analysis was performed using a continuous distribution Lamm equation model, c(s), implemented in the software Sedfit (version 16p35)[213]. Graphical output was created using the software Datagraph[250].

3.8. Supporting information

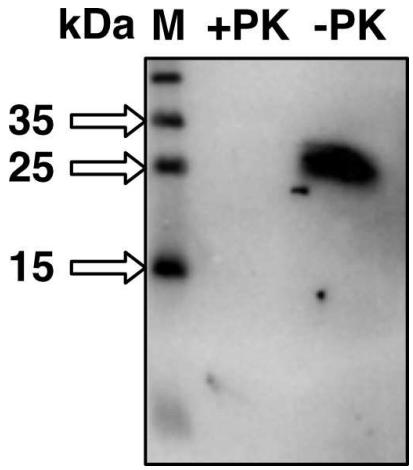

Figure 3.4: Proteinase K resistance of full-length huPrP from *L. tarentolae*. Proteinase K (PK) digestion of native-like huPrP results in complete digestion. 50 µl samples after 5000 ×g cell disruption centrifugation step were incubated with 50 ng/µl proteinase K for 1 h at 37°C and 300 rpm shaking. Samples were subsequently analyzed by western blotting.

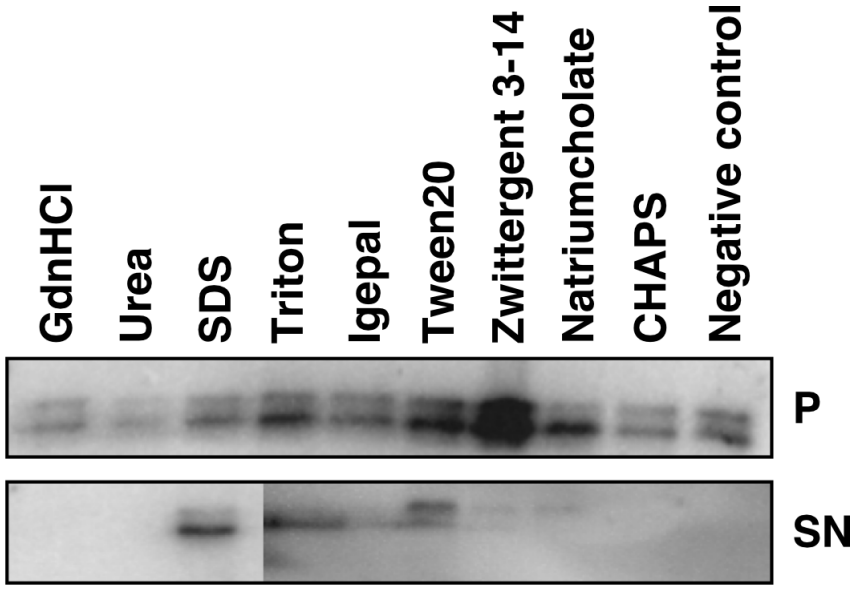

Figure 3.5: Solubilization of huPrP by different detergents. Solubility of native-like huPrP using different detergents. Samples were incubated for 1 h at 4°C. 6 M GdnHCl and Urea and 1% of remaining detergents were used for solubilization. P represents the pellet and SN represents the supernatant after centrifugation for 1 h, 4°C at 100.000×g. Samples were analyzed by western blot. Molecular masses were between 25 kDa and 35 kDa.

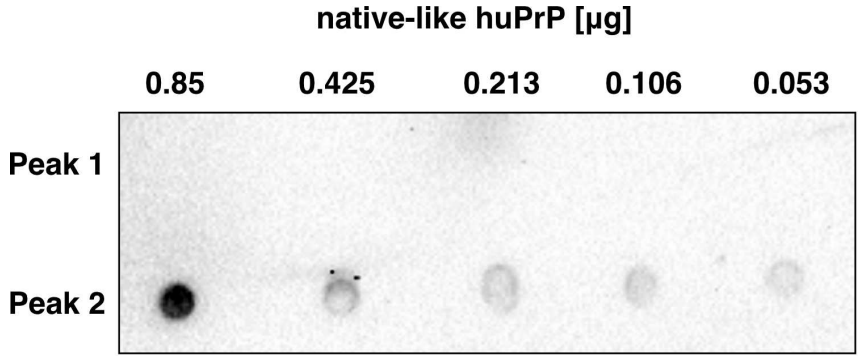

Figure 3.6: Immunological detection of huPrP from *L. tarentolae* after purification. Dot blot of native-like huPrP after SEC. The fractions eluting between 8 ml and 10 ml (Peak 1) as well as 14.5 ml and 16 ml (Peak 2) were concentrated like it was described for IMAC samples before SEC. A concentration series was applied, starting from 0.85 µg in 2 µl and further diluted 1:2 in buffer (50 mM Tris, 150 mM NaCl, 0.02% DDM, pH 7.4). The second row shows the second elution peak (Peak 2), verifying the identity of native-like huPrP, while the first row represents the first elution peak showing no signal for native-like huPrP.

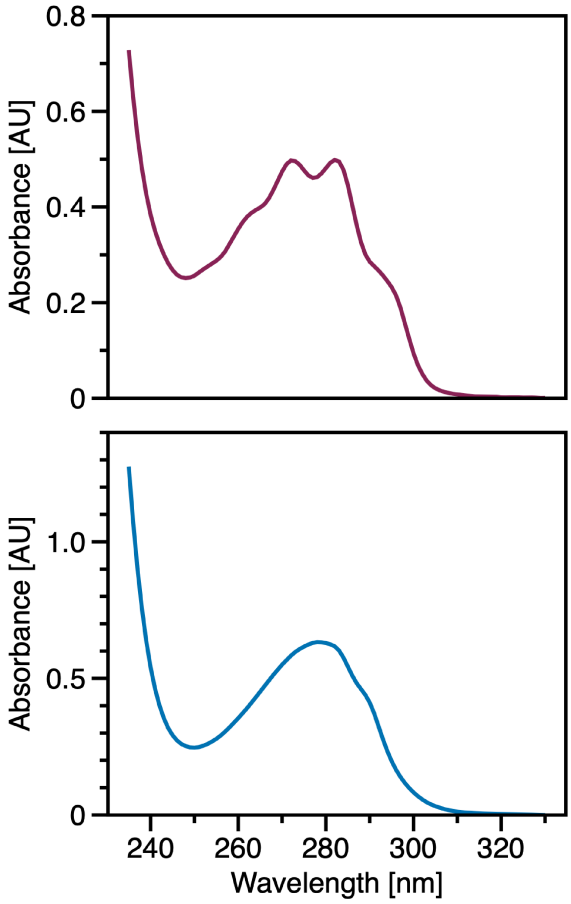

Figure 3.7: Characteristic absorbance spectrum of huPrP from *L. tarentolae* and *E. coli*. UV/-Vis spectroscopy shows distinct absorbance spectra for native-like huPrP expressed in *L. tarentolae* compared to full-length huPrP expressed in *E. coli*. 100 µl samples from the second elution peak of SEC containing the native-like huPrP in 50 mM Tris-HCl, 150 mM NaCl, 0.02 % DDM, pH 7.4 from *L. tarentolae* (purple) and purified full-length huPrP in 10 mM Tris-HCl, pH 7.4 from *E. coli* (blue) were used for absorbance measurement in a quartz glass cuvette.

4

All-D-Enantiomeric Peptide D3 Designed for Alzheimer's Disease Treatment Dynamically Interacts with Membrane-Bound Amyloid-β Precursors

4.1. Article information

Title of manuscript: All-D-Enantiomeric Peptide D3 Designed for Alzheimer's Disease Treatment Dynamically Interacts with Membrane-Bound Amyloid-β Precursors

Authors: Eduard V. Bocharov[1,2,‡,*], Lothar Gremer[1,3,4,6,‡], Anatoly S. Urban,[1,2,‡], Ivan S. Okhrimenko[1,‡], Pavel E. Volynsky[1,2,‡], Kirill D. Nadezhdin[1,2], Olga V. Bocharova[1,2], Daniil A. Kornilov[1], Yuliya A. Zagryadskaya[1], Anna V. Kamynina[1,2], Pavel K. Kuzmichev[1], Janine Kutzsche[3,4,6], Najoua Bolakhrif[3,4,6], Andreas Müller-Schiffmann[7], Norbert A. Dencher[1,8], Alexander S. Arseniev[1,2], Roman G. Efremov[1,2,9], Valentin I. Gordeliy[1,3,4,5,*], and Dieter Willbold[1,3,4,6*]

Journal: Journal of Medicinal Chemistry

Status: Published (November 2021)

[1] Research Center for Molecular Mechanisms of Aging and Age-related Diseases, Moscow Institute of Physics and Technology (State University), 141701 Dolgoprudny, Russia

[2] Department of Structural Biology, Shemyakin-Ovchinnikov Institute of Bioorganic Chemistry RAS, 117997 Moscow, Russia;

[3] Institute of Biological Information Processing (IBI-7: Structural Biochemistry), Forschungszentrum Jülich, 52425 Jülich, Germany
[4] JuStruct: Jülich Center for Structural Biology, Forschungszentrum Jülich GmbH, 52425 Jülich, Germany
[5] IRIG, Institut de Biologie Structurale (IBS), Université Grenoble Alpes, CEA, CNRS, 38000 Grenoble, France
[6] Institut für Physikalische Biologie, Heinrich-Heine-Universitaet Düsseldorf, 40225 Düsseldorf, Germany
[7] Department of Neuropathology, Heinrich-Heine-Universitaet Düsseldorf, 40225 Düsseldorf, Germany
[8] Physical Biochemistry, Chemistry department, Technical University of Darmstadt, 64287 Darmstadt, Germany
[9] School of Applied Mathematics, Higher School of Economics, 109028 Moscow, Russia
* edvbon@mail.ru, valentin.gordeliy@ibs.fr, dieter.willbold@uni-duesseldorf. de
‡ Authors contributed equally

4.2. Declaration of article contributions

4.2.1 Experimental and Data analyses

MDS and FP analyses were performed in cooperation with E.V.B., L.G., I.S.O., A.S.U., Y.A.Z., and me.

4.2.2 Manuscript preparation

E.V.B. prepared the manuscript with input from all other authors

4.3. Abstract

Alzheimer's disease (AD) is a severe neurodegenerative pathology with no effective treatment known. Toxic amyloid-β peptide (Aβ) oligomers play a crucial role in AD pathogenesis. All-d-Enantiomeric peptide D3 and its derivatives were developed to disassemble and destroy cytotoxic Aβ aggregates. One of the D3-like compounds is approaching phase II clinical trials; however, high-resolution details of its disease-preventing or pharmacological actions are not completely clear. We demonstrate that peptide D3 stabilizing Aβ monomer dynamically interacts with the extracellular juxtamembrane region of a membrane-bound fragment of an amyloid precursor protein containing the Aβ sequence. MD simulations based on NMR measurement results

suggest that D3 targets the amyloidogenic region, not compromising its α-helicity and preventing intermolecular hydrogen bonding, thus creating prerequisites for inhibition of early steps of Aβ conversion into β-conformation and its toxic oligomerization. An enhanced understanding of the D3 action molecular mechanism facilitates development of effective AD treatment and prevention strategies.

4.4. Introduction

Today more than 50 million people worldwide suffer from AD and dementia associated with it, and this number is expected to be tripled by 2050 [251]. Despite the enormous progress in science and medicine, the causes of AD and the mechanisms associated with its pathology remain largely unknown over 110 years after the disease was first described as a form of a progressive neurodegenerative and behavioral disorder by Alois Alzheimer in Germany [111, 252, 253]. Genetic evidence strongly suggests that aberrant generation or clearance of the neurotoxic Aβpeptide triggers the disease [252]. Normal biological function of this amyloid peptide is largely unknown. Nevertheless, Aβ isoforms of different lengths are found in humans regardless of the age or the disease; the peptides in the monomeric form can play a role in signaling pathways in the brain and are likely to have neuroprotective properties at low concentrations [254, 255, 256, 257, 258]. Aβ and related P3 peptides are the products of sequential extramembrane and intramembrane cleavage of the single-span membrane APP by α-, β-, and γ-secretases [252, 259]. In the first step of Aβ maturation, APP is cleaved by membrane-bound β-secretase, aspartyl protease BACE (β-site APP-cleaving enzyme), which removes the APP ectodomain and leaves a 99 amino acid C-terminal fragment (CTFβ) in the membrane. This APP CTFβ or C99 termed fragment is cleaved in the next step by a large membrane protein complex termed γ-secretase [260]. This intramembranecleaving aspartyl protease complex processes C99 in the transmembrane (TM) domain at the ε-site, thereby releasing the APP intracellular domain (AICD) from the membrane into the cytosol. In a stepwise process, a variety of Aβ isoforms are generated by additional γ-secretase cleavages at the ζ- and γ-sites that trim the TM domain until it is short enough to release predominantly 38-42 residue-long Aβ isoforms from the membrane into the extracellular space or into the lumen of secretory pathway organelles. Aβ40 is generated as a major product along minor amounts of the shorter Aβ38 and the longer Aβ42, which is more hydrophobic and fibrillogenic. Aβ also aggregates into oligomers, which are considered to be the most toxic Aβ isoform and an attractive target for drug development against AD.

Generation of Aβ is prevented by alternatively occurring extramembrane cleavage of APP by membrane-bound α-secretase, a metalloprotease of the ADAM (a disintegrin and metalloprotease)

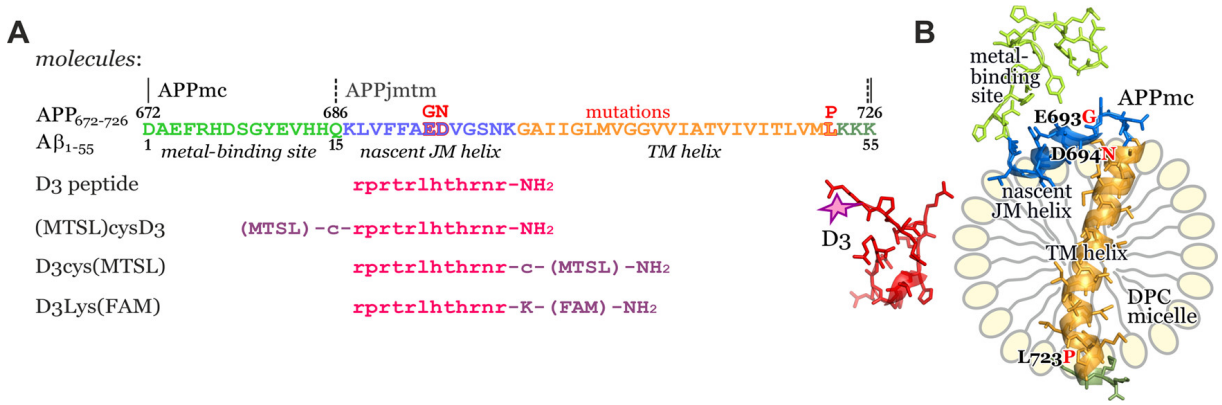

Figure 4.1: Sequences (A) and schematic presentation (B) of APP TM fragments and D3 derivatives studied in the micellar environment.

family, which removes the N-terminal metalbinding region of Aβ and generates the shorter APP CTF_{α}, C83. More than half of mutations associated with AD familial forms were found in the TM domain and juxtamembrane (JM) regions of APP [261]. The pathogenic mutations presumably affect the structural-dynamic properties of APP and its cleavage fragments, e.g., changing the conformational stability, lateral dimerization, and intermolecular interactions, including recognition by the secretases [262, 263, 264, 265, 266, 267].

In recent years, different substances have been developed targeting Aβ production and clearance, including peptidebased drugs [268, 269, 270, 271, 272, 273, 274]. However, their practical applications yielded only limited success, and they rather affect AD symptoms than directly eliminate the toxic Aβ oligomers underlying the development and progression of the disease. Arginine-rich D3- like peptides belong to a relatively new class of compounds, the all-D-enantiomeric peptides, which exhibit two major advantages compared to their L-enantiomeric stereoisomers. They show exceptional proteolytic stability [275, 276, 277] and a lower, if at all, immunogenic potential [278]. D3 was selected via mirror-image phage display against monomeric Aβ42 out of a peptide library encoding more than a billion different random 12-mer sequences [279]. D3 thus consists of 12 amino acid residues, each of them being in the D-enantiomeric configuration (sequence: rprtrlhthrnr). *In vitro*, D3 specifically eliminated cytotoxic Aβ oligomers by converting them into nontoxic, nonamyloidogenic, and nonfibrillar assemblies [280]. *In vivo*, D3 proved therapeutically effective in three different transgenic AD mouse models [279, 280, 281]. In particular, it reduced the amyloid plaque load and cerebral inflammation upon direct application into the brain of tg APPswe/PS1ΔE9 mice and inhibited the deterioration of the motor neuronal degenerative phenotype in HOM TBA2.1 after

intraperitoneal treatment and improved cognition after oral treatment of tg APPswe/PS1ΔE9 [281]. A pharmacokinetic study revealed terminal plasma half-lives of D3 between 32 and 41 h, a very high oral bioavailability of 58.3 % and a brain/plasma ratio of 0.9 four hours after application, which implicates that D3 enters the brain very efficiently [282]. Currently, one of the D3 derivatives, which already demonstrated its safety and tolerability in healthy volunteers [283], is about to undergo phase II clinical trial (ClinicalTrials.gov Identifier: NCT04711486). However, in the absence of high-resolution structural data, the mechanism of their possible interaction with APP and its fragments (Aβprecursors spanning the lipid bilayer) remained unknown. It hampers further optimization of D3-like compounds for the treatment of Alzheimer's disease by stabilizing Aβ monomers in their native conformation, thereby disassembling already existing Aβ oligomers into nontoxic native Aβ monomer building blocks.

Here, we present structural and biochemical evidence showing that D3 being an intrinsically disordered peptide (IDP) [284, 285] can dynamically and specifically bind to extracellular JM regions of a membrane-bound Aβ precursor, CTFβ transmembrane fragment APP $_{672\text{-}726}$ ($A\beta_{1\text{-}55}$ in amyloid-β numeration). The MD simulations based on experimental data suggest that D3 recognizes the amyloidogenic region of APP also before its processing, restricting conformational diversity not compromising its α-helicity and preventing intermolecular hydrogen bond formation, which would create prerequisites for inhibition of early steps of Aβ conversion into β-conformation and its toxic oligomerization associated with early stages of AD development.

4.5. Results

4.5.1 D3 Interacts Specifically with a Membrane-Bound Aβ Precursor, the TM Fragment APP $_{672\text{-}726}$.

To understand whether D3-like peptides interact with APP, we performed comprehensive experimental studies with the aid of nuclear magnetic resonance (NMR) spectroscopy supported by microscale thermophoresis (MST), microfluidic diffusional sizing (MDS), fluorescence polarization (FP), circular dichroism (CD) spectroscopy, and molecular dynamics (MD) simulations. The fluorescent- and spin-labeled analogues of D3 as well as membrane-bound Aβprecursor $APP_{672\text{-}726}$ (known as APPmc) and its AD familial mutant variants listed in Figure 4.1A were used.

The APPmc peptide corresponding to $A\beta_{1\text{-}55}$ includes an intact helical APP TM domain ($A\beta_{27\text{-}55}$) with the adjacent N-terminal JM region containing a soluble metal-binding domain ($A\beta_{1\text{-}16}$) followed by a surface-associated region having a transient helical structure, which is capable

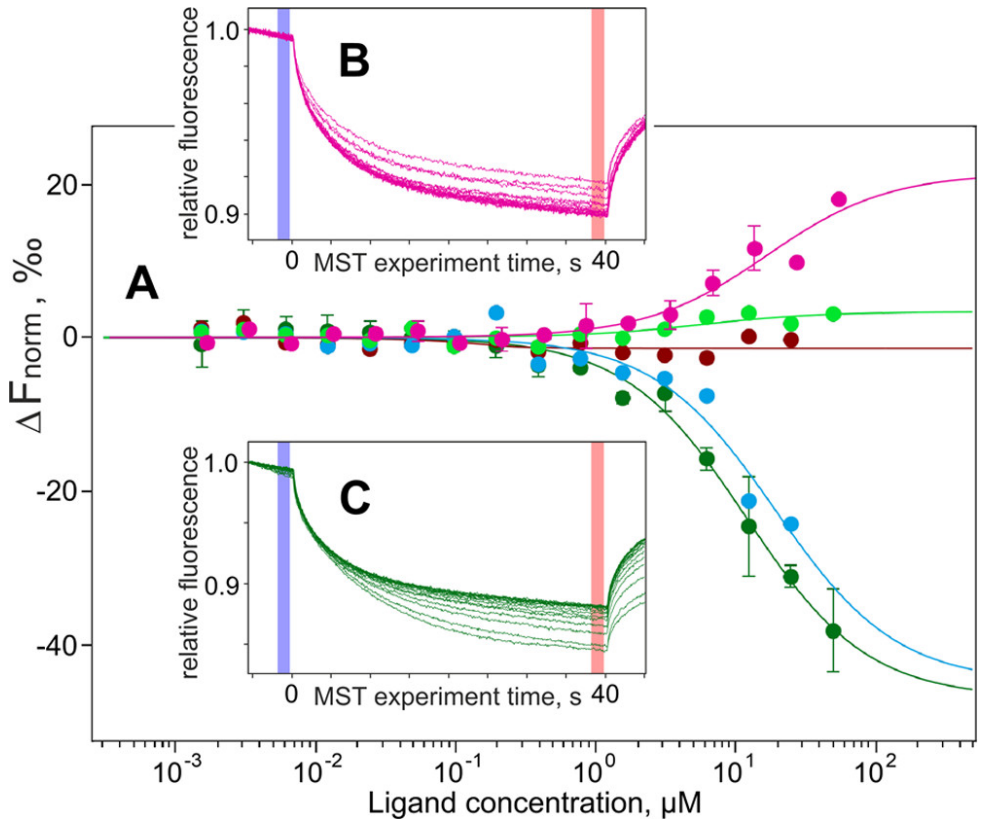

Figure 4.2: MST measurements of the interaction of D3 with APP TM fragments in the micellar environment. (A) Sigmoidal approximation plots of the D3Lys(FAM) fluorescence changes due to thermophoresis in the presence of membrane-bound APPmc (dark green line, estimated K_d = 10.6 ± 1.7 μM) and its double mutant variant with E693G and D694N amino acid substitutions (blue line, estimated K_d = 21.6 ± 1.0 μM). The control experiments did not reveal measurable interactions of D3Lys(FAM) with empty DPC micelles (salad green line) and of the FAM-label with membrane-bound APPmc (brown line). D3Lys(FAM) showed an interaction with membrane-bound EphA2tm (pink line, estimated K_d = 21.4 ± 3.9 μM) with opposite influence on the change of fluorescence during thermophoresis when compared with the APP TM fragments. (B) and (C) Thermophoresis curves (inner boxes) of binding of fluorescently labeled D3Lys(FAM) to EphA2tm and APPmc embedded into DPC micelles, respectively. Each curve corresponds to the TM fragment concentrations varying from 1.5 nM to 50 μM. The mean values of fluorescence in blue (as reference) and red (after thermophoresis) areas were used for the calculation of the normalized fluorescent unit, ΔF_{norm}.

of transforming to β-strand involved in folding the β-amyloid [286, 287, 288, 289]. Besides the wild-type APPmc, the fragment with the "Australian" familial mutation (L723P-APPmc) located in the C-terminus of the APP TM domain and rendering certain amyloidogenic properties to the fragment, gradually evolving from the typical α-helical structure to a β-sheet conformation [267], was also investigated.

Unlabeled and $^{13}C/^{15}N$ isotope-labeled APPmc and L723-PAPPmc peptides were obtained using a cell-free expression system [290, 291] and solubilized in membrane-mimicking complexes, zwitterionic dodecylphosphocholine (DPC) micelles (Figure 4.1B), under monomeric conditions at a peptide/lipid ratio of 1/200.

Using MST measurements, we found that C-terminally fluorescent-labeled D3 (D3Lys(FAM)) directly interacts with membrane-bound APPmc with a dissociation constant K_d equal to 10.6 ± 1.7 μM (Figure 4.2), which is noticeably higher compared to that observed for binding of D3 to Aβdissolved in bulk solution [292]. MST measurements with membrane-bound L723P-APPmc were unsuccessful, presumably due to its precipitation into amorphous aggregates [267]. Alternative measurements of D3 affinity toward DPC-micelle-bound APPmc by MDS and FP revealed the upper limit of dissociation constant K_d of not more than ∼40 μM (Figure 4.10C and D).

To evaluate the diversity of possible intermolecular interactions of D3-like peptides with a membrane-bound Aβprecursor by heteronuclear NMR, we used spin-labeled analogues of D3 with an MTSL nitroxyl radical spin-label covalently attached *via* an additional D-cysteine residue to the N- or C-terminus of the peptide, named (MTSL)cysD3 or D3cys(MTSL), respectively.

To obtain the baseline NMR spectra for comparison, in the control experiments, the intensity of the nitroxide spin-label was quenched by ascorbic acid. The heteronuclear $^{1}H/^{15}N$ HSQC and $^{1}H/^{13}C$ CT-HSQC spectra (Figure 4.3A, Figure4.9, Figure4.10A) illustrate inhomogeneous broadening of NMR signals of amide and methyl groups of APPmc caused by interactions with the unquenched nitroxide spin-label of D3 (the signals with quenched and unquenched labels are overlaid) due to paramagnetic relaxation enhancement (PRE).

The distributions of signal broadening for the backbone amide groups caused by the proximity of the N- or C-terminal nitroxyl radical of (MTSL)cysD3 or D3cys(MTSL) along the amino acid sequence of APPmc are shown in the form of bar charts in panels (A) and (B) of Figure 4.4, respectively. It should be noted that the difference in the side chain sizes between residues is unlikely to distort the spatial pattern of the proximity of the spin-labeled group to the backbone amide groups since, as according to [293], signal broadening beyond the resolution occurs at the distances of up to 1.4 nm (assuming permanent proximity of the label). The dissociation constant K_d was evaluated based on NMR titration [294] using Ala701 methyl group signal, which is especially sensitive to the presence of D3 (Figure 4.3, 4.9, and 4.10A), and assuming one-to-one binding, and an upper limit of $\sim$ 30 μM was obtained (Figure 4.10B), which is generally consistent with the affinity measurements by MST, MDS, and FP.

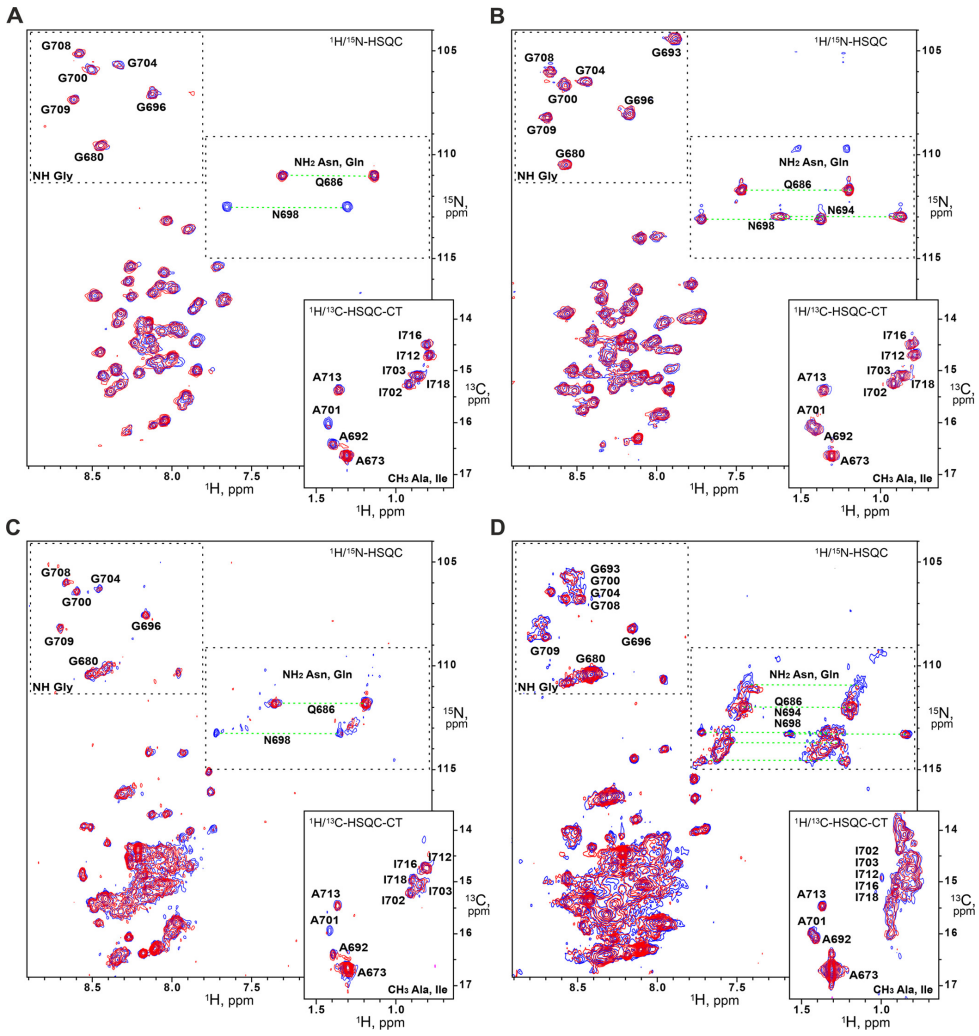

Figure 4.3: D3 binding to the APP TM fragments monitored by PRE-NMR signal broadening. (A-D) Overlaid NMR spectra, ^{1}H/^{15}N HSQC and ^{1}H/^{13}C HSQC-CT (a fragment in the right corner), of wild-type and mutant APP TM fragments: APPmc (A), E693G/D694N-APPmc (B), L723P-APPmc (C), and E693G/D694N/L723P-APPmc (D), embedded into DPC micelles in the presence of D3cys(MTSL) (red spectra) with a D3/APP fragment ratio of 2:1 and after addition of ascorbic acid (blue spectra), when the nitroxyl spin-label is quenched. Cross-peak assignments of backbone and side-chain amide groups of Gly, Asn, and Gln residues as well as of methyl groups of Ala residues are marked according to the Aβ sequence (see also Figure4.8 and Figure4.9)

Clearly, the NMR signals from the residues in the nascent JM helix and N-terminus of the TM helix of APPmc are strongly affected by the proximity of the MTSL group of N- or C-spin-labeled D3 (i.e., (MTSL)cysD3 or D3cys(MTSL)), while the PRE-NMR signal broadening is less pronounced for the residues from the N-terminal part of the metal-binding domain and C-terminus of the TM domain. In addition, marginal PRE-NMR signal broadening is also observed near the C-terminus of the APP TM helix, which seems to indicate some binding of D3

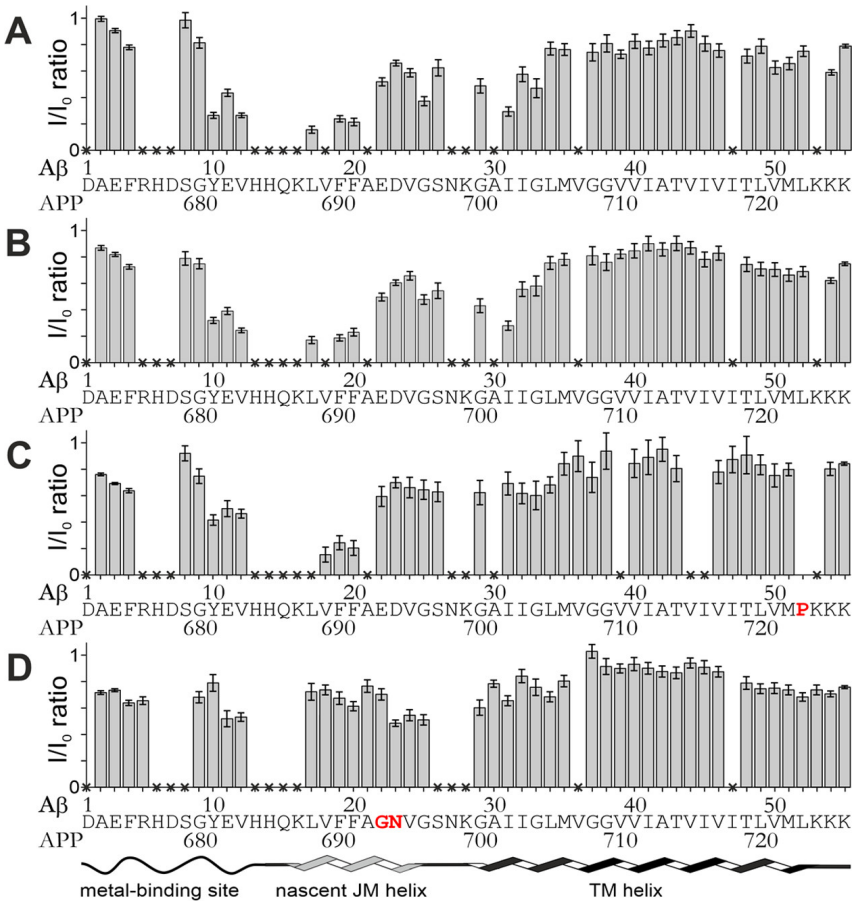

Figure 4.4: PRE-NMR signal broadening patterns for amide groups of wild-type and mutant APP TM fragments after addition of (MTSL)cysD3 to APPmc. (A) or D3cys(MTSL) to APPmc (B), L723P-APPmc (C), and E693G/D694N-APPmc (D) with a D3/APP fragment ratio of 2:1. The data points corresponding to unassigned cross-peak positions or strongly overlapping cross peaks of the amide groups are marked by diagonal crosses.

to the C-terminal sequence exposed from the micelle or unspecific interaction with the micelle surface. Overall, the similarity of the pattern of the PRE-NMR signal broadening in the case of addition of N- or C-spin-labeled D3 implies that both peptides bind with certain specificity to the extracellular JM regions of the membrane-bound Aβprecursor, although the interaction is weak and dynamic, with the spinlabels transiently approaching different APPmc residues along the JM sequence.

Although the membrane-bound mutant L723P-APPmc proved unstable [267], NMR experiments revealed that PRE-NMR signal broadening of the monomeric form of the mutant fragment in the presence of spin-labeled D3 is almost identical to the wild-type case (Figures 4.3C and 4.4C), implying that D3 binds to the mutant fragment in a similar manner. Notably, the NMR signals

from the observed amyloid-like oligomeric state (less than ∼100 kDa) [267] of L723P-APPmc are also affected by addition of spin-labeled D3, which is consistent with the experimental observation of large nonfibrillar nontoxic Aβ aggregates formed by coprecipitation with D3 [281, 292].

4.5.2 Molecular Dynamics Simulations of the D3/APPmc Complex in Hydrated Explicit Lipid Bilayers Are Indicative of Transient Protein-Protein Interactions in an IDP/IDP Manner

To evaluate the ability of D3 to interact with a membrane-bound Aβprecursor, a series of MD simulations started with PRE-NMR-derived distance constraints were performed for different APP TM fragments embedded into the explicit POPC bilayer (see Methods). Besides the wild-type $APP_{672\text{-}726}$ (APPmc, $A\beta_{1\text{-}55}$) and its mutant form L723P-APPmc, the truncated forms $APP_{686\text{-}726}$ (APPjmtm and L723P-APPjmtm) without the metal-binding domain were investigated. First, to investigate conformational preferences of free D3, 1 μs MD simulations in an explicit solvent with a random coil starting configuration were performed (Figure 4.11). The simulation revealed substantial conformational variability; the occurring conformations were binned into 29 distinct clusters (four clusters with population >5 %, Table S2), in most of which the peptide was in a random coil state. However, one folded helical turn was present in some of the substantially populated clusters, and the cluster with two folded helical turns was the most highly populated one in the ensemble (about 39 % of the entire MD trace). Noteworthily, the helical conformations proved rather stable, especially on the C- terminal side (without the helix-destabilizing proline residue), i.e., once formed, the nascent helix of D3 persisted for tens of nanoseconds. This implies that the short positively charged D3 has a flexible IDP-like conformation (consistently with the results reported earlier) [292] capable of forming transient helical structures. The existence of relatively stable diverse conformations implies that moderate alteration of the environment should be able to induce redistribution between them. Indeed, while CD spectra (Figure 4.10 and Table 4.2) of the peptide in pure aqueous solution were indicative of random coil as an average state, addition of an organic solvent (50 % trifluoroethanol or 25 % hexafluoroisopropanol, HFIP) caused it to switch to helical conformation. Likewise, the peptide remains in the random coil state in a suspension of membranemimicking DPC micelles, but addition of negatively charged sodium dodecyl sulfate (SDS) in the concentration corresponding to the presence of three SDS molecules per DPC micelle (consisting approximately of 60 DPC molecules) also switched the positively charged D3 into partially folded conformation, presumably due to adsorption on the micelle surface. In light of the observed D3 conformational lability, two conformational states corresponding to the most highly populated clusters (39 and 15 %) obtained via MD simulations

in water were used as D3 starting configurations for the investigation of interactions with the APP TM fragments. Besides being the most highly represented in the conformational ensemble, these two conformations (Figure 4.11) turned out to be antithetic: the initial conformation for the first simulation was partially helical (nascent helix), and the second simulation started with the peptide in a random coil (mostly extended, hairpinlike) conformation. In both cases, D3 was initially bound to the JM region of the wild-type and mutant APP TM fragments as deduced from our NMR data and then relaxed during 20 ns with the geometric constraints corresponding to the putative binding site suggested by the strong PRE-NMR signal broadening (Figures 4.3A,C and 4.4A,C) for for A^{701} side-chain methyl group, N^{698} side chain, L^{688}, V^{689} (partially overlapped for wild-type fragments but with distinct signal broadening for L723P-APPmc), and F^{691} backbone amide groups (see Experimental Section) with subsequent 200 ns unconstrained MD simulations. Since PRE-NMR signal broadening patterns were nearly identical for the C- and N-terminal spin-labeled D3 derivatives, four MD simulations were carried out starting with constraints imposed on the C-terminus (to verify reproducibility) and one with constraints applied to the N-terminus (as a consistency check). The obtained atomic coordinates and experimental restraints for complexes of D3 with APPmc and L723P-APPmc in the explicit POPC bilayer were deposited in the Protein Data Bank under accession codes PDB ID: 7B3J and 7B3K, respectively.

As illustrated in Figure 4.5 (see also Figures 4.13-4.15), D3, being in different conformations, interacted with both wildtype and mutant membrane-bound APP TM fragments during the entire unconstrained MD runs, with the interaction being dynamic but without dissociation. The sites of APP interaction with D3 as derived from MD traces were clustered around the locations corresponding to satisfying accuracy to the interaction site suggested by the PRE-NMR data (Figure 4.4A-C), namely, the site extended along the nascent JM helix up to the N-terminal part of the TM helix, the region known to be critical for amyloid formation and binding of basic lipophilic amyloid recognition sequence peptides [295, 107, 296]. Additional transient interactions of D3 with the metal-binding domain of APPmc embedded into the explicit lipid bilayer were observed in the resulting MD traces, which is also consistent with the PRE-NMR data in the micellar environment. The 0.4 nm cutoff distance was selected to highlight the closest contacts; however, PRE-NMR signal broadening in the experiments starts to occur at considerably longer distances. Figures 4.16 and 4.17 provide an integrated representation of MD results for a more meaningful comparison with NMR data. The profiles of the proximity of N- and C-termini of D3 to APP JM region residues (Figure 4.16) differ considerably depending on the starting conformation of D3 assumed for simulations, and apparently, the PRE-NMR signal broadening profile reflects contributions of all possible D3 conformations, which was to be expected for flexible IDP/IDP-type interaction [297, 298, 299]. Importantly, for all of the

residues used for the application of initial constraints during the first 20 ns tend to return to within the distances meeting the signal broadening criterion during subsequent 200 ns unconstrained runs with considerable frequency, as is to be expected from the experimental results.

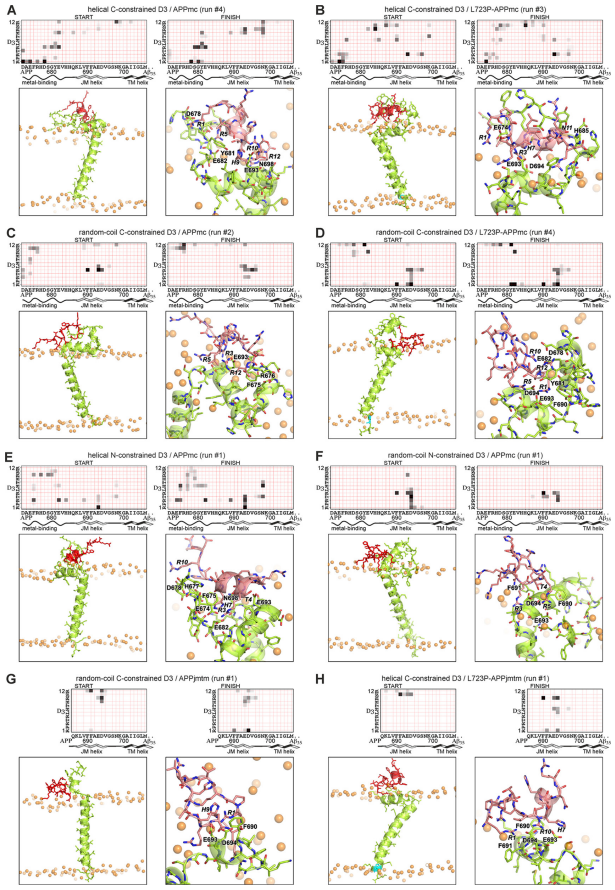

Figure 4.5: IDP/IDP-like interaction of D3 with wild-type and mutant APP TM fragments revealed by MD simulations in the hydrated explicit POPC bilayer. (A-H) Representative D3/APP TM conformational ensemble obtained by the unconstrained 200 ns MD runs performed after the 20 ns constrained MD simulations started with different D3 conformations specified on top (the full set is presented in Figure 4.12). D3-APP contact maps (upon start and after the finish of the unconstrained MD run), resulting overall configurations of the complex, and local structures of IDP/ IDP-like D3 binding to APP JM region are shown with marked residues in close D3-APP contacts. The intermolecular contacts in the maps are color-coded according to the number of direct contacts between heavy atoms with a 0.4 nm distance cutoff from white (no contacts) to black (ten protein-protein contacts). D3, APP TM fragments, and lipid phosphorous atoms are colored in red, green, and orange, respectively. The L723P mutation is highlighted in cyan. The cytoplasmic leaflet of the lipid bilayer is at the bottom.

Such a dynamic interaction with rapid conformational rearrangements and changes of contacting groups of amino acid residues in the opposing subunits of the complex explains why we were unable to directly obtain ^{1}H-^{1}H NOE (nuclear Overhauser effect) contacts between unlabeled

D3 and APPmc despite their relative proximity to each other in the complex. As it is common for IDP/IDP-like interactions, the dynamic nature of the complex formation process is also consistent with the absence of credibly detectable chemical shift changes (Figure 4.8D), which, together with a certain broadening of some cross peaks, implies that conformation exchange rate corresponds to fast or intermediate NMR timescale (hundreds of microseconds or faster).

In the dynamic D3/APPmc complex, formation of numerous transient intermolecular hydrogen bonds as well as salt-bridge, cation-π, and stacking interactions occurred (Figures 4.5A-F, 4.13 and Table 4.3). Particularly, upon peptide recognition, multiple transient interactions were observed between side chains of the positively charged residues of D3 and the negatively charged residues of APP TM fragments distributed along the JM sequence, implying the importance of the electrostatic interactions in complex formation. Notably, MD simulations of the truncated forms of APPjmtm without the metal-binding domain revealed that the side-chain carboxyl groups of residues E^{693} and D^{694} from the nascent APP JM helix participate in formation of intermolecular salt bridges and hydrogen bonds with the positively charged and polar side chains of the D3 residues (Figure 4.5G,H).

To verify this PRE-NMR-based MD data and specify the hotspot of D3/APPmc interaction, we studied D3 interactions with AD familial mutants of APPmc and L723P-APPmc isoforms (E693G/D694N-APPmc and E693G/D694N/L723P-APPmc) with simultaneous 'Arctic' E693G and 'Iowa' D694N amino acid substitutions [300] placed in the C-terminus of the APP JM helix. Indeed, the PRE-NMR experiments revealed a significant decrease of the PRE-NMR signal broadening (Figures 4.3B,D and 4.4D) with residual D3/APPmc interaction near the metal-binding domain of both APP TM fragments. In good agreement with PRE-NMR data, MST measurements also demonstrate that these mutations decrease the strength of D3/APPmc interactions by twofold (to $K_d = 21.6 \pm 1.0$ μM; Figure 4.2), suggesting that local electrostatic contacts play an important but not predominant role in complex formation.

To prove that the D3/APPmc interaction is specific, we performed a control competition experiment with a different TM fragment having similar charges in the JM region. For the control experiment, we obtained a TM fragment of EphA2 receptor tyrosine kinase ($EphA2_{523\text{-}563}$, so-called EphA2tm) [301], which also undergoes γ-secretase-mediated intramembrane proteolysis and has a similar JM region composition (though without a cation-binding domain), specifically including two negatively charged residues within it. MST measurements (Figure 4.2) suggest that D3 interacts with both membrane-bound EphA2 and APP TM fragments, however, with certain important differences. The EphA2tm binding constant is comparable with that of the double E693G/D694N-APPmc mutant but approximately twice higher than that of wild-type APPmc. Besides that, the observed difference in the signs of the fluorescence change upon

complex formation is clearly indicative of different interaction modes. More specifically, the D3/APPmc complex appears to undergo significant temperature-induced conformational changes directly affecting its fluorescence, in addition to the increased effective size of the complex compared to the free ligand. Considerable differences between D3 interactions with EphA2tm and APPmc were further illustrated by NMR measurement results (Figures 4.18 and 4.19). D3/APP interaction yields clearly specific patterns of PRE-NMR signal broadening within the JM region, more pronounced for the wild-type APPmc fragment, whereas in the case of EphA2tm the broadening is almost uniform. In additional NMR experiments performed to evaluate the binding competition between EphA2 and APP TM fragments, tenfold excess of added unlabeled EphA2tm failed to abolish D3-induced PRE-NMR signal broadening of $^{15}N/^{13}C$-labeled APPmc, causing only a minor reduction (by about a third) of the broadening. Thus, D3 is also capable of interacting with proteins sharing certain similarities with APPmc, such as negatively charged JM residues, but specific D3/APPmc complex formation was experimentally observed.

The secondary structure evolution during the unconstrained MD simulations (Figure 4.13) implies a potentially significant behavior pattern of certain peptide moieties capable of structural rearrangements. As can be seen in MD simulations (Figure 4.14 and Table 4.2), the presence of D3 in the vicinity of the APP JM region somewhat stabilized the transient α-helical structure of the latter, except for the case of interaction of initially helical D3 with L723P-APPmc. More specifically, the average helicity of APP JM region 686-696 ($A\beta_{15\text{-}25}$) over the simulations without D3 varied between different starts notably for the wild-type APP TM fragment and greatly for the amyloidogenic L723P mutant form, whereas after addition of D3 this parameter becomes almost invariant, consistently staying above ∼60 %. Addition of D3 in the random coil (hairpinlike) conformation also caused a detectable overall increase of the helicity of APP JM region 686-696. This difference is attributable to a somewhat higher number of intermolecular hydrogen bonds and salt bridges formed between D3 in the random coil conformation and the APP TM fragments.

Nevertheless, the effects of APP interaction with the helical D3 peptide are not limited to the reduction of conformational lability (variability of average helicity). This can be illustrated by the MD simulation, where L723P-APPmc interacted with the initially helical C-constrained D3 (Figures 4.13 and 4.14). In this case, disappearance of the β-sheet structure in the APP JM region (transiently formed about 70 ns after the unconstrained simulation start) and formation of the transient 3_{10} helix in the APP JM region correlated with restoration of D3 helicity.

Besides, MD simulation data revealed adsorption of D3 on the membrane surface *via* interactions with the polar headgroups of lipids with the hydrophobic side chains submerging under the membrane surface (Figures 4.5 and 4.13), suggesting that the lipid bilayer can also participate in

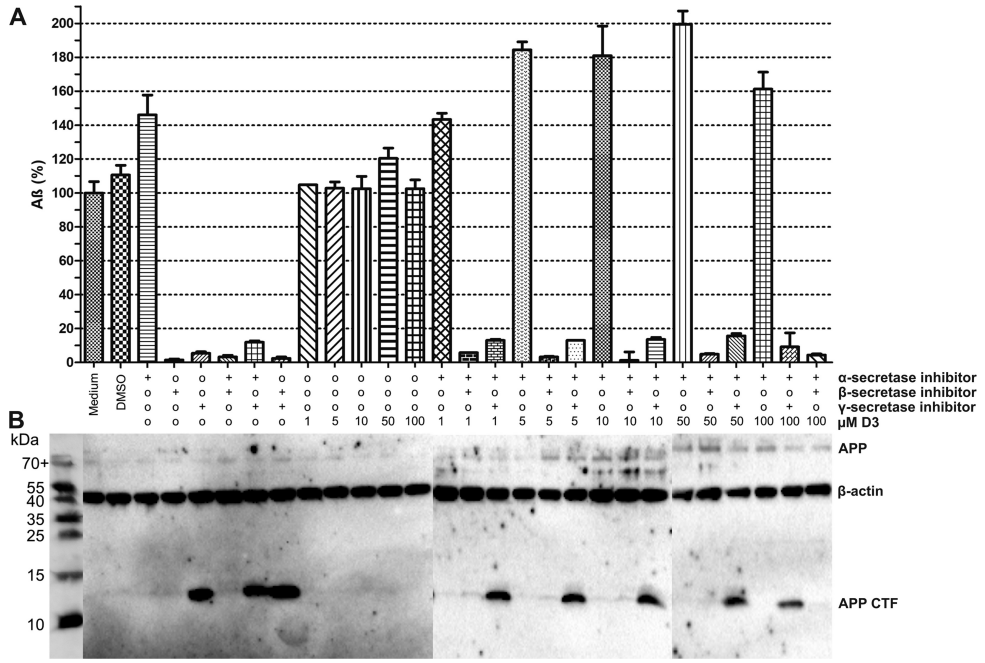

Figure 4.6: Influence of D3 on APP cleavage and Aβ42 generation studied by means of ELISA and western blotting. (A) U251-MG cells stably overexpressing wild-type human APP (U251-APP751) were treated for a period of 24 h with or without 1, 5, 10, 50, 100 µM D3 and/or 1 µM of the respective α-, β-, and γ-secretase inhibitors or the DMSO vehicle. Aβ42 levels in the conditioned media were analyzed by sandwich ELISA. The β- and γ-secretase inhibition abolished Aβ production, while D3 did not reduce the Aβ42 level. The ordinate corresponds to the Aβ concentration values normalized to the average daily generation without inhibitors or D3 peptides equal to 39.4 pg/mL. (B) Western blot analysis of cell lysate of U251-MG cells treated for a period of 24 h with or without 1, 5, 10, 50, 100 µM D3 and/or 1 µM of the respective inhibitors as in panel (A) or the DMSO vehicle. γ-Secretase inhibition induced strong accumulation of APP C-terminal fragments (CTF), while D3 induced no accumulation of the fragments.

APP sequence recognition by D3. Thus, the latter can stabilize the nascent helical conformation of the extracellular APP JM region similar to what has been described for flexible IDP/ IDP-like interactions of highly charged amphiphilic proteins near the membrane surface [297, 298].

Effects of interaction with D3 on the conformational behavior of the APP TM fragments were investigated experimentally using CD (Figure 4.12 and Table 4.1). The differential spectra with free APP TM fragment spectrum taken as a baseline are indicative of significant conformational redistribution caused by the interaction. Opposite chiralities of APP TM fragments and D3 introduce some uncertainty to interpretation of the spectra, formation of additional helices in the all-D-enantiomeric peptide D3, and L-enantiomeric APP TM fragments, yielding effects of opposite signs in the CD spectra, effectively canceling each other. However, according to NMR data discussed above, the apparent APP helicity remains largely unchanged, wherefore

the observed changes of CD spectra are likely to be associated with increased helicity of D3 consistent with its behavior in hydrophobic solvents (50 % trifluoroethanol water mixture, 25 % hexafluoroisopropanol water mixture) or negatively charged micelles (90 % DPC/ 10 % SDS). Thus, CD spectra are in favor of D3 interaction with the negatively charged APP JM region causing certain conformational rearrangements associated with increased D3 helicity similar to the changes caused by its exposure to hydrophobic solvents. This is consistent with the assumption that the interaction occurs in the vicinity of the membrane surface.

4.5.3 Interaction of D3 with APP Does Not Disturb APP Cleavage by Secretases.

The fact that D3 interacts with APP in the vicinity of the α-secretase cleavage site located between the metal-binding domain and the JM helix suggests competition between D3 binding and α-secretase recognition. Moreover, D3 may affect, directly or indirectly, the activities of other secretases. Overall, this would result in changes of concentrations of Aβ42 and C-terminal fragment (CTF) of APP.

To characterize the inhibitory/modulatory activity of D3 on any of the secretases and its effects on the generation pathway of Aβ42 toxic oligomers, western blot and ELISA experiments were performed (Figure 4.6). The concentrations of endogenic Aβ42, N-terminal water-soluble APP fragment, APP CTF, and β-actin control protein were determined in crude lysates of human glioblastoma U251-MG cells treated with D3 and inhibitors of α-, β-, and γ-secretases or DMSO as a control. As expected, β- and γ-secretase inhibition abolished Aβ42 production, while D3 did not significantly affect the Aβ42 level. The γ-secretase inhibition induced strong accumulation of APP CTFs, while D3 induced none. Based on these results, cleavage by γ- and β-secretases was not notably inhibited by D3 even at supersaturating concentrations; however, D3 concentrations close to K_d values can cause a certain inhibitory effect on α-secretase cleavage and/or slightly potentiate cleavage by β-secretase (at 50 μM D3, which is then compensated at 100 μM D3 probably by other mechanisms). This is consistent with the assumed interaction of D3 with the APP JM region in the vicinity of the α-secretase recognition site and in close proximity of the β-secretase site and provides direct evidence of interactions of the D3 peptide in micromolar concentrations with APP. Thus, D3 binding to APP had practically no effect on the native β-amyloid processing pathway, which is seemingly important for brain homeostasis, thus being presumably harmless to the organism [255, 256, 258, 302].

4.6. Discussion

Alzheimer's disease is a dramatic medical and social challenge as the lifespan increases progressively. Prevention of wider expansion of AD requires an understanding of both its pathogenesis and molecular mechanisms by which therapeutic substances affect various molecular targets involved in AD development stages, especially in amyloid production and nucleation.

D3-like peptides have been designed with the goal of preventing Aβ oligomerization and eliminating the already existing Aβ oligomers for AD treatment [303, 304]. One of the compounds, RD2, has already successfully completed phase I clinical studies [305]. Previously, it was shown that the D3-like peptides directly interact and destroy Aβ aggregates by converting them into nontoxic and nonamyloidogenic assemblies *in vitro* [280, 281] and improve cognition and memory deficits in different transgenic mouse models of AD *in vivo* [279, 280, 281]. Previous studies demonstrated that arginine-rich D3-like peptides lack well-defined structural features in aqueous environments and their binding to Aβ assemblies might resemble a specific high-affinity interaction between two small IDPs, characterized by variable stoichiometry [292]. Nevertheless, detailed structural information on the interaction of D3-like peptides with the Aβ sequence was needed for understanding the molecular mechanism of their functioning and hence for further optimization of AD treatment.

Assuming that the initial steps of amyloid nucleation can be prevented by targeting its precursor, we investigated D3 binding to CTFβ transmembrane fragment $APP_{672\text{-}726}$ and its amyloidogenic L723P mutant form embedded into the DPC micelles, which membrane-mimicking properties have been demonstrated in numerous structural studies of Aβ and APP TM fragments [267, 306, 307]. Notably, such a comprehensive structural study of the interaction of a therapeutic substance with the membrane-bound Aβ precursor was carried out here for the first time.

The present structural and modeling studies revealed that D3 can dynamically adapt and bind to the extracellular JM region of membrane-bound APP TM fragments (Figure 4.2-4.5 and Figure 4.13- 4.15). As evidenced by mutagenesis (Figures 4.3B,D and 4.4D), the electrostatic interactions presumably play an important role in the membrane-bound D3/APPmc complex, similar to the D3/Aβassociation observed in the bulk solution [292, 297]. Although the D3/APPmc complex persists during the entire MD simulations in the explicit lipid bilayer, the APP JM nascent helix and D3 interacting with it retain some mutual mobility, as is typical for coupled IDP/IDP-like recognition [297, 298].

The flexible IDP/IDP character of the interaction between the two peptides is illustrated by an almost identical PRE-NMR signal broadening pattern of membrane-bound APPmc upon

binding of both kinds of spin-labeled D3 with an MTSL-label covalently attached to either N- or C-terminus (Figure 4.4A,B). Dissociation constants determined by the MST assay for the native APPmc (direct Aβ precursor) and the fragment with double Arctic (E693G) and Iowa (D694N) mutations revealed only twice lower affinity in the case of the double mutant (Figure 4.2). (The best fit was obtained using a 1:1 binding model; other binding models deteriorated the fit.) Such a moderate decrease corroborated the IDP/IDP-like recognition of highly charged amphiphilic peptides with numerous intermolecular contacts holding the complex together and, in particular, the involvement of the negatively charged E693 and D694 side chains of APP in the local salt-bridge interactions with positively charged side chains of D3 residues.

In addition, the observed transient interactions of both molecules with the lipid headgroups (Figures 4.5 and 4.13) facilitate the presentation of D3 for recognition of the APP JM region and the corresponding sequence in Aβ species partially submerged into the membrane. It should be noted that the conformation of the APP JM sequence is very sensitive to the environment, including membrane composition, which can modulate conformational transitions and affect relative propensities for α- and β-structures [286, 287, 288, 306]. Similarly, we found that addition of 10 % of negatively charged SDS into DPC micelles caused partial folding of the positively charged D3 (presumably due to adsorption on the micelle surface) as evidenced by CD measurements (see Figure 4.12). Since Aβ is known to preferentially interact with negatively charged membranes[258, 302], such an effect of D3 interaction with negatively charged membranes on its conformational preferences is consistent with the idea that lipid membranes can play a role in the molecular mechanisms of D3 function.

Thus, D3-like peptides directly interact with APP fragments, including mature Aβ species, and reduce their oligomerization on the membrane surface, which can be attributed to stabilization of the helical conformation of the APP JM region and suppression intermolecular hydrogen bonding (suggested by MD) and hence inhibition of its conversion into the β- structure, similar to these effects in the bulk solution. Furthermore, our PRE-NMR and CD data revealed D3 binding to an amyloid-like oligomeric state of L723P-APPmc (Figures 4.3 - 4.5). This is consistent with that the corresponding flexible helical region of Aβ is exposed above the membrane surface in the recently obtained spatial structure of the six-stranded Aβ42 tetramer prepared in DPC [306]. Thus, this region is able to be recognized by D3-like peptides, causing formation of large nontoxic Aβ-aggregates observed experimentally [292, 308]. Similarly, D3-like peptides could limit Aβ binding (both in monomeric and oligomeric states) to membrane proteins, preserving their normal functioning.

Notably, the observed ability of D3 to bind to the Aβ part of APP near the membrane and to destabilize toxic Aβ-assemblies capable of perturbing cell membranes is presumably relevant to

AD treatment. Since this recognition site is located in the APP part sensitive to interactions with α- and β-secretases, we speculated that D3-like peptides potentially influence Aβ production. Our biochemical studies, however, did not reveal the significant influence of D3 on APP cleavage by either one of the secretases (Figure 4.6), which is consistent with the flexible IDP/IDP nature of the D3/APP interactions. Only a marginal increase of Aβ42 production was observed upon simultaneous addition of D3 with the α-secretase inhibitor, which suggests negligible functional interference between them. So, D3 does not interfere with the normal activities of secretases, and thus, D3 does not modulate the production of monomeric Aβ which may have important physiological functions [253, 254]. Although the exact normal physiological role of the Aβ monomers and oligomers remains unknown, they have been shown to act as ligands for a number of different receptors or as active components involved in the antimicrobial function of the innate immune system [253, 258, 271, 212]. We combined the observed and potential activities of D3-like peptides in the scheme shown in Figure 4.7.

4.7. Conclusion

The all-D-enantiomeric D3-like peptides were developed to directly destroy the cytotoxic aggregates of amyloid-β peptides responsible for AD progression. We conclude that beneficial effects of D3-like peptides may be explained by their potential ability to act on various aspects of AD relevant molecular events: Aβ conversion into β-conformation, toxic Aβ oligomerization, Aβ-induced perturbation of cell membranes, and inhibition of Aβ influence on membrane-associated and soluble protein functioning. The experimental results obtained in this study augmented by MD analysis of NMR-derived structures suggest that dynamic IDP/IDP-like interaction between the D3-like peptide and APP JM region results in decreased conformational lability, generally favoring α-helicity of the amyloidogenic region, reducing intermolecular hydrogen bond formation, and thus preventing Aβ conversion into β- conformation and subsequent toxic oligomerization. The achieved progress in understanding the molecular mechanism of action, in addition to the already demonstrated Aβ oligomer disassembling activity of D3 and its derivatives, of which one of them is in clinical development, constitutes an important step toward the development of an effective AD treatment strategy. Taking into account the identified localization of the interaction sites, the D3-like peptides can be presumably modified to modulate specifically the APP processing by secretases without affecting their activity for other substrates. Such an APP-specific effect on secretases has long been tried to obtain for secretase inhibitors without adverse side effects. Although such a compound may be beneficial only preventively, it would be extremely important to investigate whether secretase inhibitors and modulators failed due to offtarget effects or whether they failed because APP processing toward Aβ is physiologically

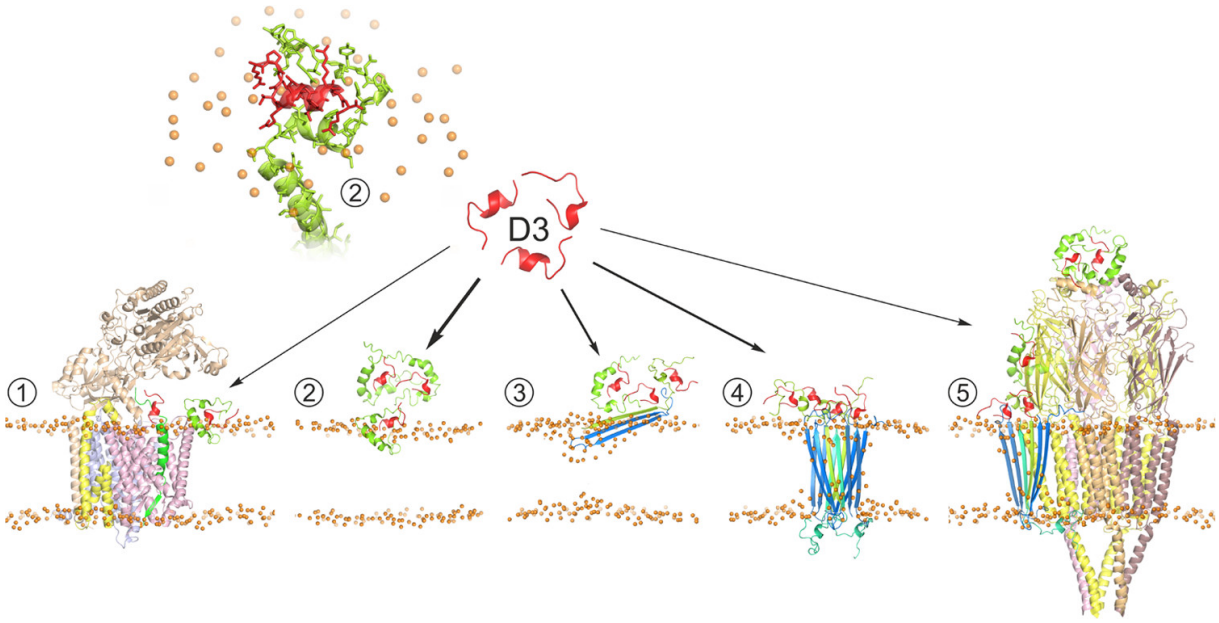

Figure 4.7: Schematic representation of the possible dynamic interactions of D3 with potential AD treatment targets. The following five aspects of flexible IDP/IDP-like D3/APP interactions restricting conformational diversity of the extracellular APP JM region *via* prevention of intermolecular hydrogen bond formation near the membrane surface (shown by orange phosphorous atoms of lipid heads) having implications for AD development are suggested based on the previously published data and the present study: (1) putative influence of D3 (shown in red) on abnormal APP processing, e.g., interaction with the APP TM fragment (in green) recognized by the γ-secretase complex [259], as well as with mature Aβ (in green) leaving the complex (the absence of this activity has been demonstrated for D3 (Figure 4.6), but since D3 is specific for APP as a substrate, adaption of D3 toward an APP-specific secretase inhibitor may become interesting in the future); (2) inhibition of Aβ conversion into β- conformation and subsequent toxic oligomerization by suppressing intermolecular hydrogen bond formation and stabilizing its nascent α-helical structure (the close up in the upper left corner illustrates the membrane-bound D3/APPmc complex revealed by the current structural studies); (3) depolymerization of fusible Aββ oligomers [306] by reducing intermolecular hydrogen bond formation in β-sheets (in green and blue); (4) inhibition of perturbation of cell membranes by Aβ through conversion of Aβ oligomers into nontoxic, nonamyloidogenic, and nonfibrillar assemblies (partially overlaps with item 3); and (5) preventing abnormal functioning of membrane-associated and soluble proteins, e.g., nicotinic acetylcholine receptor (nAChR), which can be inhibited by diverse Aβ oligomers in a different manner[253].

relevant, and its inhibition leads to adverse side effects. Optimization of D3-like compounds based on the results presented here has still a lot of room to obtain even more potent compounds for effective AD treatment and prevention.

4.8. Material and methods

4.8.1 Membrane-Bound APP Fragments.

Unlabeled and $^{15}N/^{13}C$-labeled recombinant peptide APPmc (D^{672}AEFRHDSGYEVHHQ^{686}KL VFFAEDVGSNKG^{700}AIIGLMVGGVVIATVIVITLVML^{723}KKK^{726}, $APP_{672\text{-}726}$ fragment; the metal-binding domain is in italic, and the hydrophobic TM segment is underlined) and its familial mutant variants (L723P-APPmc, E693G/D694N-APPmc, and E693G/D694N/L723P-APPmc) with E693G, D694N, and L723P amino acid substitutions (Figure 4.1A) were expressed and purified by elaborated protocols [290, 291]. The control TM fragment $EphA2_{523\text{-}563}$ of EphA2 receptor tyrosine kinase (EphA2tm) was obtained as described [301]. Purity of the TM fragments of APP and EphA2 is >95 % according to denaturing gel electrophoresis and reverse-phase HPLC (RP-HPLC). The TM fragments of APP and EphA2 were solubilized in an aqueous suspension of dodecylphosphocholine (DPC, for unlabeled fragments) or d_{38}-dodecylphosphocholine (d_{38}-DPC, 98 %, CIL) micelles under monomeric conditions with a protein/lipid ratio of 1:200, as described [267, 268].

4.8.2 Fluorescent- and Spin-Labeled D3.

The all-D-enantiomeric peptide D3 (consisting of 12 all D-enantiomeric amino acid residues and amidated C-terminus) (H-rprtrlhthrnr-NH_2, 1598.8 Da, purity $\geq$98.2 %), the C-terminally fluorescent-labeled D3 derivative D3Lys-(FAM) (H-rprtrlhthrnr-K-(FAM)-NH_2, 2086.39 Da, purity 98.2 %), and the D-cys derivatives of D3, namely, D3cys (H-rprtrlhthrnr-c-NH_2, 1702.0 Da, purity $\geq$95.7 %) and cysD3 (H-c-rprtrlhthrnr-NH_2, 1702.0 Da, purity $\geq$95.7 %) for subsequent in-house nitroxyl radical spin-labeling were custom-synthesized (Peptides and Elephants, Germany, or JPT, Germany). The purity, identity, and chirality of the peptides were confirmed by RP-HPLC, mass spectroscopy, and CD spectroscopy, respectively.

For paramagnetic relaxation enhancement (PRE) NMR experiments, nitroxyl radical spin-labeled analogues of D3 were synthesized by reacting (1-oxyl-2,2,5,5-tetramethyl-Δ3-pyrroline-3-methyl) methanethiosulfonate (MTSL) (Toronto Research Chemicals) with D3cys or cysD3, leading to covalent attachment of the MTSL nitroxyl radical spin-label to the N- or C-terminal D-cysteine residue ((MTSL)cysD3 or D3cys(MTSL)), respectively. Typically, a fivefold molar excess of MTSL over peptide, i.e., $\sim$4 mg of MTSL ($\sim$15 µmol), is freshly dissolved in 90 µL of N,N-dimethylformamide (DMF) and mixed with 810 µL of 200 mM HEPES/NaOH buffer, pH 7.6. The solution is then added to $\sim$5 mg ($\sim$3 µmol) of either lyophilized D3cys or cysD3. After incubation for 1-2 h at RT, the reaction mixture is applied to a semipreparative

RP-HPLC on a C8 column (Agilent Zorbax-300 SB, 9.4 mm x 250 mm column dimension, 300 µL of sample aliquots) connected to Agilent 1260 HPLC system. Purification of spin-labeled peptides (MTSL)cysD3 or D3cys(MTSL) was achieved by applying an aqueous acetonitrile (ACN) gradient (8 % ACN, 0.1 % trifluoroacetic acid (TFA) to 60 % ACN, 0.1 % TFA in Milli-Q water within 40 min), running at a flow rate of 4 mL min $^{-1}$ at 25 °C with ultraviolet absorbance detection at 214 nm. Purified spin-labeled samples are collected, aliquoted, flash-frozen in liquid N2, and freeze-dried *in vacuo* (LT-105, Martin Christ, Germany). This described procedure allows complete spin-labeling of D3cys or cysD3 with final purity of ∼98 %.

4.8.3 Affinity Measurements by Microscale Thermophoresis (MST), Microfluidic Diffusional Sizing (MDS), and Fluorescence Polarization (FP) in a Membrane-Mimicking Micellar Environment.

For MST experiments the C-terminally fluorescentlabeled D3 derivative D3Lys(FAM) was used to investigate binding of D3 to the control EphA2$_{523\text{-}563}$ TM fragment (EphA2tm), APP$_{672\text{-}726}$ TM fragment (APPmc), and its mutant variants by means of a Monolith NT.115 instrument (blue/green channel, NanoTemper Technologies). Pretests were performed to check the adsorption of D3Lys(FAM) to capillary walls and to find the concentration of D3Lys(FAM) suitable for MST measurements. D3 was extremely soluble, and it was found that D3Lys(FAM) does not adsorb to the walls of nanoDSF standard treated capillaries (NanoTemper Technologies). The concentration of D3Lys(FAM) suitable for MST measurements was selected constant to 200 nM. D3Lys(FAM) was mixed with the TM fragments (protein/lipid ratio of 1:200) in assay buffer (20 mM Tris/HCl pH 7.4 and 1.5 mM DPC (Anatrace)) in standard tubes (NanoTemper Technology) by 1:1 serial dilutions to obtain concentrations of the TM fragments from 50 µM to 1.5 nM. The mixture was immediately loaded into capillaries and analyzed at 20 %, 40 %, 60 %, and 80 % MST power and a light-emitting diode (LED) intensity of 20 %. Analysis of the interaction by thermophoresis was performed in the following time intervals: 5 s IR laser off-time, 40 s on-time, and 5 s off-time. Experimental data were analyzed by MO.Affinity Analysis v2.3 software (NanoTemper Technologies). Changes in the normalized fluorescence (ΔF_{norm}) with concentrations of the TM fragments were used to obtain a sigmoidal curve, and a 1:1 binding model shows the best fit. The dissociation constant (K_d) was determined by MO.Affinity Analysis v2.3 software, which uses Morrison equation extrapolation.

MDS was performed on a Microfluidity One-W instrument (Fluidic Analytics) by titrating various amounts of DPC-micellebound APPmc (0-250 µM) on 1 µM D3Lys(FAM) in 20 mM Tris/HCl buffer pH 7.4. Experiments were run at 26 °C in two to six replicates using the FAM fluorescence. The hydrodynamic radii of unbound D3Lys(FAM) (Rh free) and APPmc-bound

D3Lys(FAM) (Rh complex) were determined to 0.96 ± 0.01 and 3.3 ± 1 nm, respectively, and translated into apparent molecular masses of 1.4 kD (D3Lys(FAM), molecular mass of 2.1 kDa) or 56 kDa (D3Lys(FAM) bound to APPmc-loaded DPC micelles), respectively. Rh values of 3.4 ± 2 nm are typical for DPC micelles determined by alternative methods and indicate that binding of both APPmc and D3 retain the overall size of DPC micelles. Affinity data derived from MDS were fitted by Morrison equation extrapolation by means of LibreOffice 7.1.6.2.0+ Calc software, the FP data was analyzed in the same way. FP measurements were performed on a BMG Clariostar fluorescent plate reader (BMG Labtech) using a 384-well plate (No. 781892, Sensoplate plus, glass flat bottom, black wall, Greiner) using bottom optics. Titrations were performed with DPC-micelle-bound APPmc (0-200 µM) on 1 µM D3Lys(FAM) in 20 mM Tris/HCl buffer pH 7.4. Experiments were run at 25 °C in fluorescence polarization mode using fluorescence excitation at 482 nm (16 nm bandwidth) and fluorescence emission at 530 nm (40 nm bandwidth). Orbital shaking of 700 rpm for 5 s was applied before each measurement cycle, and ten cycles were averaged.

4.8.4 Circular Dichroism (CD) spectroscopy.

CD spectra were measured on a J-1100 spectropolarimeter (Jasco) in a 1 mm quartz cuvette at 20 °C using the following parameters: minimal shortest wavelength 180 nm, maximal wavelength 280 nm, digital integration time 4 s, data pitch 0.1 nm, and scanning speed 50 nm min^{-1}. Ten scans were acquired and summed for every sample. Spectra were corrected by subtracting the respective solvents' control spectra. Analysis of the CD spectra was performed with the DichoWeb on-line package (http://dichroweb.cryst.bbk.ac.uk). The CDSSTR algorithm and Reference set 4 were used for deconvolution [309]. Note that D3 consists of D-amino acid residues, leading to the CD spectrum mirrored at the x-axis compared to its L-enantiomeric counterpart.

4.8.5 Nuclear Magnetic Resonance (NMR) Spectroscopy in a Membrane-Mimicking Micellar Environment.

High-resolution heteronuclear NMR spectra of the $APP_{672-726}$ fragment (APPmc) and its mutant variants (0.2-0.4 mM samples) in 20 mM NaPi buffer solution, pH 6.9, 5 % D2O (v/v), were acquired at 30 °C on 600 and 800 MHz AVANCE III spectrometers (Bruker BioSpin) equipped with pulsed-field gradient triple-resonance cryoprobes. The ^{1}H, ^{13}C, and ^{15}N chemical shifts of APPmc and its mutant form at pH 6.9 were assigned using CARA software [310] by means of two- and threedimensional heteronuclear experiments [311]: $^{1}H/^{15}N$ HSQC (heteronuclear single quantum coherence spectroscopy), $^{1}H/^{13}C$ HSQC, $^{1}H/^{13}C$ HSQC-CT (constant time version with

an evolution period of 28.6 ms), $^{1}H/^{15}N$ TROSY (transverse relaxation optimized spectroscopy), $^{1}H/^{13}C/^{15}N$ HNCA, $^{1}H/^{13}C/^{15}N$ HN(CO)CA, $^{1}H/^{13}C/^{15}N$ HNCO, $^{1}H/^{13}C$ HCCH-TOCSY (with a mixing time of 17 ms), and ^{13}C- and ^{15}N-edited NOESY-HSQC (with a mixing time of 80 ms). Spectra were recorded with a nonuniform sampling of indirect dimensions and processed using qMDD software [312]. The backbone resonances of the peptides were assigned using the BEST-TROSY version [313] of the triple-resonance experiments based on the chemical shifts of the APP**686-726** fragment and its L723P mutant form previously obtained [267, 286]. To characterize the interaction of the spin-labeled D3 derivatives (MTSL)cysD3 or D3cys(MTSL) with the APP TM fragments, the relative decrease of the $^{1}H/^{15}N$ cross-peak intensity due to signal broadening caused by the proximity of the MTSL group along the amino acid residue sequence of the peptide was analyzed in the $^{1}H/^{15}N$ TROSY spectra (the uncertainties were estimated from the noise level). To obtain the baseline NMR spectra for comparison, in the control experiments, the nitroxyl radical spin-label was quenched by addition of 2 mM ascorbic acid.

4.8.6 Molecular Dynamics (MD) Simulations in an Explicit Lipid Bilayer.

To elucidate the details of the NMR-observed interactions of D3 with the APP TM fragments, MD simulations were performed in an explicit lipid bilayer using the GROMACS 5.1.4 package [314] and Amber99SB-ILDN force-field [315] with the TIP3P water model [316] and lipid parameters as described elsewhere [317]. In addition to the $APP_{672\text{-}726}$ fragment and its variant with familial mutation L723P (APPmc and L723P-APPmc, four MD traces per each), the truncated forms $APP_{686\text{-}726}$ (APPjmtm and L723P-APPjmtm, one MD trace per each) without the metal-binding domain were investigated. The initial monomeric conformations of APP TM fragments were derived from the NMR structures of the metal-binding domain (PDB ID: 1ZE7) [318] and the $APP_{686\text{-}726}$ fragment (PDB ID: 2LLM) [286] embedded into DPC micelles. Nonprotonated states (corresponding to pH 7) of ionogenic side chains of the histidine, aspartate, and glutamate residues were used.

Starting configurations of the simulated systems were obtained by inserting the APP TM fragments into a pre-equilibrated lipid bilayer consisting of 200 1-palmitoyl-2-oleoyl-sn-glycero-3-phosphocholine (POPC) molecules. The systems were solvated and counterions were added to make them electrically neutral. The initial configuration of the protein-membrane system for each MD simulation was selected based on the analysis of PRE-NMR signal broadening caused by the proximity of the nitroxyl radical spin-labeled group to the backbone amide and methyl groups according to the previously described procedure [293].

The starting conformation of D3 as a nascent helix was obtained after 1 μs MD simulations performed for free peptides having initially random coil conformations in explicit solvents. Since the simulation revealed substantial conformational variability of D3, its conformational preferences were calculated by superimposing backbone atoms using the RMSD conformational clustering algorithm, a cluster module from the GROMACS package. An RMSD cutoff of 0.5 nm was applied, and the largest clusters (with population $\geq$ 5 %) were extracted. Two antithetic conformational states of D3, the partially helical (nascent helix, cluster 1) and random coil (hairpinlike, cluster 2) conformations, derived on 600 ns and 200 ns of the MD trace, respectively, and corresponding to the most highly represented in the obtained conformational ensemble were used as starting configurations of the peptide in complex with the membrane-bound APP TM fragments. Positions of D3 were initially constrained using a linear/harmonic approach with a force constant of 1000 kJ x mol^{-1} x nm^{-2} within the distance interval 0-0.8 nm between the N- or C- terminus of D3 (N^H or C^O atom, respectively) and the protein residues: side-chain methyl group ($C\beta^{H3}$ atom) of Ala701; side-chain amide group ($N\delta^{H2}$ atom) of N698; and backbone amide groups (N^H atom) of L688, V689, and F691.

For all of the systems, the constraints were removed after 20 ns constrained MD relaxation, and MD calculations were continued for additional 200 ns. The integration time step was equal to 2 fs. The spherical cutoff function (1.2 nm) was used for truncation of van der Waals interactions, while the electrostatic interactions were treated using the particle-mesh Ewald summation (real space cutoff of 1.2 and a 0.12 nm grid with fourth-order spline interpolation). MD simulations were carried out with the imposed 3D periodic boundary conditions in the isothermal-isobaric (NPT) ensemble with a semiisotropic pressure of 1.013 bar scaled independently along the bilayer normal and in the bilayer plane at a constant temperature of 310 K. The temperature and pressure were controlled using a Nose-Hoover thermostat and a Parrinello-Rahman barostat with 0.5 and 10 ps relaxation parameters, respectively, and a compressibility of 4.5×10-5 bar-1 for the barostat. The temperatures of the protein, lipids, and water molecules were coupled separately. Conformational dynamics of the protein and its van der Walls contacts with lipid and water molecules were analyzed using the GROMACS package utilities. To map protein-water interactions, the numbers of direct van der Waals contacts between atoms within a 0.4 nm distance cutoff were estimated. MD simulation data were analyzed and visualized with PYMOL (Schroedinger, LLC).

4.8.7 Determination of Potential α-, β-, and γ-Secretase Inhibitory/Modulatory Activity.

To characterize the inhibitory/modulatory activity of D3 on α-, β-, and γ-secretases and its effects on the generation of Aβ42, western blot analysis and enzyme-linked immunosorbent assay (ELISA) were performed. The α-secretase inhibitor (# SML0789-5MG) and y-secretase inhibitor (# D5942) were purchased from Sigma-Aldrich, and β- secretase inhibitor (# 565794) was from Merck-Millipore (Darmstadt, Germany). Human amyloidβ (1-42) (FL) assay kit (# 27719) was purchased from IBL International, anti-APP (epitope LEVPTDGNAGLLAEPQIAMFC, 17-37 of full-length APP) antibody (# 28053) was from IBL International, anti-APP C-terminal (751-770) rabbit antibody (# 171610-50UL) was from Merck-Millipore (Darmstadt, Germany), and anti-β-actin (8H10D10) mouse monoclonal antibody (# 3700P) was from Cell Signaling Technology International. Human glioblastoma U251-MG cells stably overexpressing the wild-type human amyloid precursor protein (U251-APP751) were kindly provided by the laboratory of Prof. Carsten Korth (Department of Neuropathology, Heinrich Heine University, Duesseldorf, Germany). U251-MG cells were maintained in DMEM supplemented with pyruvate, 10 % FBS, and Pen/Strep and treated in 75 cm2 flasks for 24 h with or without 1, 5, 10, 50, 100 μM D3 and/or 1 μM of the respective inhibitors or the DMSO vehicle in a humidified incubator with 5 % CO2 at 37°C. Culture media were collected, and Aβ42 levels were analyzed by ELISA (human amyloidβ (1-42) (FL) assay kit) according to the manufacturer's protocol. Each sample was measured in triplicate. Crude cell lysates were prepared using NP40 lysis buffer (50 mM Tris HCl, 150 mM NaCl, 1 % Nonidet P-40, protease inhibitor, pH 7.8). Total protein was separated on a 16.5 % Tris-Tricine gel, and levels of full-length APP (holo-APP) and APP CTFs (including CTF α and β) were analyzed by western blotting using polyclonal anti-APP antibody (IBL) raised against amino acids 18-38 of full-length APP and anti-APP antibody (Millipore) raised against the C-terminal amino acids 751-770 of APP. Anti-β-actin antibody (Cell Signaling Technology) was used as the loading control.

4.9. Supporting information

Table 4.1: Secondary structure of D3. Secondary structure composition of D3 in various environment conditions and presence of APPmc fragment embedded into micelle according to the deconvolution of CD spectra (direct measurement of differential signals using the reference substances indicated in the left column).

D3 sample	helix	strand	others
H_2O	0.02	0.35	0.61
TFE:H_2O 1:1	0.12	0.26	0.60
HFIP:H_2O 1:3	0.10	0.28	0.61
DPC 0.2 %	0.05	0.34	0.59
DCP+SDS	∼0.15 (pure fit)	∼0.30 (pure fit)	∼0.48 (pure fit)
DPC+EphA2tm (D3:EphA2tm 1:1)	0.08	0.32	0.60
DPC+APPmc (D3:APPmc 1:1)	0.14	0.41	0.45

Table 4.2: Cluster analysis of D3. Cluster analysis of D3 conformations obtained by MD simulation in the explicit water. The largest clusters (>5 % populated, totally 1001 structures) were presented (fig. S2B). 1-μs MD simulation was performed starting from random coil conformation of D3 and revealed its substantial conformational variability in explicit water. Using GROMACS utility the occurring conformations were binned into 29 distinct clusters, in most of which the peptide was in random coil state (fig. S2D). However, one folded helical turn was present in some of the substantially populated clusters, and the cluster with two helical turns (fig. S2C) folded was the most highly populated one in the ensemble (about 39 % of total 1001 structures derived from the MD trace).

# cluster	# structures	# rmsd, nm
1	390	0.495
2	145	0.500
3	119	0.520
4	67	0.426

Table 4.3: D3 binding to membrane-bound APP TM fragments. MD simulations of D3 binding to the membrane-bound APP TM fragments (APP672-726, APPmc, and truncated APP686-726, APPjmtm) and their L723P-mutant forms. Helicity of the amyloidogenic APP JM region 686-696 (Aß15-25) and number of diverse intermolecular contacts in the complex are derived from the sets of MD runs starting with intermolecular constraints imposed between N- or C-terminus of D3 on APP JM region during first 20 ns followed by subsequent 200-ns unconstrained MD relaxation. The 20-ns constrained MD simulations started with the D3 in the random-coil (hairpin-like) or partially helical (nascent helix) conformation.

membrane-bound complex	**intermolecular H-bonds, MD runs # 1/2/3/4**	**intermolecular salt-bridges, MD runs # 1/2/3/4**	**intermolecular stacking, MD runs # 1/2/3/4**	**% helicity of $APP_{686-696}$, MD runs # 1/2/3/4**	**% helicity of D3, MD runs # 1/2/3/4**
D3					23
APPmc				63/83/72/81 (±75)	
helical C-constrained D3/APPjmtm	4.5	2	0	31	27
helical C-constrained D3/APPmc	4.31/5.1/3.8/7.1 (4.8±1.5)	1.2/1.9/2.3/4.2 (2.4±1.1)	0.8/1.8/1.0/0.1 (0.9±0.6)	61/57/83/86 (72±13)	61/71/51/39 (55±12)
helical N-constrained D3/APPmc	8.5	2.9	2.2	78	63
random-coil C-constrained D3/APPjmtm	2.2	1.5	0.6	20	0
random-coil C-constrained D3/APPmc	5.5/6.0/6.8/7.4 (6.4±0.7)	2.0/3.0/3.0/1.3 (2.3±0.7)	1.0/0.2/0.6/2.2 (1.0±0.7)	84/88/86/78 (84±4)	1/0/0/0 (0±0)
random-coil N-constrained D3/APPmc	3.7	1.5	0.5	82	2
L723P-APPmc				49/82/20/0 (38±30)	0 0
helical C-constrained D3/L723P-APPjmtm	2.8	2	0.5	48	45
helical C-constrained D3/L723-APPmc	4.1/6.0/6.1/9.3 (6.4±1.9)	1.7/3.6/3.4/3.6 (3.1±0.8)	1.4/1.3/0.8/1.7 (1.3±0.3)	4/1/28/4 (9±11)	52/48/48/9 (40±18)
random-coil C-constrained D3/L723P-APPjmtm	2.3	0.3	0.4	6	3
random-coil C-constrained D3/L723P-APPmc	6.8/5.2/10/8.4 (7.6±1.8)	3.6/3.5/5.2/5.1 (4.4±0.8)	1.1/1.8/1.9/2.5 (1.8±0.5)	60/67/67/50 (61±7)	20/0/0/0 (5±8)

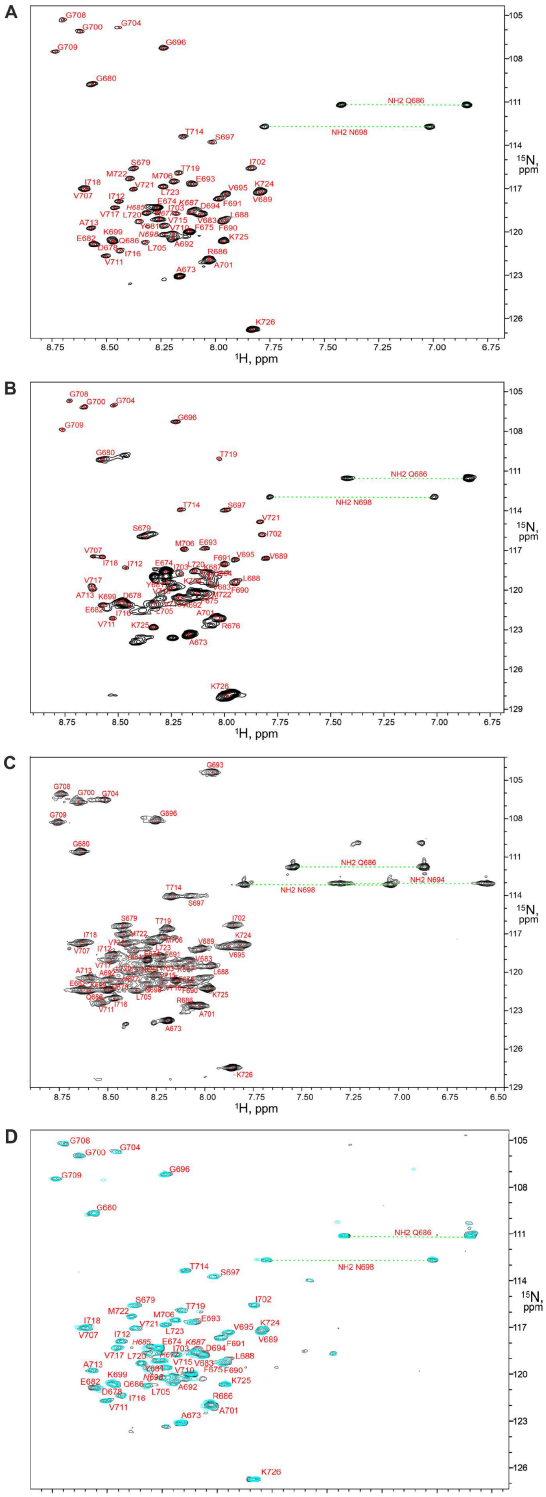

Figure 4.8: Heteronuclear 1H/15N-HSQC NMR spectra of wild-type and mutant APP TM fragments. APPmc (A), L723P-APPmc (B), and E693G/D694N-APPmc (C), embedded into DPC micelles at protein/lipid ratio of 1/200. Cross peak assignments of backbone and side chain amide groups are marked according to the APP sequence. (D) Overlaid 1H/15N-HSQC NMR spectra of free APPmc (black spectrum) and in the presence of unlabeled D3 (cyan spectrum) with D3/APP-fragment ratio of 2:1.

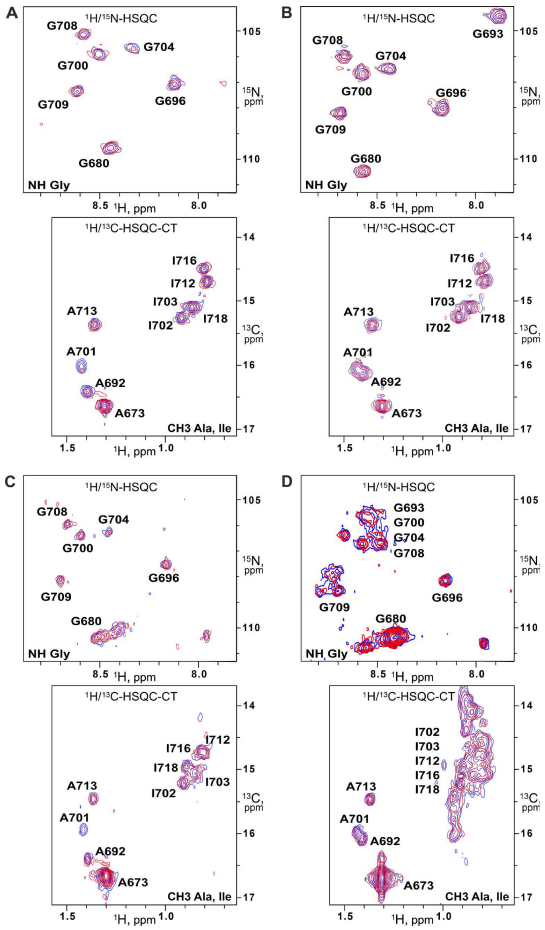

Figure 4.9: Representative regions of NMR spectra, 1H/15N-HSQC and 1H/13C-HSQC-CT, with amide and methyl group cross-peaks of Gly, Ala, and Ile residues of APP TM fragments. APPmc (A), E693G/D694N-APPmc (B), L723P-APPmc (C), and E693G/D694N/L723P-APPmc (D), embedded into DPC micelles in the presence of D3cys(MTSL) (red spectra) with D3/APP-fragment ratio of 2:1 and after quenching nitroxyl spin-label (blue spectra).

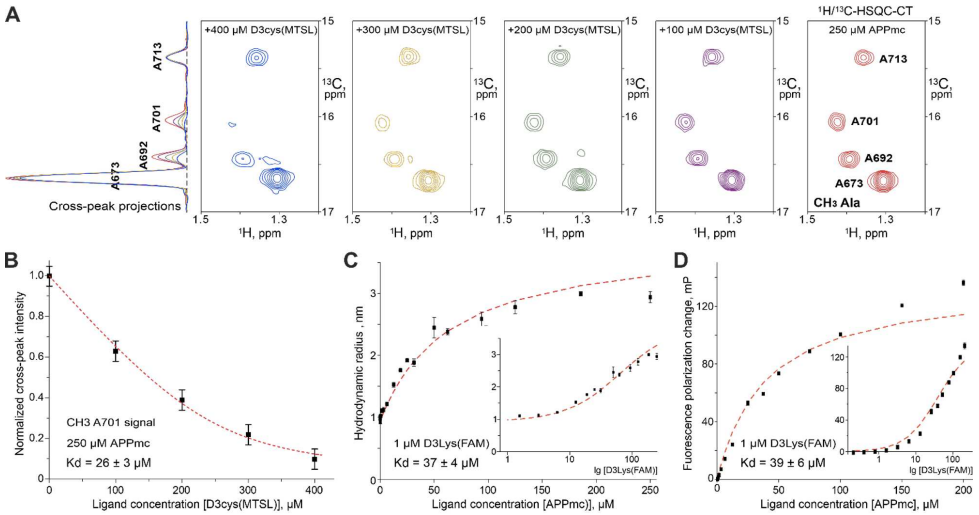

Figure 4.10: Affinity measurements of D3 towards DPC-micelle bound APPmc by alternative methods. (A) The selective decreasing cross-peak intensities of Ala methyl groups in 1H/13C-HSQC-CT spectra upon titration of DPC-micelle bound APPmc by D3cys(MTSL) are shown. (B-D) Determination of dissociation constant Kd of D3 with DPC-micelle bound APPmc performed (in addition to Micro-Scale Thermophoresis (see Fig. 2)) by means of NMR (B), Microfluidic Diffusional Sizing (C), and Fluorescence Polarization (D) methods are presented.

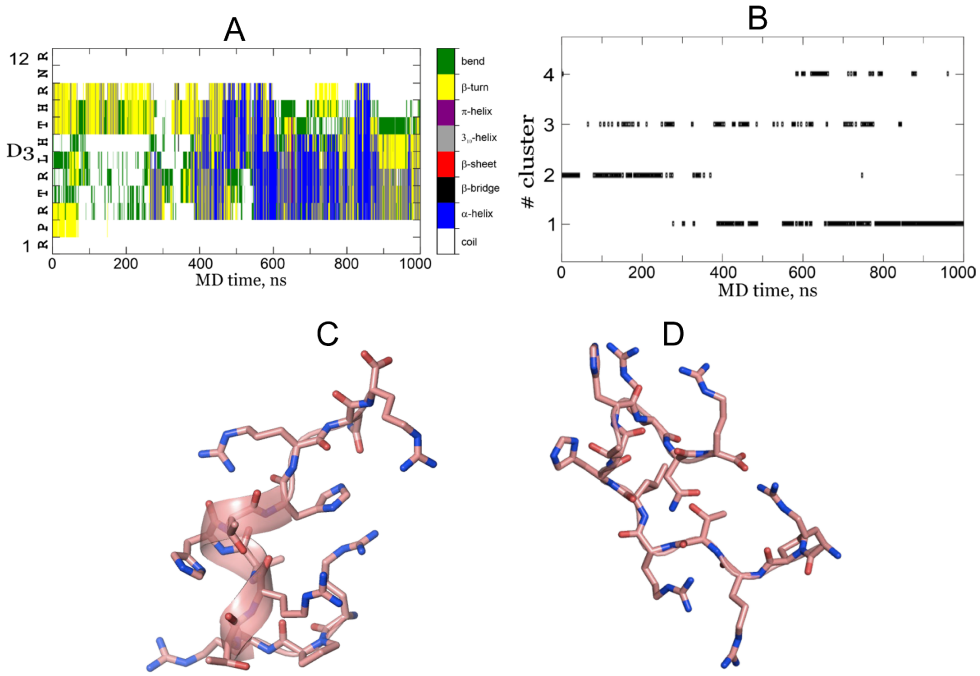

Figure 4.11: Conformational lability of D3 in explicit water. (A) D3 secondary structure evolution along 1-μs MD simulation in explicit water. The color-codding bar of the secondary structure elements is shown in right. (B) The distribution of the most highly represented D3 conformations, corresponding to first 4 clusters (>5 % populated), along the MD trace are shown by black dots. (C) A representative structure of D3, belonging to cluster 1 and derived on 600 ns, has partially helical (nascent helix) conformation. (D) A representative structure of D3, belonging to cluster 2 and derived on 200 ns, has random-coil (hairpin-like) conformation.

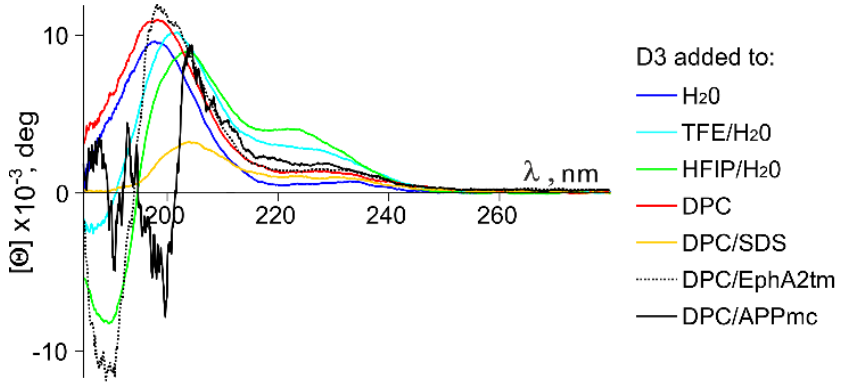

Figure 4.12: Conformational behavior of free D3 in different environments and upon its binding to the APP TM fragment monitored by CD spectroscopy. Differential CD spectra of the all-D-enantiomeric peptide D3 in several environment solution conditions (used as the reference substances) specified in the right corner vertically down: 50 mM potassium phosphate buffer pH 7.4 (blue); 50 % trifluoroethanol (TFE) water mixture (light blue); 25 % hexafluoroisopropanol (HFIP) water mixture (green); DPC micelles (red) or mixed 90 % DPC/ 10 % SDS micelles (orange) with concentration of 0.2 % w/v in the potassium phosphate buffer; 0.5 mg/ml EphA2tm embedded into 0.8 % w/v DPC micelles (dotted black) (protein/lipid ratio was 1/200) in the potassium phosphate buffer (in all experiments D3 concentration was 0.2 mg/ml, corresponding to D3/EphA2tm ratio of 1:1); 0.7 mg/ml APPmc embedded into 0.8 % w/v DPC micelles (black) (protein/lipid ratio was 1/200) in the potassium phosphate buffer (in all experiments D3 concentration was 0.2 mg/ml, corresponding to D3/APP-fragment ratio of 1:1).

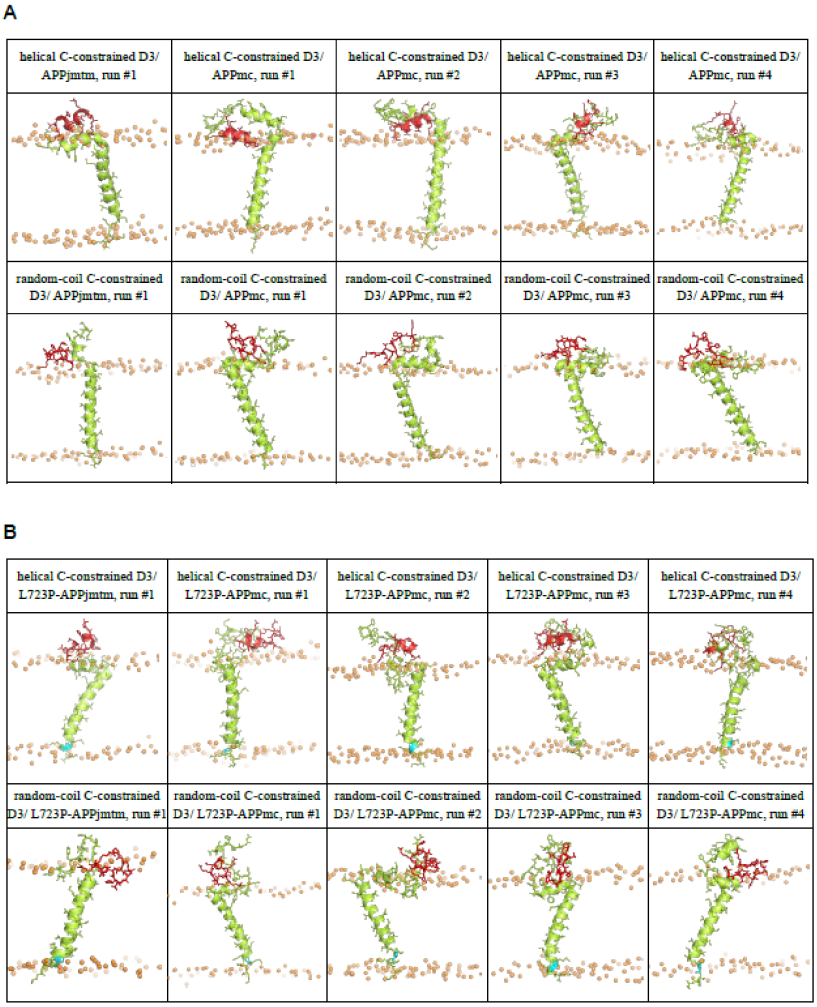

Figure 4.13: Spatial structures of the complex of D3 with membrane-bound APP TM fragments. (A-C) Spatial structures of the complex of D3 with membrane-bound APP TM fragments (APP672-726, APPmc, and truncated APP686-726, APPjmtm) and their L723P-mutant forms obtained by the unconstrained 200-ns MD runs performed after the 20-ns constrained MD simulations started with different D3 conformations specified on top (see table S3). The intermolecular constraints were imposed between (A and B) C- or (C) N-terminus of D3 on APP JM region (see Material and Methods). D3, APP TM fragments, and POPC lipid phosphorous atoms are colored by red, green, and orange, respectively. The L723P-mutation is highlighted in cyan. Cytoplasmic leaflet of lipid bilayer is on the bottom.

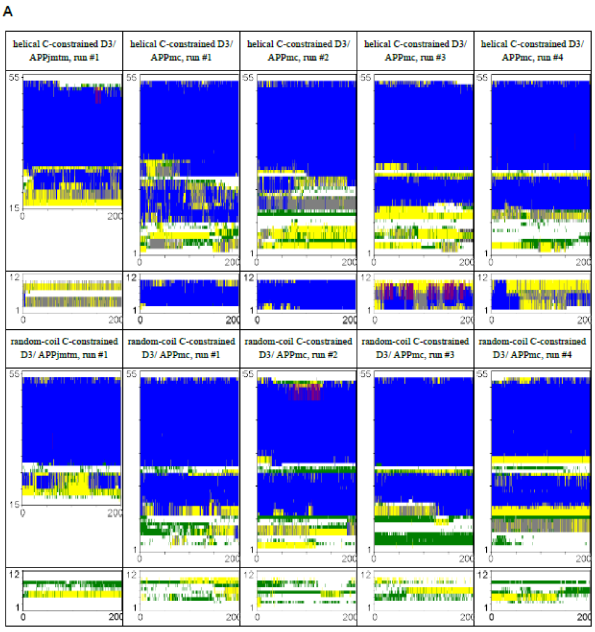

Figure 4.14: Secondary structure evolution of D3 in the complex with membrane-bound APP. Secondary structure evolution of D3 in the complex with membrane-bound APP TM fragments (APP672-726, APPmc, and truncated APP686-726, APPjmtm, corresponding to Aß1-55 and Aß15-55, respectively) and their L723P-mutant forms during 200-ns unconstrained MD simulations in the explicit POPC bilayer. Secondary structure patters are derived using GROMACS utility from the sets of MD runs starting with intermolecular constraints imposed between (A and B) C- or (C) N-terminus of D3 on APP JM region during first 20 ns followed by subsequent unconstrained 200-ns MD (listed in table S3 and fig. S6). The color-codding bar of the secondary structure elements is shown in (D). Ordinate – residue numbering, abscissa – MD trace timing (in ns).

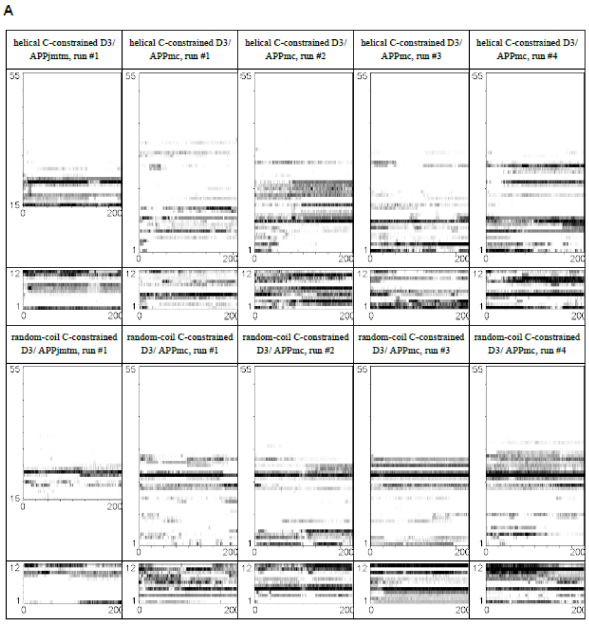

Figure 4.15: Evolution of the intermolecular contacts in the complex of D3 with membrane-bound APP. Evolution of the intermolecular contacts in the complex of D3 with membrane-bound APP TM fragments (APP672-726, APPmc, and truncated APP686-726, APPjmtm, corresponding to Aß1-55 and Aß15-55, respectively) and their L723P-mutant forms during 200-ns unconstrained MD simulations in the explicit POPC bilayer. Intermolecular contacts are derived using GROMACS utility from the sets of MD runs starting with intermolecular constraints imposed between (A and B) C- or (C) N-terminus of D3 on APP JM region during first 20 ns followed by subsequent unconstrained 200-ns MD (listed in table S3 and fig. S6). Intermolecular contacts are color-coded in gradation of gray according to the number of direct van-der-Waals contacts between atoms with 0.4 nm distance cut-off from white (no contacts) to black (10 protein-protein contacts). Ordinate – residue numbering, abscissa – MD trace timing (in ns).

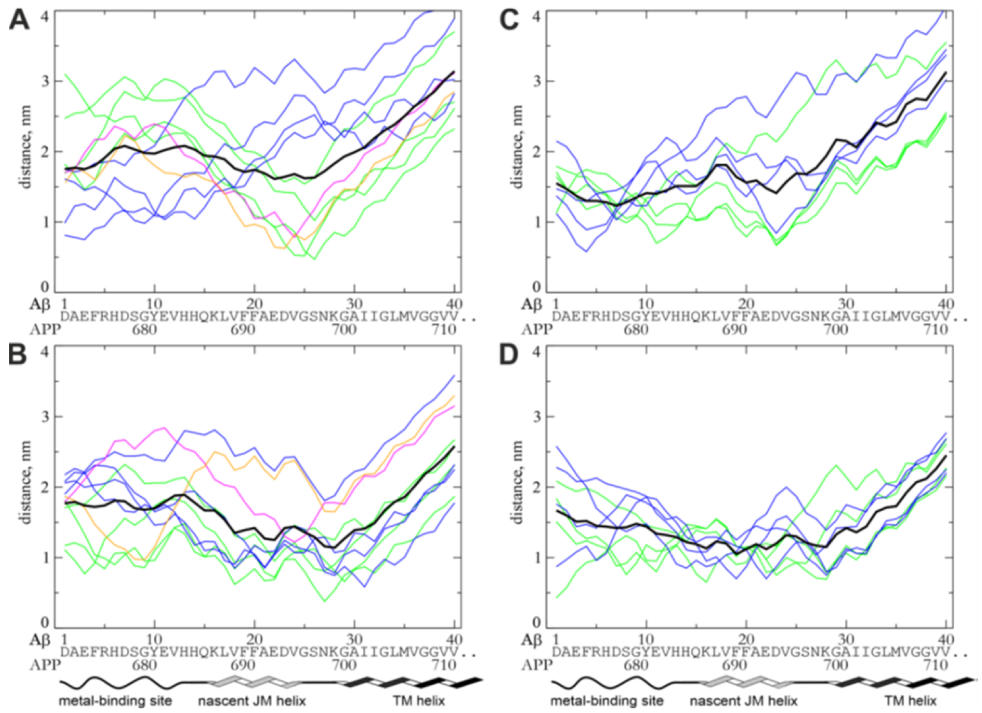

Figure 4.16: Proximity of the D3 termini to the APP JM residues during the MD simulations. (A and B) Proximities defined as the distances (between heavy atoms) from APPmc amide groups to the N- and C-termini of D3, respectively, averaged over 200-ns unconstrained MD runs corresponding to fig. S6, A and C. (C and D) Proximities defined as the distances from L723P-APPmc amide groups to the N- and C-termini of D3, respectively, averaged along 200-ns unconstrained MD runs corresponding to fig. S6B. The proximity curves derived from the sets of the MD runs starting with intermolecular constraints imposed between APP JM region and C-terminus of D3 having partially helical (nascent helix) and random-coil (hairpin-like) conformations are shown in blue and green, respectively. The proximity curves derived from the MD runs starting with intermolecular constraints imposed between APP JM region and N-terminus of D3 having partially helical (nascent helix) and random-coil (hairpin-like) conformations are shown in yellow and magenta, respectively. The black curves represent arithmetic average of all the proximity curves in each panel.

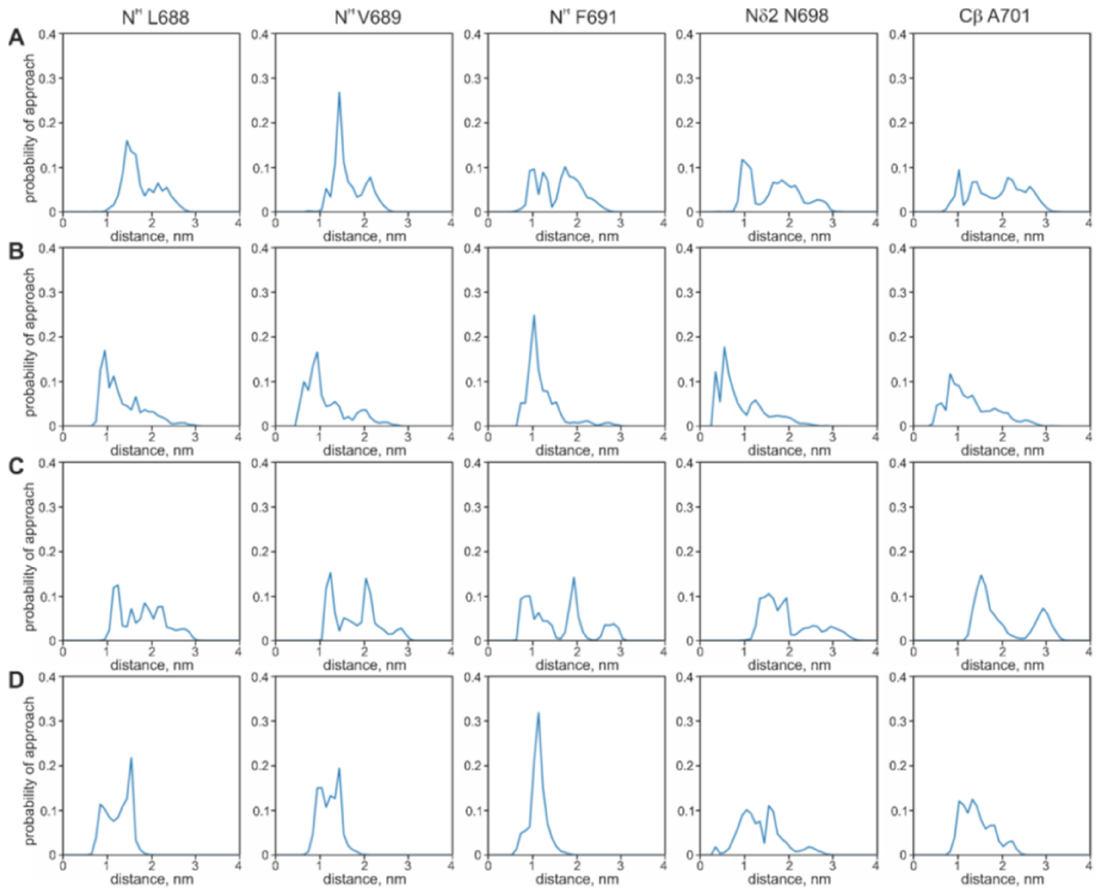

Figure 4.17: Distribution of distances from D3 peptide C- and N- termini to APPmc groups during unconstrained 200 ns simulations. All MD frames from all runs for APPmc and L723P-APPmc were binned according to proximity between the given groups with the step of 0.1 nm, and the fraction of the frames within the band was taken as a measure of likelihood of the groups approaching to a given distance. All the groups constrained during initial 20 ns of MD simulation are shown in the Figure. It is noteworthy that in NMR experiments complete PRE NMR signal broadening (scaling as 1/(distance)6) occurs at 1 nm proximity to the label, which was bound to D3 peptide via an additional D-cysteine residue.

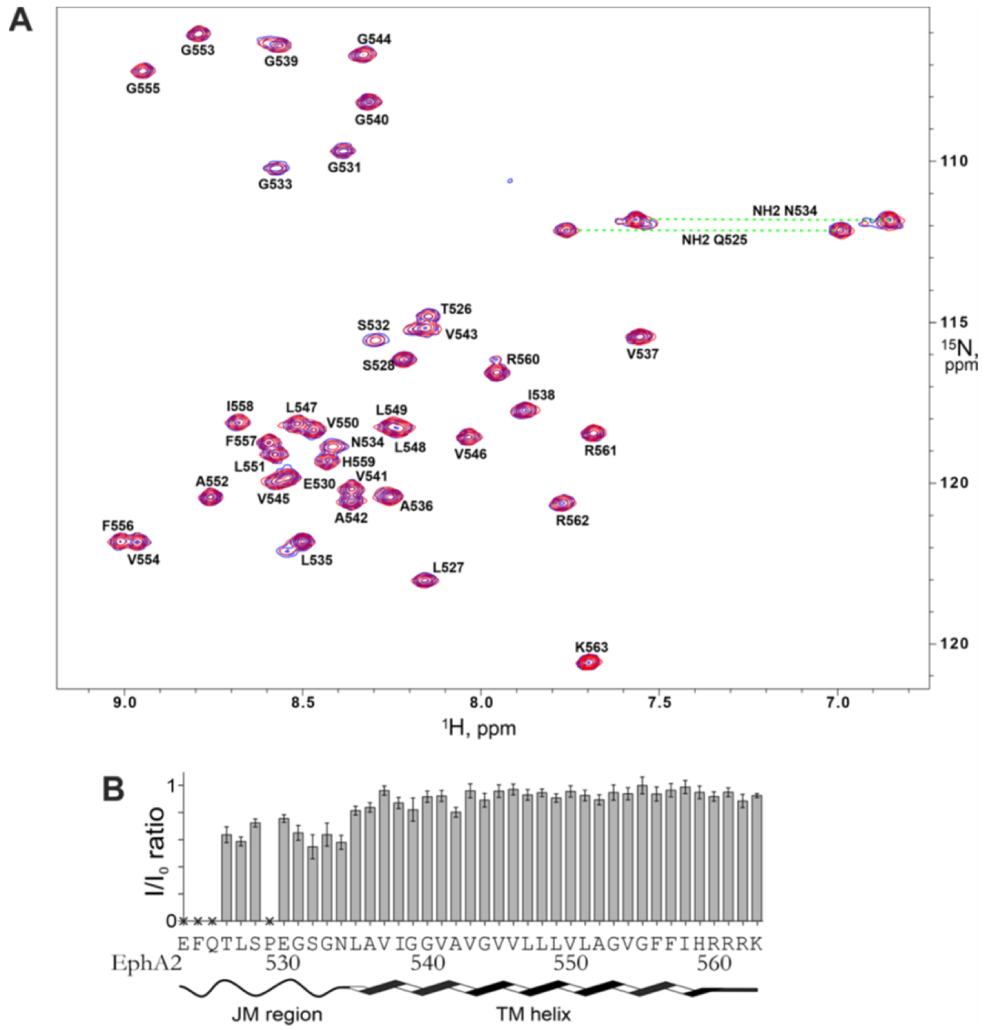

Figure 4.18: Control NMR experiment of D3 binding to another TM fragment of type I membrane receptor. (A) Overlaid NMR spectra 1H/15N-HSQC of EphA2 TM fragment, embedded into DPC micelles in the presence of D3cys(MTSL) (red spectra) with D3/EphA2tm ratio of 2:1 and after addition of ascorbic acid (blue spectra), when the nitroxyl spin-label is quenched. (B) PRE-NMR signal broadening patterns for amide groups of EphA2tm after addition of (MTSL)cysD3 with D3/EphA2tm ratio of 2:1. The datapoints corresponding to unassigned cross-peak positions or strongly overlapping cross-peaks of the amide groups are marked by diagonal crosses.

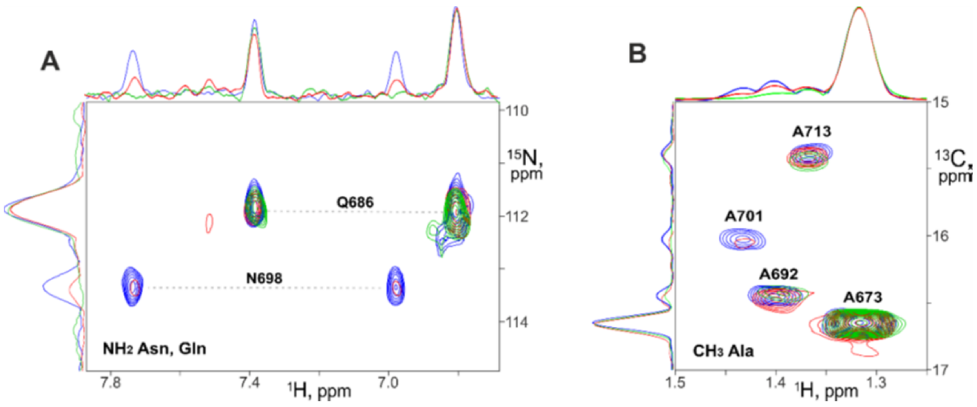

Figure 4.19: Control competition NMR experiment of D3 binding to membrane-bound APPmc and another TM fragment of type I membrane receptor. (A) Overlaid fragments of NMR spectra 1H/15N-HSQC (A) and 1H/13C-HSQC (B) of 50 μM 13C/15N-isotope-labeled APPmc (free fragment, blue spectra), in the presence of 300 μM D3cys(MTSL) (green spectra) and after addition of 500 μM unlabeled EphA2tm (red spectra) with peptide/DPC ratio of 1/200. Projections of the spectra are shown by the sides.

5

CONCLUSION & OUTLOOK

The conversion of huPrP from a native, partially folded conformation, to an amyloid state characterized by substantial amount of β-sheet structure is the key event in the pathology of prion diseases. The well-known 129M/V polymorphism links genetic predisposition to differences in prion pathology and susceptibility to certain diseases. The differences in structure, stability, and aggregation behavior of these two variants on a molecular basis may be related to the differences in pathology.

To conduct studies on the aggregation behavior of full-length huPrP expressed in *E. coli*, acidic pH was necessary to increase solubility and additional destabilization by denaturant was utilized to promote structural conversion. A relatively low concentration of 0.5 M GdnHCl was required to destabilize the globular domain of full-length huPrP and enable amyloid formation. The structure of both the 129M and 129V variants primarily consists of α-helical and random coil structure before the destabilization with denaturant. However, the shift in peak minimum observed with CD for the 129M variant indicated a higher proportion of random coil structure. This in turn might explain the stronger effect of thermal denaturation on the 129V variant, involving more ordered structure. This conclusion was supported by MD simulations, which revealed higher structural stability for the 129M variant. The two variants clearly had distinct aggregation behavior, with the 129M variant showing multiphasic kinetics. The complexity of the aggregation kinetics correlated well with the amount of oligomers. The 129M variant contains about 30 % oligomers, which could be the molecular basis for the different plateaus observed in the complex aggregation kinetics (Figure 5.1). The 129V variant is predominantly monomeric and exhibits aggregation kinetics that resemble an elongation-like mechanism starting from a destabilized monomer state. In addition, it was demonstrated that oligomers formed initially after addition of denaturant, appear to undergo structural rearrangement to further increase ThT binding capacity, rather than dissolve first as off-pathway aggregates.

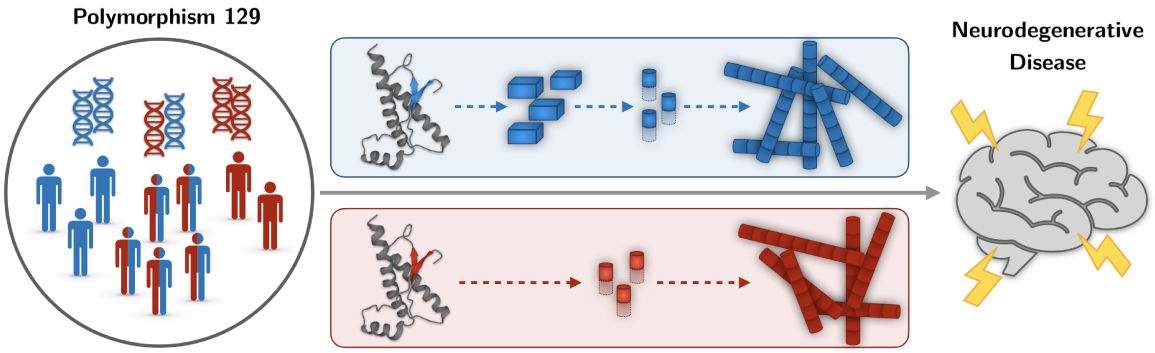

Figure 5.1: Aggregation model of polymorphism 129M/V of the human prion protein. Based on a pool of the population reflecting the genetic predisposition of polymorphism 129M/V of huPrP. More than half of the population is herterozygous at position 129. About 30 % of the population is homozygous for methionine at position 129 (blue) and the remaining minority is homozygous for valine at position 129 (red). Depending on the amino acid at position 129 of huPrP, we suspect different pathways of amyloid formation. The 129M variant appears to reflect an oligomer-mediated pathway, whereas the 129V variant exhibits elongation-like kinetics that begin with a destabilized monomer. These differences could be the basis for different pathologies of prion diseases and the susceptibility and age of onset of these diseases. Monomer structure based on PDB entry: 1FO7.

Interestingly, a shorter construct of the 129M variant, huPrP (121-230) lacking the unstructured N-terminus, showed a reduced amount of oligomers in line with simple aggregation kinetics without multiple plateaus, similar to the full-length 129V variant. This result supports the importance of the flexible N-terminus when investigating huPrP conversion. Shorter constructs lacking the unstructured N-terminus are commonly used in studies focusing on high-resolution structures of PrP^{C} [240] and amyloid fibrils of PrP^{Sc} [319, 320, 321], as well as the structural conversion [322, 240, 323, 324]. Short constructs have also been used in studies focusing on the 129M/V polymorphism, revealing neither an effect on structure, stability, and folding [35] nor a dependence on conversion propensity [325].

From this work, we conclude that the differences between the two huPrP variants become apparent only if the full-length protein is examined. It appears that the effect of a single amino acid exchange at position 129 is masked by the depletion of the 98 amino acid N-terminal half. This emphasizes the result of Zahn et al. from 2000 [52] that the N-terminal region interacts with the C-terminal region, forming a transient complex. This complex might affect oligomerization and amyloid formation depending on the polymorphism at position 129.

Considering that huPrP is actually a GPI-anchored glycoprotein, such PTMs might impact the results of studies on structure or conversion, especially if we consider the above-mentioned enormous impact of the substitution of a single amino acid or the presence of the unstructured N-terminal region. Understanding the disease-causing structural conversion of huPrP close to native properties should be the aspiration of most studies. Of note, most studies on the recombinant huPrP expressed in *E. coli* were performed at acidic pH to ensure solubility considering the theoretical isoelectric point of 9.4 and the missing membrane anchoring. The most striking shortcoming of recombinant protein expression in *E. coli* is the inefficiency in assisting the folding of eukaryotic proteins, such that only about 15 % of eukaryotic proteins are in their active form [326]. This may be due to the lack of PTMs, which are often essential for the functionality of eukaryotic proteins. Therefore, the second part of this work presents an eukaryotic expression system, that allows for stable expression of native-like full-length huPrP (129M variant), including GPI-anchoring and mammalian-like glycosylation. A straight-forward purification protocol was established, which yielded 1 mg native-like huPrP per liter culture, solubilized in DDM micelles. In summary, this protocol enabled the production of native-like huPrP on a large scale with high homogeneity and high similarity to the native protein expressed in the human brain. This protocol combines the advantages of *ex vivo* huPrP material with regard to similarity to human PTMs and thus structural similarities to humans, and the advantages of recombinant protein expression in *E. coli* such as high protein yield and inexpensive cultivation.

To highlight the advantages of this full-length native-like huPrP expressed in *L. tarentolae*, it was compared to full-length huPrP expressed in *E. coli*. Clear differences were observed in structure and stability. CD spectroscopy measurements of the purified native-like huPrP at physiological pH showed an α-helical dominated conformation, typical of huPrP^{C}. HuPrP from *E.coli* at pH 7.4 presented a shift towards β-sheet structure. Furthermore, oligomerization was compared between both proteins using SV measurements. At physiological pH, native-like huPrP is predominantly monomeric (86 %), whereas the remaining 14 % have an *s*-value corresponding to a dimer. Under identical conditions, huPrP from *E.coli* is not completely soluble and tends to form aggregates. Only 21 % of the remaining soluble protein was found to be in a monomeric state.

To circumvent these problems of low solubility at physiological pH and lack of similarity to humans, future studies could be based on native-like huPrP expressed in the eukaryotic expression system *L. tarentolae*. The ability of *L. tarentolae* to produce significant amounts of isotopically labeled recombinant proteins has already been shown [248, 249]. Cultivation in a synthetic medium for selective $^{13}C/^{15}N$-labeled valine can be used for NMR studies, for example. *L. tarentolae* showed auxotrophy for several amino acids (V, R, H, M, W, F, S, Y, T, L, and K), making it a suitable system for high-resolution structural analysis of the soluble and partially

folded huPrP^{C} by solution NMR, as well as the highly ordered amyloid fibrils based on huPrP^{Sc} by solid-state NMR [327, 180]. The latter can also be investigated by cryo-EM. In order to study the amyloid state of native-like huPrP, aggregation kinetics need to be established. In general, this system can also be used to characterize the aggregation behavior of the 129M/V huPrP variants at physiological pH. To get even closer to physiological conditions, the aggregation kinetics can be further investigated using a combination of both variants, representative for heterozygous individuals. This would represent the majority of the population and help to understand why heterozygous carriers are less susceptible to most prion diseases. The importance of the N-terminus can also be further investigated *in vitro*, using shorter constructs of huPrP that are also physiologically relevant, such as the cleavage products of α-, β-, γ- secretases as well as shedding.

These structural findings can then be used in a next step to develop potential therapeutics that could either stabilize the native structure of huPrP^{C} and prevent amyloid formation or eliminate potentially toxic species.

6

LITERATURE

[1] Prusiner SB (1982) Novel proteinaceous infectious particles cause scrapie. Science 216(4542):136–144

[2] Riesner D (2004) Transmissible spongiform encephalopathies: the prion theory-background and basic information. Contributions to microbiology 11:1–13

[3] Aguzzi A, Calella AM (2009) Prions: protein aggregation and infectious diseases. Physiological reviews 89(4):1105–1152

[4] McKinley MP, Bolton DC, Prusiner SB (1983) A protease-resistant protein is a structural component of the scrapie prion. Cell 35(1):57–62

[5] Weissmann C, Enari M, Klöhn PC, Rossi D, Flechsig E (2002) Transmission of prions. The Journal of infectious diseases 186(Supplement_2):S157–S165

[6] Alper T, Haig DA, Clarke MC, et al. (1966) The exceptionally small size of the scrapie agent. Biochemical and biophysical research communications 22:278–284

[7] Alper T, Cramp W, Haig DA, Clarke MC (1967) Does the agent of scrapie replicate without nucleic acid? Nature 214(5090):764–766

[8] Griffith JS (1967) Nature of the scrapie agent: Self-replication and scrapie. Nature 215(5105):1043–1044

[9] Prusiner SB, McKinley MP, Groth DF, Bowman KA, Mock NI, Cochran SP, Masiarz FR (1981) Scrapie agent contains a hydrophobic protein. Proceedings of the National Academy of Sciences 78(11):6675–6679

[10] Prusiner SB (1989) Scrapie prions. Annual review of microbiology 43(1):345–374

[11] Stahl N, Borchelt DR, Hsiao K, Prusiner SB (1987) Scrapie prion protein contains a phosphatidylinositol glycolipid. Cell 51(2):229–240

[12] Prusiner SB, McKinley MP, Bolton DC, Bowman KA, Groth DF, Cochran SP, Hennessey EM, Braunfeld MB, Baringer JR, Chatigny MA (1984) Prions: methods for assay, purification, and characterization. Methods in virology 8:293–345

[13] Prusiner SB, Groth DF, Bolton DC, Kent SB, Hood LE (1984) Purification and structural studies of a major scrapie prion protein. Cell 38(1):127–134

[14] Prusiner SB, Bolton DC, Groth DF, Bowman KA, Cochran SP, McKinley MP (1982) Further purification and characterization of scrapie prions. Biochemistry 21(26):6942–6950

[15] Weissmann C (1991) A'unified theory'of prion propagation. Nature 352(6337):679–683

[16] Basler K, Oesch B, Scott M, Westaway D, Wälchli M, Groth D, McKinley M, Prusiner S, Weissmann C (1986) Scrapie and cellular prp isoforms are encoded by the same chromosomal gene. Cell 46(3):417–428

[17] Stahl N, Baldwin MA, Teplow DB, Hood L, Gibson BW, Burlingame AL, Prusiner SB (1993) Structural studies of the scrapie prion protein using mass spectrometry and amino acid sequencing. Biochemistry 32(8):1991–2002

[18] Prusiner SB (1987) Prions causing degenerative neurological diseases. Annual review of medicine 38(1):381–398

[19] Oesch B, Westaway D, Wälchli M, McKinley MP, Kent SB, Aebersold R, Barry RA, Tempst P, Teplow DB, Hood LE, et al. (1985) A cellular gene encodes scrapie prp 27-30 protein. Cell 40(4):735–746

[20] Meyer-Luehmann M, Coomaraswamy J, Bolmont T, Kaeser S, Schaefer C, Kilger E, Neuenschwander A, Abramowski D, Frey P, Jaton AL, et al. (2006) Exogenous induction of cerebral ß-amyloidogenesis is governed by agent and host. Science 313(5794):1781–1784

[21] Cuille J (1939) Experimental transmission of trembling to the goat. CR Seances Acad Sci 208:1058–1060

[22] Miller MW, Williams ES, Hobbs NT, Wolfe LL (2004) Environmental sources of prion transmission in mule deer. Emerging infectious diseases 10(6):1003

[23] Gajdusek DC (1965) Slow, Latent, and Temperate Virus Infections: Ed. by D. Carleton Gajdusek [et Al. 2, National Institute of Neurological Diseases and Blindness

[24] Kimberlin RH, Wilesmith JW (1994) Bovine spongiform encephalopathy. epidemiology, low dose exposure and risks. Annals of the New York Academy of Sciences 724:210–220

[25] Hill AF, Desbruslais M, Joiner S, Sidle KC, Gowland I, Collinge J, Doey LJ, Lantos P (1997) The same prion strain causes vcjd and bse. Nature 389(6650):448–450

[26] Collinge J, Whitfield J, McKintosh E, Frosh A, Mead S, Hill AF, Brandner S, Thomas D, Alpers MP (2008) A clinical study of kuru patients with long incubation periods at the end of the epidemic in papua new guinea. Philosophical Transactions of the Royal Society B: Biological Sciences 363(1510):3725–3739

[27] Maignien T, Beringue V, Dormont D, Deslys JP, et al. (1999) Pathogenesis of the oral route of infection of mice with scrapie and bovine spongiform encephalopathy agents. Journal of General Virology 80(11):3035–3042

[28] Jeffrey M, Ryder S, Martin S, Hawkins S, Terry L, Berthelin-Baker C, Bellworthy S (2001) Oral inoculation of sheep with the agent of bovine spongiform encephalopathy (bse). 1. onset and

distribution of disease-specific prp accumulation in brain and viscera. Journal of comparative pathology 124(4):280–289

[29] Bons N, Mestre-Frances N, Belli P, Cathala F, Gajdusek DC, Brown P (1999) Natural and experimental oral infection of nonhuman primates by bovine spongiform encephalopathy agents. Proceedings of the National Academy of Sciences 96(7):4046–4051

[30] Prusiner SB, Hadlow WJ (1979) Slow Transmissible Diseases of the Nervous System: Clinical, Epidemiological, Genetic and Pathological Aspects of the Spongiform Encephalopathie. Academic Press Inc

[31] Brown P, Preece M, Brandel JP, Sato T, McShane L, Zerr I, Fletcher A, Will R, Pocchiari M, Cashman N, et al. (2000) Iatrogenic creutzfeldt–jakob disease at the millennium. Neurology 55(8):1075–1081

[32] Willbold D, Strodel B, Schröder GF, Hoyer W, Heise H (2021) Amyloid-type protein aggregation and prion-like properties of amyloids. Chemical Reviews 121(13):8285–8307, DOI 10.1021/acs.chemrev.1c00196

[33] Wadsworth JD, Joiner S, Linehan JM, Desbruslais M, Fox K, Cooper S, Cronier S, Asante EA, Mead S, Brandner S, et al. (2008) Kuru prions and sporadic creutzfeldt–jakob disease prions have equivalent transmission properties in transgenic and wild-type mice. Proceedings of the National Academy of Sciences 105(10):3885–3890

[34] Hosszu LL, Conners R, Sangar D, Batchelor M, Sawyer EB, Fisher S, Cliff MJ, Hounslow AM, McAuley K, Leo Brady R, et al. (2020) Structural effects of the highly protective v127 polymorphism on human prion protein. Communications biology 3(1):1–12

[35] Hosszu LL, Jackson GS, Trevitt CR, Jones S, Batchelor M, Bhelt D, Prodromidou K, Clarke AR, Waltho JP, Collinge J (2004) The residue 129 polymorphism in human prion protein does not confer susceptibility to creutzfeldt-jakob disease by altering the structure or global stability of prpc. Journal of Biological Chemistry 279(27):28515–28521

[36] Prusiner SB (1989) Creutzfeldt-jakob disease and scrapie prions. Alzheimer disease and associated disorders 3(1-2):52–78

[37] Brown P, Cathala F, Raubertas R, Gajdusek D, Castaigne P (1987) The epidemiology of creutzfeldt-jakob disease: conclusion of a 15-year investigation in france and review of the world literature. Neurology 37(6):895–895

[38] Malmgren R (1979) The epidemiology of creufzfeldt-jakob disase. Slow transmissible diseases of the nervous system 1:93–112

[39] Mead S (2006) Prion disease genetics. European Journal of Human Genetics 14(3):273–281

[40] Young K, Clark HB, Piccardo P, Dlouhy SR, Ghetti B (1997) Gerstmann–sträussler–scheinker disease with the prnp p102l mutation and valine at codon 129. Molecular brain research 44(1):147–150

[41] Hainfellner JA, Brantner-Inthaler S, Cervenáková L, Brown P, Kitamoto T, Tateishi J, Diringer H, Liberski PP, Regele H, Feucht M, et al. (1995) The original gerstmann-sträussler-scheinker family of austria: divergent clinicopathological phenotypes but constant prp genotype. Brain Pathology 5(3):201–211

[42] Lugaresi E, Medori R, Montagna P, Baruzzi A, Cortelli P, Lugaresi A, Tinuper P, Zucconi M, Gambetti P (1986) Fatal familial insomnia and dysautonomia with selective degeneration of thalamic nuclei. New England Journal of Medicine 315(16):997–1003

[43] Brown P, Cervenáková L, Boellaard J, Stavrou D, Goldfarb L, Gajdusek DC (1994) Identification of a prnp gene mutation in jakob's original creutzfeldt-jakob disease family. The Lancet 344(8915):130–131

[44] Goldfarb LG, Petersen RB, Tabaton M, Brown P, LeBlanc AC, Montagna P, Cortelli P, Julien J, Vital C, Pendelbury WW, et al. (1992) Fatal familial insomnia and familial creutzfeldt-jakob disease: disease phenotype determined by a dna polymorphism. Science 258(5083):806–808

[45] Zeidler M, Stewart G, Cousens S, Estibeiro K, Will R (1997) Codon 129 genotype and new variant cjd. The Lancet 350(9078):668

[46] Hill A, Butterworth R, Joiner S, Jackson G, Rossor M, Thomas D, Frosh A, Tolley N, Bell J, Spencer M, et al. (1999) Investigation of variant creutzfeldt-jakob disease and other human prion diseases with tonsil biopsy samples. The Lancet 353(9148):183–189

[47] Poulter M, Baker H, Frith C, Leach M, Lofthouse R, Ridley R, Shah T, Owen F, Collinge J, Brown J, et al. (1992) Inherited prion disease with 144 base pair gene insertion: 1. genealogical and molecular studies. Brain 115(3):675–685

[48] Collinge J, Palmer MS, Dryden A (1991) Genetic predisposition to iatrogenic creutzfeldt-jakob disease. The Lancet 337(8755):1441–1442

[49] Cobb NJ, Surewicz WK (2009) Prion diseases and their biochemical mechanisms. Biochemistry 48(12):2574–2585

[50] Sparkes RS, Simon M, Cohn VH, Fournier R, Lem J, Klisak I, Heinzmann C, Blatt C, Lucero M, Mohandas T (1986) Assignment of the human and mouse prion protein genes to homologous chromosomes. Proceedings of the National Academy of Sciences 83(19):7358–7362

[51] Harris DA (1999) Cellular biology of prion diseases. Clinical microbiology reviews 12(3):429–444

[52] Zahn R, Liu A, Lührs T, Riek R, Schroetter Cv, García FL, Billeter M, Calzolai L, Wider G, Wüthrich K (2000) Nmr solution structure of the human prion protein. Proceedings of the National Academy of Sciences 97(1):145–150, DOI 10.1073/pnas.97.1.145

[53] Kim SJ, Rahbar R, Hegde RS (2001) Combinatorial control of prion protein biogenesis by the signal sequence and transmembrane domain. Journal of Biological Chemistry 276(28):26132–26140

[54] Wang LQ, Zhao K, Yuan HY, Wang Q, Guan Z, Tao J, Li XN, Sun Y, Yi CW, Chen J, Li D, Zhang D, Yin P, Liu C, Liang Y (2020) Cryo-em structure of an amyloid fibril formed by full-length human prion protein. Nature Structural & Molecular Biology 27(6):598–602, DOI 10.1038/s41594-020-0441-5

[55] Kraus A, Hoyt F, Schwartz CL, Hansen B, Artikis E, Hughson AG, Raymond GJ, Race B, Baron GS, Caughey B (2021) High-resolution structure and strain comparison of infectious mammalian prions. Molecular Cell 81(21):4540–4551

[56] Kovač V, Čurin Šerbec V (2022) Prion protein: The molecule of many forms and faces. International Journal of Molecular Sciences 23(3):1232

[57] Vincent B, Paitel E, Saftig P, Frobert Y, Hartmann D, De Strooper B, Grassi J, Lopez-Perez E, Checler F (2001) The disintegrins adam10 and tace contribute to the constitutive and phorbol ester-regulated normal cleavage of the cellular prion protein. Journal of Biological Chemistry 276(41):37743–37746

[58] Laffont-Proust I, Faucheux BA, Hässig R, Sazdovitch V, Simon S, Grassi J, Hauw JJ, Moya KL, Haïk S (2005) The n-terminal cleavage of cellular prion protein in the human brain. FEBS letters 579(28):6333–6337

[59] Laurén J, Gimbel DA, Nygaard HB, Gilbert JW, Strittmatter SM (2009) Cellular prion protein mediates impairment of synaptic plasticity by amyloid-β oligomers. Nature 457(7233):1128–1132

[60] Chen S, Yadav SP, Surewicz WK (2010) Interaction between human prion protein and amyloid-β (aβ) oligomers: role of n-terminal residues. Journal of Biological Chemistry 285(34):26377–26383

[61] Lewis V, Johanssen VA, Crouch PJ, Klug GM, Hooper NM, Collins SJ (2016) Prion protein "gamma-cleavage": characterizing a novel endoproteolytic processing event. Cellular and Molecular Life Sciences 73(3):667–683

[62] Um JW, Kaufman AC, Kostylev M, Heiss JK, Stagi M, Takahashi H, Kerrisk ME, Vortmeyer A, Wisniewski T, Koleske AJ, et al. (2013) Metabotropic glutamate receptor 5 is a coreceptor for alzheimer aβ oligomer bound to cellular prion protein. Neuron 79(5):887–902

[63] McDonald AJ, Dibble JP, Evans EG, Millhauser GL (2014) A new paradigm for enzymatic control of α-cleavage and β-cleavage of the prion protein. Journal of Biological Chemistry 289(2):803–813

[64] Lewis V, Hill AF, Haigh CL, Klug GM, Masters CL, Lawson VA, Collins SJ (2009) Increased proportions of c1 truncated prion protein protect against cellular m1000 prion infection. Journal of Neuropathology & Experimental Neurology 68(10):1125–1135

[65] Westergard L, Turnbaugh JA, Harris DA (2011) A naturally occurring c-terminal fragment of the prion protein (prp) delays disease and acts as a dominant-negative inhibitor of prpsc formation. Journal of Biological Chemistry 286(51):44234–44242

[66] Watt NT, Taylor DR, Gillott A, Thomas DA, Perera WSS, Hooper NM (2005) Reactive oxygen species-mediated β-cleavage of the prion protein in the cellular response to oxidative stress. Journal of Biological Chemistry 280(43):35914–35921

[67] Linsenmeier L, Mohammadi B, Shafiq M, Frontzek K, Bär J, Shrivastava AN, Damme M, Song F, Schwarz A, Da Vela S, et al. (2021) Ligands binding to the prion protein induce its proteolytic release with therapeutic potential in neurodegenerative proteinopathies. Science advances 7(48):eabj1826

[68] Küffer A, Lakkaraju AK, Mogha A, Petersen SC, Airich K, Doucerain C, Marpakwar R, Bakirci P, Senatore A, Monnard A, et al. (2016) The prion protein is an agonistic ligand of the g protein-coupled receptor adgrg6. Nature 536(7617):464–468

[69] Collins S, McLean C, Masters C (2001) Gerstmann–sträussler–scheinker syndrome, fatal familial insomnia, and kuru: a review ofthese less common human transmissiblespongiform encephalopathies. Journal of Clinical Neuroscience 8(5):387–397

[70] Gasperini L, Meneghetti E, Pastore B, Benetti F, Legname G (2015) Prion protein and copper cooperatively protect neurons by modulating nmda receptor through s-nitrosylation. Antioxidants & redox signaling 22(9):772–784

[71] Cingaram PKR, Nyeste A, Dondapati DT, Fodor E, Welker E (2015) Prion protein does not confer resistance to hippocampus-derived zpl cells against the toxic effects of cu2+, mn2+, zn2+ and co2+ not supporting a general protective role for prp in transition metal induced toxicity. PLoS one 10(10):e0139219

[72] Ikezawa H (2002) Glycosylphosphatidylinositol (gpi)-anchored proteins. Biological and pharmaceutical bulletin 25(4):409–417

[73] Yoshitake H, Araki Y (2020) Role of the glycosylphosphatidylinositol-anchored protein tex101 and its related molecules in spermatogenesis. International Journal of Molecular Sciences 21(18):6628

[74] Simons K, Ikonen E (1997) Functional rafts in cell membranes. nature 387(6633):569–572

[75] Taylor DR, Hooper NM (2006) The prion protein and lipid rafts. Molecular membrane biology 23(1):89–99

[76] Stahl N, Baldwin M, Hecker R, Pan KM, Burlingame A, Prusiner S (1992) Glycosylinositol phospholipid anchors of the scrapie and cellular prion proteins contain sialic acid. Biochemistry 31(21):5043–5053

[77] Stahl N, Borchelt DR, Prusiner SB (1990) Differential release of cellular and scrapie prion proteins from cellular membranes by phosphatidylinositol-specific phospholipase c. Biochemistry 29(22):5405–5412

[78] Chesebro B, Trifilo M, Race R, Meade-White K, Teng C, LaCasse R, Raymond L, Favara C, Baron G, Priola S, et al. (2005) Anchorless prion protein results in infectious amyloid disease without clinical scrapie. Science 308(5727):1435–1439

[79] Taraboulos A, Scott M, Semenov A, Avrahami D, Laszlo L, Prusiner SB, Avraham D (1995) Cholesterol depletion and modification of cooh-terminal targeting sequence of the prion protein inhibit formation of the scrapie isoform. The Journal of cell biology 129(1):121–132

[80] Baron GS, Wehrly K, Dorward DW, Chesebro B, Caughey B (2002) Conversion of raft associated prion protein to the protease-resistant state requires insertion of prp-res (prpsc) into contiguous membranes. The EMBO journal 21(5):1031–1040

[81] Baron GS, Caughey B (2003) Effect of glycosylphosphatidylinositol anchor-dependent and-independent prion protein association with model raft membranes on conversion to the protease-resistant isoform. Journal of Biological Chemistry 278(17):14883–14892

[82] Kaneko K, Vey M, Scott M, Pilkuhn S, Cohen FE, Prusiner SB (1997) Cooh-terminal sequence of the cellular prion protein directs subcellular trafficking and controls conversion into the scrapie isoform. Proceedings of the National Academy of Sciences 94(6):2333–2338

[83] Aebi M (2013) N-linked protein glycosylation in the er. Biochimica et Biophysica Acta (BBA)-Molecular Cell Research 1833(11):2430–2437

[84] Breitling J, Aebi M (2013) N-linked protein glycosylation in the endoplasmic reticulum. Cold Spring Harbor perspectives in biology 5(8):a013359

[85] Spiro RG (2002) Protein glycosylation: nature, distribution, enzymatic formation, and disease implications of glycopeptide bonds. Glycobiology 12(4):43R–56R

[86] Imperiali B, O'Connor SE (1999) Effect of n-linked glycosylation on glycopeptide and glycoprotein structure. Current opinion in chemical biology 3(6):643–649

[87] Patterson MC (2005) Metabolic mimics: the disorders of n-linked glycosylation. In: Seminars in pediatric neurology, Elsevier, vol 12, pp 144–151

[88] Lai JY, Klatt S, Lim TS (2019) Potential application of leishmania tarentolae as an alternative platform for antibody expression. Critical reviews in biotechnology 39(3):380–394

[89] Jefferis R (2017) Recombinant proteins and monoclonal antibodies. Advances in Glycobiotechnology pp 281–318

[90] Taylor ME, Drickamer K (2011) Introduction to glycobiology. Oxford university press

[91] Guo S, Skala W, Magdolen V, Brandstetter H, Goettig P (2014) Sweetened kallikrein-related peptidases (klks): glycan trees as potential regulators of activation and activity. Biological chemistry 395(9):959–976

[92] Haraguchi T, Fisher S, Olofsson S, Endo T, Groth D, Tarentino A, Borchelt DR, Teplow D, Hood L, Burlingame A, et al. (1989) Asparagine-linked glycosylation of the scrapie and cellular prion proteins. Archives of biochemistry and biophysics 274(1):1–13

[93] Wiseman FK, Cancellotti E, Piccardo P, Iremonger K, Boyle A, Brown D, Ironside JW, Manson JC, Diack AB (2015) The glycosylation status of prpc is a key factor in determining transmissible spongiform encephalopathy transmission between species. Journal of virology 89(9):4738–4747

[94] Katorcha E, Makarava N, Savtchenko R, d' Azzo A, Baskakov IV (2014) Sialylation of prion protein controls the rate of prion amplification, the cross-species barrier, the ratio of prpsc glycoform and prion infectivity. PLoS pathogens 10(9):e1004366

[95] Camacho MV, Telling G, Kong Q, Gambetti P, Notari S (2019) Role of prion protein glycosylation in replication of human prions by protein misfolding cyclic amplification. Laboratory Investigation 99(11):1741–1748

[96] Lehmann S, Harris DA (1997) Blockade of glycosylation promotes acquistion of scrapie-like properties by the prion protein in cultured cells. Journal of Biological Chemistry 272(34):21479–21487

[97] Taraboulos A, Rogers M, Borchelt DR, McKinley MP, Scott M, Serban D, Prusiner SB (1990) Acquisition of protease resistance by prion proteins in scrapie-infected cells does not require asparagine-linked glycosylation. Proceedings of the National Academy of Sciences 87(21):8262–8266

[98] Bosques CJ, Imperiali B (2003) The interplay of glycosylation and disulfide formation influences fibrillization in a prion protein fragment. Proceedings of the National Academy of Sciences 100(13):7593–7598

[99] Lawson VA, Collins SJ, Masters CL, Hill AF (2005) Prion protein glycosylation. Journal of neurochemistry 93(4):793–801

[100] Walmsley AR, Zeng F, Hooper NM (2001) Membrane topology influences n-glycosylation of the prion protein. The EMBO Journal 20(4):703–712

[101] Sipe JD, Cohen AS (2000) History of the amyloid fibril. Journal of structural biology 130(2-3):88–98

[102] Benditt E, Eriksen N, Hermodson M, Ericsson L (1971) The major proteins of human and monkey amyloid substance: common properties including unusual n-terminal amino acid sequences. FEBS letters 19(2):169–173

[103] Costa PP, Figueira AS, Bravo FR (1978) Amyloid fibril protein related to prealbumin in familial amyloidotic polyneuropathy. Proceedings of the National Academy of Sciences 75(9):4499–4503

[104] Iadanza MG, Jackson MP, Hewitt EW, Ranson NA, Radford SE (2018) A new era for understanding amyloid structures and disease. Nature Reviews Molecular Cell Biology 19(12):755–773

[105] Shirahama T, Cohen AS (1967) High-resolution electron microscopic analysis of the amyloid fibril. The Journal of cell biology 33(3):679–708

[106] Serpell LC, Sunde M, Benson MD, Tennent GA, Pepys MB, Fraser PE (2000) The protofilament substructure of amyloid fibrils. Journal of molecular biology 300(5):1033–1039

[107] Gremer L, Schölzel D, Schenk C, Reinartz E, Labahn J, Ravelli RB, Tusche M, Lopez-Iglesias C, Hoyer W, Heise H, et al. (2017) Fibril structure of amyloid-β (1–42) by cryo-electron microscopy. Science 358(6359):116–119

[108] Virchow R (1855) Zur cellulose-frage. Archiv für pathologische Anatomie und Physiologie und für klinische Medicin 8(1):140–144

[109] Friedreich N, Kekulé A (1859) Zur amyloidfrage. Archiv für pathologische Anatomie und Physiologie und für klinische Medicin 16(1):50–65

[110] Alzheimer A (1906) Uber einen eigenartigen schweren er krankungsprozeb der hirnrinde. Neurologisches Centralblatt 23:1129–1136

[111] Alzheimer A (1907) Uber eine eigenartige erkrankung der hirnrinde. Zentralbl Nervenh Psych 18:177–179

[112] Divry P (1934) De la nature de l'altération fibrillaire d'alzheimer. J Belge Neurol Psych 34:197–201

[113] Bennhold H (1922) Eine spezifische amyloidfarbung wit kongorot. Meunch Med Wocheschr 69:1537–1538

[114] Missmahl HP, Hartwig M (1953) Polarisationsoptische untersuchungen an der amyloidsubstanz. Virchows Archiv für pathologische Anatomie und Physiologie und für klinische Medizin 324(4):489–508

[115] Cohen AS, Calkins E (1959) Electron microscopic observations on a fibrous component in amyloid of diverse origins. Nature 183(4669):1202–1203

[116] Eanes E, Glenner G (1968) X-ray diffraction studies on amyloid filaments. Journal of Histochemistry & Cytochemistry 16(11):673–677

[117] Naiki H, Higuchi K, Hosokawa M, Takeda T (1989) Fluorometric determination of amyloid fibrils in vitro using the fluorescent dye, thioflavine t. Analytical biochemistry 177(2):244–249

[118] Khurana R, Coleman C, Ionescu-Zanetti C, Carter SA, Krishna V, Grover RK, Roy R, Singh S (2005) Mechanism of thioflavin t binding to amyloid fibrils. Journal of structural biology 151(3):229–238

[119] Biancalana M, Koide S (2010) Molecular mechanism of thioflavin-t binding to amyloid fibrils. Biochimica et Biophysica Acta (BBA)-Proteins and Proteomics 1804(7):1405–1412

[120] Linse S (2019) Mechanism of amyloid protein aggregation and the role of inhibitors. Pure and Applied Chemistry 91(2):211–229

[121] Almeida ZL, Brito RMM (2020) Structure and aggregation mechanisms in amyloids. Molecules 25(5):1195, DOI 10.3390/molecules25051195

[122] O'Nuallain B, Shivaprasad S, Kheterpal I, Wetzel R (2005) Thermodynamics of aβ (1- 40) amyloid fibril elongation. Biochemistry 44(38):12709–12718

[123] Jarrett JT, Lansbury Jr PT (1993) Seeding "one-dimensional crystallization" of amyloid: a pathogenic mechanism in alzheimer's disease and scrapie? Cell 73(6):1055–1058

[124] Michaels TC, Šarić A, Habchi J, Chia S, Meisl G, Vendruscolo M, Dobson CM, Knowles TP (2018) Chemical kinetics for bridging molecular mechanisms and macroscopic measurements of amyloid fibril formation. Annual review of physical chemistry 69:273–298

[125] Arosio P, Knowles TPJ, Linse S (2015) On the lag phase in amyloid fibril formation. Physical Chemistry Chemical Physics 17(12):7606–7618, DOI 10.1039/c4cp05563b

[126] Šarić A, Chebaro YC, Knowles TP, Frenkel D (2014) Crucial role of nonspecific interactions in amyloid nucleation. Proceedings of the National Academy of Sciences 111(50):17869–17874

[127] Verma M, Vats A, Taneja V (2015) Toxic species in amyloid disorders: Oligomers or mature fibrils. Annals of Indian Academy of Neurology 18(2):138

[128] Milanesi L, Sheynis T, Xue WF, Orlova EV, Hellewell AL, Jelinek R, Hewitt EW, Radford SE, Saibil HR (2012) Direct three-dimensional visualization of membrane disruption by amyloid fibrils. Proceedings of the National Academy of Sciences 109(50):20455–20460

[129] Evangelisti E, Cascella R, Becatti M, Marrazza G, Dobson CM, Chiti F, Stefani M, Cecchi C (2016) Binding affinity of amyloid oligomers to cellular membranes is a generic indicator of cellular dysfunction in protein misfolding diseases. Scientific reports 6(1):1–14

[130] Conway KA, Lee SJ, Rochet JC, Ding TT, Williamson RE, Lansbury Jr PT (2000) Acceleration of oligomerization, not fibrillization, is a shared property of both α-synuclein mutations linked to early-onset parkinson's disease: implications for pathogenesis and therapy. Proceedings of the National Academy of Sciences 97(2):571–576

[131] Cleary JP, Walsh DM, Hofmeister JJ, Shankar GM, Kuskowski MA, Selkoe DJ, Ashe KH (2005) Natural oligomers of the amyloid-β protein specifically disrupt cognitive function. Nature neuroscience 8(1):79–84

[132] Winner B, Jappelli R, Maji SK, Desplats PA, Boyer L, Aigner S, Hetzer C, Loher T, Vilar M, Campioni S, et al. (2011) In vivo demonstration that α-synuclein oligomers are toxic. Proceedings of the National Academy of Sciences 108(10):4194–4199

[133] Sengupta U, Nilson AN, Kayed R (2016) The role of amyloid-β oligomers in toxicity, propagation, and immunotherapy. EBioMedicine 6:42–49

[134] Eva Ž (2002) Amyloid-fibril formation: Proposed mechanisms and relevance to conformational disease. European Journal of Biochemistry 269(14):3362–3371

[135] Uversky VN, Fink AL (2004) Conformational constraints for amyloid fibrillation: the importance of being unfolded. Biochimica et Biophysica Acta (BBA)-Proteins and Proteomics 1698(2):131–153

[136] Colvin MT, Silvers R, Frohm B, Su Y, Linse S, Griffin RG (2015) High resolution structural characterization of aβ42 amyloid fibrils by magic angle spinning nmr. Journal of the American Chemical Society 137(23):7509–7518

[137] Heise H, Hoyer W, Becker S, Andronesi OC, Riedel D, Baldus M (2005) Molecular-level secondary structure, polymorphism, and dynamics of full-length α-synuclein fibrils studied by solid-state nmr. Proceedings of the National Academy of Sciences 102(44):15871–15876

[138] Fändrich M, Meinhardt J, Grigorieff N (2009) Structural polymorphism of alzheimer aβ and other amyloid fibrils. Prion 3(2):89–93

[139] Roeder C, Kupreichyk T, Gremer L, Schäfer LU, Pothula KR, Ravelli RB, Willbold D, Hoyer W, Schröder GF (2020) Cryo-em structure of islet amyloid polypeptide fibrils reveals similarities with amyloid-β fibrils. Nature Structural & Molecular Biology 27(7):660–667

[140] Röder C, Vettore N, Mangels LN, Gremer L, Ravelli RB, Willbold D, Hoyer W, Buell AK, Schröder GF (2019) Atomic structure of pi3-kinase sh3 amyloid fibrils by cryo-electron microscopy. Nature communications 10(1):1–9

[141] Chiti F, Dobson CM, et al. (2006) Protein misfolding, functional amyloid, and human disease. Annual review of biochemistry 75(1):333–366

[142] Chapman MR, Robinson LS, Pinkner JS, Roth R, Heuser J, Hammar M, Normark S, Hultgren SJ (2002) Role of escherichia coli curli operons in directing amyloid fiber formation. Science 295(5556):851–855

[143] Patterson BW, Elbert DL, Mawuenyega KG, Kasten T, Ovod V, Ma S, Xiong C, Chott R, Yarasheski K, Sigurdson W, et al. (2015) Age and amyloid effects on human central nervous system amyloid-beta kinetics. Annals of neurology 78:439–453

[144] Meyne F, Gloeckner SF, Ciesielczyk B, Heinemann U, Krasnianski A, Meissner B, Zerr I (2009) Total prion protein levels in the cerebrospinal fluid are reduced in patients with various neurological disorders. Journal of Alzheimer's Disease 17(4):863–873

[145] Jack K, Jackson GS, Bieschke J (2022) Essential components of synthetic infectious prion formation de novo. Biomolecules 12(11):1694

[146] Corsellis J (1989) Boxing and the brain. BMJ: British Medical Journal 298(6666):105

[147] Murphy MP, LeVine III H (2010) Alzheimer's disease and the amyloid-β peptide. Journal of Alzheimer's disease 19(1):311–323

[148] Lane CA, Hardy J, Schott JM (2018) Alzheimer's disease. European journal of neurology 25(1):59–70

[149] Scheltens P, De Strooper B, Kivipelto M, Holstege H, Chételat G, Teunissen CE, Cummings J, van der Flier WM (2021) Alzheimer's disease. The Lancet 397(10284):1577–1590

[150] Patterson C (2018) World alzheimer report 2018. Alzheimer's Disease International

[151] Hebert LE, Scherr PA, Beckett LA, Albert MS, Pilgrim DM, Chown MJ, Funkenstein HH, Evans DA (1995) Age-specific incidence of alzheimer's disease in a community population. Jama 273(17):1354–1359

[152] Sloane PD, Zimmerman S, Suchindran C, Reed P, Wang L, Boustani M, Sudha S (2002) The public health impact of alzheimer's disease, 2000–2050: potential implication of treatment advances. Annual review of public health 23(1):213–231

[153] Goedert M, Spillantini MG (2006) A century of alzheimer's disease. science 314(5800):777–781

[154] Elfgen A, Hupert M, Bochinsky K, Tusche M, González de San Román Martin E, Gering I, Sacchi S, Pollegioni L, Huesgen PF, Hartmann R, et al. (2019) Metabolic resistance of the d-peptide rd2 developed for direct elimination of amyloid-β oligomers. Scientific reports 9(1):1–13

[155] Elfgen A, Santiago-Schübel B, Gremer L, Kutzsche J, Willbold D (2017) Surprisingly high stability of the aβ oligomer eliminating all-d-enantiomeric peptide d3 in media simulating the route of orally administered drugs. European journal of pharmaceutical sciences 107:203–207

[156] Uppalapati M, Lee DJ, Mandal K, Li H, Miranda LP, Lowitz J, Kenney J, Adams JJ, Ault-Riché D, Kent SB, et al. (2016) A potent d-protein antagonist of vegf-a is nonimmunogenic, metabolically stable, and longer-circulating in vivo. ACS chemical biology 11(4):1058–1065

[157] Wiesehan K, Buder K, Linke RP, Patt S, Stoldt M, Unger E, Schmitt B, Bucci E, Willbold D (2003) Selection of d-amino-acid peptides that bind to alzheimer's disease amyloid peptide aβ1–42 by mirror image phage display. Chembiochem 4(8):748–753

[158] Van Groen T, Wiesehan K, Funke SA, Kadish I, Nagel-Steger L, Willbold D (2008) Reduction of alzheimer's disease amyloid plaque load in transgenic mice by d3, ad-enantiomeric peptide identified by mirror image phage display. ChemMedChem: Chemistry Enabling Drug Discovery 3(12):1848–1852

[159] Brener O, Dunkelmann T, Gremer L, Van Groen T, Mirecka EA, Kadish I, Willuweit A, Kutzsche J, Jürgens D, Rudolph S, et al. (2015) Qiad assay for quantitating a compound's efficacy in elimination of toxic aβ oligomers. Scientific reports 5(1):1–13

[160] Funke SA, van Groen T, Kadish I, Bartnik D, Nagel-Steger L, Brener O, Sehl T, Batra-Safferling R, Moriscot C, Schoehn G, et al. (2010) Oral treatment with the d-enantiomeric peptide d3 improves the pathology and behavior of alzheimer's disease transgenic mice. ACS chemical neuroscience 1(9):639–648

[161] Wiesehan K, Stöhr J, Nagel-Steger L, Van Groen T, Riesner D, Willbold D (2008) Inhibition of cytotoxicity and amyloid fibril formation by a d-amino acid peptide that specifically binds to alzheimer's disease amyloid peptide. Protein Engineering, Design & Selection 21(4):241–246

[162] Chen Gf, Xu Th, Yan Y, Zhou Yr, Jiang Y, Melcher K, Xu HE (2017) Amyloid beta: structure, biology and structure-based therapeutic development. Acta Pharmacologica Sinica 38(9):1205–1235

[163] Johansson AS, Bergquist J, Volbracht C, Päiviö A, Leist M, Lannfelt L, Westlind-Danielsson A (2007) Attenuated amyloid-β aggregation and neurotoxicity owing to methionine oxidation. Neuroreport 18(6):559–563

[164] El-Agnaf OM, Mahil DS, Patel BP, Austen BM (2000) Oligomerization and toxicity of β-amyloid-42 implicated in alzheimer's disease. Biochemical and biophysical research communications 273(3):1003–1007

[165] Priller C, Bauer T, Mitteregger G, Krebs B, Kretzschmar HA, Herms J (2006) Synapse formation and function is modulated by the amyloid precursor protein. Journal of Neuroscience 26(27):7212–7221

[166] Duce JA, Tsatsanis A, Cater MA, James SA, Robb E, Wikhe K, Leong SL, Perez K, Johanssen T, Greenough MA, et al. (2010) Iron-export ferroxidase activity of β-amyloid precursor protein is inhibited by zinc in alzheimer's disease. Cell 142(6):857–867

[167] Haass C, Kaether C, Thinakaran G, Sisodia S (2012) Trafficking and proteolytic processing of app. Cold Spring Harbor perspectives in medicine 2(5):a006270

[168] Spies PE, Verbeek MM, van Groen T, Claassen JA (2012) Reviewing reasons for the decreased csf abeta42 concentration in alzheimer disease. Frontiers in Bioscience

[169] Selkoe DJ (2001) Alzheimer's disease: genes, proteins, and therapy. Physiological reviews

[170] Puzzo D, Arancio O (2013) Amyloid-β peptide: Dr. jekyll or mr. hyde? Journal of Alzheimer's Disease 33(s1):S111–S120

[171] Cheignon C, Tomas M, Bonnefont-Rousselot D, Faller P, Hureau C, Collin F (2018) Oxidative stress and the amyloid beta peptide in alzheimer's disease. Redox biology 14:450–464

[172] Perrett S, Ma J, Wang F (2014) Prion disease and the 'protein-only hypothesis'. Essays in biochemistry 56:181–191

[173] Schwarzman A, Senkevich K, Emelyanov A, Pchelina S (2019) Prion properties of alpha-synuclein. Molecular Biology 53(3):335–341

[174] Stuart K (1991) Rna editing in trypanosomatid mitochondria. Annual review of microbiology 45(1):327–344

[175] Breitling R, Klingner S, Callewaert N, Pietrucha R, Geyer A, Ehrlich G, Hartung R, Müller A, Contreras R, Beverley SM, et al. (2002) Non-pathogenic trypanosomatid protozoa as a platform for protein research and production. Protein expression and purification 25(2):209–218

[176] Raymond F, Boisvert S, Roy G, Ritt JF, Legare D, Isnard A, Stanke M, Olivier M, Tremblay MJ, Papadopoulou B, et al. (2012) Genome sequencing of the lizard parasite leishmania tarentolae reveals loss of genes associated to the intracellular stage of human pathogenic species. Nucleic acids research 40(3):1131–1147

[177] Klatt S, Rohe M, Alagesan K, Kolarich D, Konthur Z, Hartl D (2013) Production of glycosylated soluble amyloid precursor protein alpha (sappalpha) in leishmania tarentolae. Journal of proteome research 12(1):396–403

[178] Parodi AJ (1993) N-glycosylation in trypanosomatid protozoa. Glycobiology 3(3):193–199

[179] Krakow JL, Hereld D, Bangs J, Hart G, Englund P (1986) Identification of a glycolipid precursor of the trypanosoma brucei variant surface glycoprotein. Journal of Biological Chemistry 261(26):12147–12153

[180] Basile G, Peticca M (2009) Recombinant protein expression in leishmania tarentolae. Molecular biotechnology 43(3):273–278

[181] Khan AH, Bayat H, Rajabibazl M, Sabri S, Rahimpour A (2017) Humanizing glycosylation pathways in eukaryotic expression systems. World Journal of Microbiology and Biotechnology 33(1):1–12

[182] Schenkman S, Eichinger D, Pereira M, Nussenzweig V (1994) Structural and functional properties of trypanosoma trans-sialidase. Annual review of microbiology 48:499–524

[183] Pereira ME (1983) A developmentally regulated neuraminidase activity in trypanosoma cruzi. Science 219(4591):1444–1446

[184] Roth J, Zuber C, Park S, Jang I, Lee Y, Kysela KG, Le Fourn V, Santimaria R, Guhl B, Cho JW (2010) Protein n-glycosylation, protein folding, and protein quality control. Molecules and cells 30(6):497–506

[185] de Oliveira TA, da Silva W, da Rocha Torres N, de Moraes JVB, Senra RL, de Oliveira Mendes TA, Júnior AS, Bressan GC, Fietto JLR (2019) Application of the lexsy leishmania tarentolae system as a recombinant protein expression platform: A review. Process Biochemistry 87:164–173

[186] Kushnir S, Gase K, Breitling R, Alexandrov K (2005) Development of an inducible protein expression system based on the protozoan host leishmania tarentolae. Protein expression and purification 42(1):37–46

[187] Pan KM, Baldwin M, Nguyen J, Gasset M, Serban A, Groth D, Mehlhorn I, Huang Z, Fletterick RJ, Cohen FE (1993) Conversion of alpha-helices into beta-sheets features in the formation of the scrapie prion proteins. Proceedings of the National Academy of Sciences 90(23):10962–10966

[188] Safar J, Roller PP, Gajdusek DC, Gibbs Jr CJ (1993) Thermal stability and conformational transitions of scrapie amyloid (prion) protein correlate with infectivity. Protein Science 2(12):2206–2216

[189] Prusiner SB (1982) Novel proteinaceous infectious particles cause scrapie. Science 216(4542):136–144

[190] Palmer MS, Dryden AJ, Hughes JT, Collinge J (1991) Homozygous prion protein genotype predisposes to sporadic creutzfeldt–jakob disease. Nature 352(6333):340–342

[191] Baker H, Poulter M, Crow T, Frith C, Lofthouse R, Ridley R, Collinge J (1991) Aminoacid polymorphism in human prion protein and age at death in inherited prion disease. The Lancet 337(8752):1286, DOI https://doi.org/10.1016/0140-6736(91)92953-Y, URL https://www.sciencedirect.com/science/article/pii/014067369192953Y, originally published as Volume 1, Issue 8752

[192] Baiardi S, Rossi M, Mammana A, Appleby BS, Barria MA, Calì I, Gambetti P, Gelpi E, Giese A, Ghetti B, et al. (2021) Phenotypic diversity of genetic creutzfeldt–jakob disease: A histo-molecular-based classification. Acta neuropathologica 142(4):707–728

[193] Brown K, Mastrianni JA (2010) The prion diseases. Journal of geriatric psychiatry and neurology 23(4):277–298

[194] Barducci A, Chelli R, Procacci P, Schettino V, Gervasio FL, Parrinello M (2006) Metadynamics simulation of prion protein: β-structure stability and the early stages of misfolding. Journal of the American Chemical Society 128(8):2705–2710

[195] Hosszu LL, Wells MA, Jackson GS, Jones S, Batchelor M, Clarke AR, Craven CJ, Waltho JP, Collinge J (2005) Definable equilibrium states in the folding of human prion protein. Biochemistry 44(50):16649–16657

[196] Gerum C, Silvers R, Wirmer-Bartoschek J, Schwalbe H (2009) Unfolded-state structure and dynamics influence the fibril formation of human prion protein. Angewandte Chemie 121(50):9616–9620

[197] Ziaunys M, Sneideris T, Smirnovas V (2020) Formation of distinct prion protein amyloid fibrils under identical experimental conditions. Scientific reports 10(1):1–7

[198] Torrent J, Martin D, Noinville S, Yin Y, Doumic M, Moudjou M, Beringue V, Rezaei H (2019) Pressure reveals unique conformational features in prion protein fibril diversity. Scientific reports 9(1):1–11

[199] Hosszu LL, Trevitt CR, Jones S, Batchelor M, Scott DJ, Jackson GS, Collinge J, Waltho JP, Clarke AR (2009) Conformational properties of β-prp. Journal of Biological Chemistry 284(33):21981–21990

[200] Greenfield NJ (2006) Using circular dichroism spectra to estimate protein secondary structure. Nature protocols 1(6):2876–2890

[201] Pfleger C, Rathi PC, Klein DL, Radestock S, Gohlke H (2013) Constraint network analysis (cna): a python software package for efficiently linking biomacromolecular structure, flexibility,(thermo-) stability, and function

[202] Rathi PC, Jaeger KE, Gohlke H (2015) Structural rigidity and protein thermostability in variants of lipase a from bacillus subtilis. PloS one 10(7):e0130289

[203] Hermans SM, Pfleger C, Nutschel C, Hanke CA, Gohlke H (2017) Rigidity theory for biomolecules: concepts, software, and applications. Wiley Interdisciplinary Reviews: Computational Molecular Science 7(4):e1311

[204] Valley CC, Cembran A, Perlmutter JD, Lewis AK, Labello NP, Gao J, Sachs JN (2012) The methionine-aromatic motif plays a unique role in stabilizing protein structure. Journal of Biological Chemistry 287(42):34979–34991

[205] Lee J, Chang I (2019) Structural insight into conformational change in prion protein by breakage of electrostatic network around h187 due to its protonation. Scientific reports 9(1):1–11

[206] Zhou S, Shi D, Liu X, Yao X, Da LT, Liu H (2019) ph-induced misfolding mechanism of prion protein: Insights from microsecond-accelerated molecular dynamics simulations. ACS chemical neuroscience 10(6):2718–2729

[207] Malevanets A, Chong PA, Hansen DF, Rizk P, Sun Y, Lin H, Muhandiram R, Chakrabartty A, Kay LE, Forman-Kay JD, et al. (2017) Interplay of buried histidine protonation and protein stability in prion misfolding. Scientific reports 7(1):1–14

[208] Baldwin AJ, Knowles TP, Tartaglia GG, Fitzpatrick AW, Devlin GL, Shammas SL, Waudby CA, Mossuto MF, Meehan S, Gras SL, et al. (2011) Metastability of native proteins and the phenomenon of amyloid formation. Journal of the American Chemical Society 133(36):14160–14163

[209] Tahiri-Alaoui A, Gill AC, Disterer P, James W (2004) Methionine 129 variant of human prion protein oligomerizes more rapidly than the valine 129 variant: implications for disease susceptibility to creutzfeldt-jakob disease. Journal of Biological Chemistry 279(30):31390–31397

[210] Eghiaian F, Daubenfeld T, Quenet Y, van Audenhaege M, Bouin AP, van der Rest G, Grosclaude J, Rezaei H (2007) Diversity in prion protein oligomerization pathways results from domain expansion as revealed by hydrogen/deuterium exchange and disulfide linkage. Proceedings of the National Academy of Sciences 104(18):7414–7419

[211] Engelke AD, Gonsberg A, Thapa S, Jung S, Ulbrich S, Seidel R, Basu S, Multhaup G, Baier M, Engelhard M, et al. (2018) Dimerization of the cellular prion protein inhibits propagation of scrapie prions. Journal of Biological Chemistry 293(21):8020–8031

[212] Rösener NS, Gremer L, Reinartz E, König A, Brener O, Heise H, Hoyer W, Neudecker P, Willbold D (2018) A d-enantiomeric peptide interferes with heteroassociation of amyloid-β oligomers and prion protein. Journal of Biological Chemistry 293(41):15748–15764

[213] Schuck P, Perugini MA, Gonzales NR, Howlett GJ, Schubert D (2002) Size-distribution analysis of proteins by analytical ultracentrifugation: strategies and application to model systems. Biophysical journal 82(2):1096–1111

[214] Abskharon RN, Giachin G, Wohlkonig A, Soror SH, Pardon E, Legname G, Steyaert J (2014) Probing the n-terminal β-sheet conversion in the crystal structure of the human prion protein bound to a nanobody. Journal of the American Chemical Society 136(3):937–944

[215] Chemical Computing Group U (2021) Molecular operating environment (moe)

[216] Honda RP, Yamaguchi Ki, Kuwata K (2014) Acid-induced molten globule state of a prion protein. Journal of Biological Chemistry 289(44):30355–30363

[217] Izadi S, Anandakrishnan R, Onufriev AV (2014) Building water models: a different approach. The journal of physical chemistry letters 5(21):3863–3871

[218] Case DA, Cheatham III TE, Darden T, Gohlke H, Luo R, Merz Jr KM, Onufriev A, Simmerling C, Wang B, Woods RJ (2005) The amber biomolecular simulation programs. Journal of computational chemistry 26(16):1668–1688

[219] Tian C, Kasavajhala K, Belfon KA, Raguette L, Huang H, Migues AN, Bickel J, Wang Y, Pincay J, Wu Q, et al. (2019) ff19sb: Amino-acid-specific protein backbone parameters trained against quantum mechanics energy surfaces in solution. Journal of chemical theory and computation 16(1):528–552

[220] Roe DR, Cheatham III TE (2013) Ptraj and cpptraj: software for processing and analysis of molecular dynamics trajectory data. Journal of chemical theory and computation 9(7):3084–3095

[221] Jacobs DJ, Rader AJ, Kuhn LA, Thorpe MF (2001) Protein flexibility predictions using graph theory. Proteins: Structure, Function, and Bioinformatics 44(2):150–165

[222] Barlow DJ, Thornton J (1983) Ion-pairs in proteins. Journal of molecular biology 168(4):867–885

[223] Ryckaert JP, Ciccotti G, Berendsen HJ (1977) Numerical integration of the cartesian equations of motion of a system with constraints: molecular dynamics of n-alkanes. Journal of computational physics 23(3):327–341

[224] Hopkins CW, Le Grand S, Walker RC, Roitberg AE (2015) Long-time-step molecular dynamics through hydrogen mass repartitioning. Journal of chemical theory and computation 11(4):1864–1874

[225] Stöhr J, Weinmann N, Wille H, Kaimann T, Nagel-Steger L, Birkmann E, Panza G, Prusiner SB, Eigen M, Riesner D (2008) Mechanisms of prion protein assembly into amyloid. Proceedings of the National Academy of Sciences 105(7):2409–2414

[226] Safar J, Roller P, Gajdusek D, Gibbs Jr C (1993) Conformational transitions, dissociation, and unfolding of scrapie amyloid (prion) protein. Journal of Biological Chemistry 268(27):20276–20284

[227] Vey M, Pilkuhn S, Wille H, Nixon R, DeArmond SJ, Smart EJ, Anderson RG, Taraboulos A, Prusiner SB (1996) Subcellular colocalization of the cellular and scrapie prion proteins in caveolae-like membranous domains. Proceedings of the National Academy of Sciences 93(25):14945–14949

[228] Resenberger UK, Harmeier A, Woerner AC, Goodman JL, Müller V, Krishnan R, Vabulas RM, Kretzschmar HA, Lindquist S, Hartl FU, et al. (2011) The cellular prion protein mediates neurotoxic signalling of β-sheet-rich conformers independent of prion replication. The EMBO journal 30(10):2057–2070

[229] Pauly T, Bolakhrif N, Kaiser J, Nagel-Steger L, Gremer L, Gohlke H, Willbold D (2022) Met/val129 polymorphism of the full-length human prion protein dictates distinct pathways of amyloid formation. Journal of Biological Chemistry 298(10)

[230] Bocharova OV, Breydo L, Parfenov AS, Salnikov VV, Baskakov IV (2005) In vitro conversion of full-length mammalian prion protein produces amyloid form with physical properties of prpsc. Journal of molecular biology 346(2):645–659

[231] Kundu B, Maiti NR, Jones EM, Surewicz KA, Vanik DL, Surewicz WK (2003) Nucleation-dependent conformational conversion of the y145stop variant of human prion protein: structural clues for prion propagation. Proceedings of the National Academy of Sciences 100(21):12069–12074

[232] Mehlhorn I, Groth D, Stöckel J, Moffat B, Reilly D, Yansura D, Willett WS, Baldwin M, Fletterick R, Cohen FE, et al. (1996) High-level expression and characterization of a purified 142-residue polypeptide of the prion protein. Biochemistry 35(17):5528–5537

[233] Riley ML, Leucht C, Gauczynski S, Hundt C, Brecelj M, Dodson G, Weiss S (2002) High-level expression and characterization of a glycosylated covalently linked dimer of the prion protein. Protein engineering 15(6):529–537

[234] Niimi T (2012) Recombinant protein production in the eukaryotic protozoan parasite leishmania tarentolae: a review. Recombinant Gene Expression pp 307–315

[235] Zhang WW, Charest H, Matlashewski G (1995) The expression of biologically active human p53 in leishmania cells: a novel eukaryotic system to produce recombinant proteins. Nucleic acids research 23(20):4073–4080

[236] La Flamme AC, Buckner FS, Swindle J, Ajioka J, Van Voorhis WC (1995) Expression of mammalian cytokines by trypanosoma cruzi indicates unique signal sequence requirements and processing. Molecular and biochemical parasitology 75(1):25–31

[237] Zhang L, Somasundaran P, Maltesh C (1996) Electrolyte effects on the surface tension and micellization of n-dodecyl β-d-maltoside solutions. Langmuir 12(10):2371–2373

[238] Rath A, Glibowicka M, Nadeau VG, Chen G, Deber CM (2009) Detergent binding explains anomalous sds-page migration of membrane proteins. Proceedings of the National Academy of Sciences 106(6):1760–1765

[239] López García F, Zahn R, Riek R, Wüthrich K (2000) Nmr structure of the bovine prion protein. Proceedings of the National Academy of Sciences 97(15):8334–8339

[240] Riek R, Hornemann S, Wider G, Billeter M, Glockshuber R, Wüthrich K (1996) Nmr structure of the mouse prion protein domain prp (121–231). Nature 382(6587):180–182

[241] Johnson Jr WC (1988) Secondary structure of proteins through circular dichroism spectroscopy. Annual review of biophysics and biophysical chemistry 17(1):145–166

[242] Zerr I, Parchi P (2018) Sporadic creutzfeldt–jakob disease. In: Handbook of clinical neurology, vol 153, Elsevier, pp 155–174

[243] Kraus A, Hoyt F, Schwartz CL, Hansen B, Hughson AG, Artikis E, Race B, Caughey B (2021) Structure of an infectious mammalian prion. bioRxiv DOI 10.1101/2021.02.14.431014,

URL https://www.biorxiv.org/content/early/2021/03/16/2021.02.14.431014,https://www.biorxiv.org/content/early/2021/03/16/2021.02.14.431014.full.pdf

[244] Hoyt F, Standke HG, Artikis E, Schwartz CL, Hansen B, Li K, Hughson AG, Manca M, Thomas OR, Raymond GJ, et al. (2022) Cryo-em structure of anchorless rml prion reveals variations in shared motifs between distinct strains. Nature communications 13(1):1–7

[245] Julien O, Chatterjee S, Bjorndahl TC, Sweeting B, Acharya S, Semenchenko V, Chakrabartty A, Pai EF, Wishart DS, Sykes BD, et al. (2011) Relative and regional stabilities of the hamster, mouse, rabbit, and bovine prion proteins toward urea unfolding assessed by nuclear magnetic resonance and circular dichroism spectroscopies. Biochemistry 50(35):7536–7545

[246] Bousset L, Luckgei N, Kabani M, Gardiennet C, Schütz AK, Melki R, Meier BH, Böckmann A (2020) Prion amyloid polymorphs–the tag might change it all. Frontiers in Molecular Biosciences 7:190

[247] Viennet T, Bungert-Plümke S, Elter S, Viegas A, Fahlke C, Etzkorn M (2019) Reconstitution and nmr characterization of the ion-channel accessory subunit barttin in detergents and lipid-bilayer nanodiscs. Frontiers in molecular biosciences 6:13

[248] Niculae A, Bayer P, Cirstea I, Bergbrede T, Pietrucha R, Gruen M, Breitling R, Alexandrov K (2006) Isotopic labeling of recombinant proteins expressed in the protozoan host leishmania tarentolae. Protein expression and purification 48(2):167–172

[249] Foldynová-Trantírková S, Matulová J, Dötsch V, Löhr F, Cirstea I, Alexandov K, Breitling R, Lukeš J, Trantírek L (2009) A cost-effective amino-acid-type selective isotope labeling of proteins expressed in leishmania tarentolae. Journal of Biomolecular Structure and Dynamics 26(6):755–761

[250] Adalsteinsson D, Schultz P (2020) Datagraph. Visual Data Tools Inc

[251] Seixas FL, Zadrozny B, Laks J, Conci A, Saade DCM (2014) A bayesian network decision model for supporting the diagnosis of dementia, alzheimer's disease and mild cognitive impairment. Computers in biology and medicine 51:140–158

[252] Selkoe DJ, Hardy J (2016) The amyloid hypothesis of alzheimer's disease at 25 years. EMBO molecular medicine 8(6):595–608

[253] Kumar K, Kumar A, Keegan RM, Deshmukh R (2018) Recent advances in the neurobiology and neuropharmacology of alzheimer's disease. Biomedicine & pharmacotherapy 98:297–307

[254] Li S, Selkoe DJ (2020) A mechanistic hypothesis for the impairment of synaptic plasticity by soluble aβ oligomers from alzheimer's brain. Journal of neurochemistry 154(6):583–597

[255] Giuffrida ML, Caraci F, Pignataro B, Cataldo S, De Bona P, Bruno V, Molinaro G, Pappalardo G, Messina A, Palmigiano A, et al. (2009) β-amyloid monomers are neuroprotective. Journal of Neuroscience 29(34):10582–10587

[256] Soscia SJ, Kirby JE, Washicosky KJ, Tucker SM, Ingelsson M, Hyman B, Burton MA, Goldstein LE, Duong S, Tanzi RE, et al. (2010) The alzheimer's disease-associated amyloid β-protein is an antimicrobial peptide. PloS one 5(3):e9505

[257] Kumar DKV, Choi SH, Washicosky KJ, Eimer WA, Tucker S, Ghofrani J, Lefkowitz A, McColl G, Goldstein LE, Tanzi RE, et al. (2016) Amyloid-β peptide protects against microbial infection in mouse and worm models of alzheimer's disease. Science translational medicine 8(340):340ra72–340ra72

[258] Gosztyla ML, Brothers HM, Robinson SR (2018) Alzheimer's amyloid-β is an antimicrobial peptide: A review of the evidence. Journal of Alzheimer's Disease 62(4):1495–1506

[259] Zhou R, Yang G, Guo X, Zhou Q, Lei J, Shi Y (2019) Recognition of the amyloid precursor protein by human γ-secretase. Science 363(6428):eaaw0930

[260] Deyts C, Thinakaran G, Parent AT (2016) App receptor? to be or not to be. Trends in pharmacological sciences 37(5):390–411

[261] Hunter S, Brayne C (2018) Understanding the roles of mutations in the amyloid precursor protein in alzheimer disease. Molecular psychiatry 23(1):81–93

[262] Langosch D, Scharnagl C, Steiner H, Lemberg M (2015) Understanding intramembrane proteolysis: from protein dynamics to reaction kinetics. Trends in biochemical sciences 40(6):318–327

[263] Tang TC, Hu Y, Kienlen-Campard P, El Haylani L, Decock M, Van Hees J, Fu Z, Octave JN, Constantinescu SN, Smith SO (2014) Conformational changes induced by the a21g flemish mutation in the amyloid precursor protein lead to increased aβ production. Structure 22(3):387–396

[264] Chen W, Gamache E, Rosenman DJ, Xie J, Lopez MM, Li YM, Wang C (2014) Familial alzheimer's mutations within apptm increase aβ42 production by enhancing accessibility of ε-cleavage site. Nature communications 5(1):1–7

[265] Polshakov VI, Mantsyzov AB, Kozin SA, Adzhubei AA, Zhokhov SS, van Beek W, Kulikova AA, Indeykina MI, Mitkevich VA, Makarov AA (2017) A binuclear zinc interaction fold discovered in the homodimer of alzheimer's amyloid-β fragment with taiwanese mutation d7h. Angewandte Chemie 129(39):11896–11901

[266] Götz A, Högel P, Silber M, Chaitoglou I, Luy B, Muhle-Goll C, Scharnagl C, Langosch D (2019) Increased h-bond stability relates to altered ε-cleavage efficiency and aβ levels in the i45t familial alzheimer's disease mutant of app. Scientific reports 9(1):1–12

[267] Bocharov EV, Nadezhdin KD, Urban AS, Volynsky PE, Pavlov KV, Efremov RG, Arseniev AS, Bocharova OV (2019) Familial l723p mutation can shift the distribution between the alternative app transmembrane domain cleavage cascades by local unfolding of the e-cleavage site suggesting a straightforward mechanism of alzheimer's disease pathogenesis. ACS Chemical Biology 14(7):1573–1582

[268] Citron M (2010) Alzheimer's disease: strategies for disease modification. Nature reviews Drug discovery 9(5):387–398

[269] Sun N, A Funke S, Willbold D (2012) A survey of peptides with effective therapeutic potential in alzheimer's disease rodent models or in human clinical studies. Mini reviews in medicinal chemistry 12(5):388–398

[270] Schenk D, Basi GS, Pangalos MN (2012) Treatment strategies targeting amyloid β-protein. Cold Spring Harbor perspectives in medicine 2(9):a006387

[271] Chen Y, Fu AK, Ip NY (2019) Synaptic dysfunction in alzheimer's disease: Mechanisms and therapeutic strategies. Pharmacology & therapeutics 195:186–198

[272] Sabbagh MN (2020) Alzheimer's disease drug development pipeline 2020

[273] Heller GT, Aprile FA, Michaels TC, Limbocker R, Perni M, Ruggeri FS, Mannini B, Löhr T, Bonomi M, Camilloni C, et al. (2020) Small-molecule sequestration of amyloid-β as a drug discovery strategy for alzheimer's disease. Science advances 6(45):eabb5924

[274] Xie J, Liang R, Wang Y, Huang J, Cao X, Niu B (2020) Progress in target drug molecules for alzheimer's disease. Current Topics in Medicinal Chemistry 20(1):4–36

[275] Elfgen A, Hupert M, Bochinsky K, Tusche M, González de San Román Martin E, Gering I, Sacchi S, Pollegioni L, Huesgen PF, Hartmann R, et al. (2019) Metabolic resistance of the d-peptide rd2 developed for direct elimination of amyloid-β oligomers. Scientific reports 9(1):1–13

[276] Elfgen A, Hupert M, Bochinsky K, Tusche M, González de San Román Martin E, Gering I, Sacchi S, Pollegioni L, Huesgen PF, Hartmann R, et al. (2019) Metabolic resistance of the d-peptide rd2 developed for direct elimination of amyloid-β oligomers. Scientific reports 9(1):1–13

[277] Zhao Y, Zhang M, Qiu S, Wang J, Peng J, Zhao P, Zhu R, Wang H, Li Y, Wang K, et al. (2016) Antimicrobial activity and stability of the d-amino acid substituted derivatives of antimicrobial peptide polybia-mpi. AMB Express 6(1):1–11

[278] Uppalapati M, Lee DJ, Mandal K, Li H, Miranda LP, Lowitz J, Kenney J, Adams JJ, Ault-Riché D, Kent SB, et al. (2016) A potent d-protein antagonist of vegf-a is nonimmunogenic, metabolically stable, and longer-circulating in vivo. ACS chemical biology 11(4):1058–1065

[279] Van Groen T, Wiesehan K, Funke SA, Kadish I, Nagel-Steger L, Willbold D (2008) Reduction of alzheimer's disease amyloid plaque load in transgenic mice by d3, ad-enantiomeric peptide identified by mirror image phage display. ChemMedChem: Chemistry Enabling Drug Discovery 3(12):1848–1852

[280] Brener O, Dunkelmann T, Gremer L, Van Groen T, Mirecka EA, Kadish I, Willuweit A, Kutzsche J, Jürgens D, Rudolph S, et al. (2015) Qiad assay for quantitating a compound's efficacy in elimination of toxic aβ oligomers. Scientific reports 5(1):1–13

[281] Funke SA, van Groen T, Kadish I, Bartnik D, Nagel-Steger L, Brener O, Sehl T, Batra-Safferling R, Moriscot C, Schoehn G, et al. (2010) Oral treatment with the d-enantiomeric peptide d3 improves the pathology and behavior of alzheimer's disease transgenic mice. ACS chemical neuroscience 1(9):639–648

[282] Jiang N, Leithold LH, Post J, Ziehm T, Mauler J, Gremer L, Cremer M, Schartmann E, Shah NJ, Kutzsche J, et al. (2015) Preclinical pharmacokinetic studies of the tritium labelled d-enantiomeric peptide d3 developed for the treatment of alzheimer s disease. PloS one 10(6):e0128553

[283] Hellstrand E, Boland B, Walsh DM, Linse S (2010) Amyloid β-protein aggregation produces highly reproducible kinetic data and occurs by a two-phase process. ACS chemical neuroscience 1(1):13–18

[284] Friedemann M, Helk E, Tiiman A, Zovo K, Palumaa P, Tõugu V (2015) Effect of methionine-35 oxidation on the aggregation of amyloid-β peptide. Biochemistry and biophysics reports 3:94–99

[285] Nirmalraj PN, List J, Battacharya S, Howe G, Xu L, Thompson D, Mayer M (2020) Complete aggregation pathway of amyloid β (1-40) and (1-42) resolved on an atomically clean interface. Science advances 6(15):eaaz6014

[286] Bocharov EV, Gremer L, Urban AS, Okhrimenko IS, Volynsky PE, Nadezhdin KD, Bocharova OV, Kornilov DA, Zagryadskaya YA, Kamynina AV, et al. (2021) All-d-enantiomeric peptide d3 designed for alzheimer's disease treatment dynamically interacts with membrane-bound amyloid-β precursors. Journal of Medicinal Chemistry 64(22):16464–16479

[287] Barrett PJ, Song Y, Van Horn WD, Hustedt EJ, Schafer JM, Hadziselimovic A, Beel AJ, Sanders CR (2012) The amyloid precursor protein has a flexible transmembrane domain and binds cholesterol. Science 336(6085):1168–1171

[288] Hu Y, Kienlen-Campard P, Tang TC, Perrin F, Opsomer R, Decock M, Pan X, Octave JN, Constantinescu SN, Smith SO (2017) β-sheet structure within the extracellular domain of c99 regulates amyloidogenic processing. Scientific reports 7(1):1–11

[289] Pantelopulos GA, Straub JE, Thirumalai D, Sugita Y (2018) Structure of app-c991–99 and implications for role of extra-membrane domains in function and oligomerization. Biochimica et Biophysica Acta (BBA)-Biomembranes 1860(9):1698–1708

[290] Bocharova O, Urban A, Nadezhdin K, Bocharov E, Arseniev A (2013) Bacterial and cell-free production of app671-726 containing amyloid precursor protein transmembrane and metal-binding domains. Biochemistry (Moscow) 78(11):1263–1271

[291] Bocharova OV, Urban AS, Nadezhdin KD, Bocharov EV, Arseniev AS (2016) Cell-free expression of the app transmembrane fragments with alzheimer's disease mutations using algal amino acid mixture for structural nmr studies. Protein Expression and Purification 123:105–111

[292] Zhang T, Loschwitz J, Strodel B, Nagel-Steger L, Willbold D (2019) Interference with amyloid-β nucleation by transient ligand interaction. Molecules 24(11):2129

[293] Battiste JL, Wagner G (2000) Utilization of site-directed spin labeling and high-resolution heteronuclear nuclear magnetic resonance for global fold determination of large proteins with limited nuclear overhauser effect data. Biochemistry 39(18):5355–5365

[294] Williamson MP (2013) Using chemical shift perturbation to characterise ligand binding. Progress in nuclear magnetic resonance spectroscopy 73:1–16

[295] Tjernberg LO, Näslund J, Lindqvist F, Johansson J, Karlström AR, Thyberg J, Terenius L, Nordstedt C (1996) Arrest of-amyloid fibril formation by a pentapeptide ligand. Journal of Biological Chemistry 271(15):8545–8548

[296] Robinson M, Lee BY, Leonenko Z (2005) Drugs and drug delivery systems targeting amyloid-β in alzheimer's. AIMS Molecular Science

[297] Uversky VN (2015) The multifaceted roles of intrinsic disorder in protein complexes. FEBS letters 589(19):2498–2506

[298] Borgia A, Borgia MB, Bugge K, Kissling VM, Heidarsson PO, Fernandes CB, Sottini A, Soranno A, Buholzer KJ, Nettels D, et al. (2018) Extreme disorder in an ultrahigh-affinity protein complex. Nature 555(7694):61–66

[299] Prestel A, Bugge K, Staby L, Hendus-Altenburger R, Kragelund BB (2018) Characterization of dynamic idp complexes by nmr spectroscopy. In: Methods in enzymology, vol 611, Elsevier, pp 193–226

[300] Puchtler H, Sweat F (1965) Congo red as a stain for fluorescence microscopy of amyloid. J Histochem Cytochem 13(8):693–4, DOI 10.1177/13.8.693, URL https://www.ncbi.nlm.nih.gov/pubmed/4160077

[301] Bocharov EV, Mayzel ML, Volynsky PE, Mineev KS, Tkach EN, Ermolyuk YS, Schulga AA, Efremov RG, Arseniev AS (2010) Left-handed dimer of epha2 transmembrane domain: helix packing diversity among receptor tyrosine kinases. Biophysical journal 98(5):881–889

[302] Grimm MO, Mett J, Grimm HS, Hartmann T (2017) App function and lipids: a bidirectional link. Frontiers in molecular neuroscience 10:63

[303] Klein AN, Ziehm T, van Groen T, Kadish I, Elfgen A, Tusche M, Thomaier M, Reiss K, Brener O, Gremer L, et al. (2017) Optimization of d-peptides for aβ monomer binding specificity enhances their potential to eliminate toxic aβ oligomers. ACS chemical neuroscience 8(9):1889–1900

[304] Ziehm T, Buell AK, Willbold D (2018) Role of hydrophobicity and charge of amyloid-beta oligomer eliminating d-peptides in the interaction with amyloid-beta monomers. ACS chemical neuroscience 9(11):2679–2688

[305] Kutzsche J, Jürgens D, Willuweit A, Adermann K, Fuchs C, Simons S, Windisch M, Hümpel M, Rossberg W, Wolzt M, et al. (2020) Safety and pharmacokinetics of the orally available antiprionic compound pri-002: A single and multiple ascending dose phase i study. Alzheimer's & Dementia: Translational Research & Clinical Interventions 6(1):e12001

[306] Ciudad S, Puig E, Botzanowski T, Meigooni M, Arango AS, Do J, Mayzel M, Bayoumi M, Chaignepain S, Maglia G, et al. (2020) Aβ (1-42) tetramer and octamer structures reveal edge conductivity pores as a mechanism for membrane damage. Nature communications 11(1):1–14

[307] Nadezhdin KD, Bocharova OV, Bocharov EV, Arseniev AS (2012) Dimeric structure of transmembrane domain of amyloid precursor protein in micellar environment. FEBS letters 586(12):1687–1692

[308] Cavini IA, Munte CE, Erlach MB, van Groen T, Kadish I, Zhang T, Ziehm T, Nagel-Steger L, Kutzsche J, Kremer W, et al. (2018) Inhibition of amyloid aβ aggregation by high pressures or specific d-enantiomeric peptides. Chemical communications 54(26):3294–3297

[309] Sreerama N, Woody RW (2000) Estimation of protein secondary structure from circular dichroism spectra: comparison of contin, selcon, and cdsstr methods with an expanded reference set. Analytical biochemistry 287(2):252–260

[310] Keller RL (2004) Cantina verlag. The computer aided resonance assignment tutorial

[311] Cavanagh J, Fairbrother WJ, Palmer III AG, Skelton NJ (1996) Protein NMR spectroscopy: principles and practice. Academic press

[312] Kazimierczuk K, Orekhov VY (2012) A comparison of convex and non-convex compressed sensing applied to multidimensional nmr. Journal of magnetic resonance 223:1–10

[313] Favier A, Brutscher B (2011) Recovering lost magnetization: polarization enhancement in biomolecular nmr. Journal of biomolecular NMR 49(1):9–15

[314] Abraham MJ, Murtola T, Schulz R, Páll S, Smith JC, Hess B, Lindahl E (2015) Gromacs: High performance molecular simulations through multi-level parallelism from laptops to supercomputers. SoftwareX 1:19–25

[315] Lindorff-Larsen K, Piana S, Palmo K, Maragakis P, Klepeis JL, Dror RO, Shaw DE (2010) Improved side-chain torsion potentials for the amber ff99sb protein force field. Proteins: Structure, Function, and Bioinformatics 78(8):1950–1958

[316] Jorgensen WL, Chandrasekhar J, Madura JD, Impey RW, Klein ML (1983) Comparison of simple potential functions for simulating liquid water. The Journal of chemical physics 79(2):926–935

[317] Jaembeck JP, Lyubartsev AP (2012) Derivation and systematic validation of a refined all-atom force field for phosphatidylcholine lipids. The journal of physical chemistry B 116(10):3164–3179

[318] Zirah S, Kozin SA, Mazur AK, Blond A, Cheminant M, Ségalas-Milazzo I, Debey P, Rebuffat S (2006) Structural changes of region 1-16 of the alzheimer disease amyloid β-peptide upon zinc binding and in vitro aging. Journal of Biological Chemistry 281(4):2151–2161

[319] Glynn C, Sawaya MR, Ge P, Gallagher-Jones M, Short CW, Bowman R, Apostol M, Zhou ZH, Eisenberg DS, Rodriguez JA (2020) Cryo-em structure of a human prion fibril with a hydrophobic, protease-resistant core. Nature structural & molecular biology 27(5):417–423

[320] Gallagher-Jones M, Glynn C, Boyer DR, Martynowycz MW, Hernandez E, Miao J, Zee CT, Novikova IV, Goldschmidt L, McFarlane HT, et al. (2018) Sub-ångström cryo-em structure of a prion protofibril reveals a polar clasp. Nature structural & molecular biology 25(2):131–134

[321] Cobb NJ, Sönnichsen FD, Mchaourab H, Surewicz WK (2007) Molecular architecture of human prion protein amyloid: A parallel, in-register β-structure. Proceedings of the National Academy of Sciences 104(48):18946–18951

[322] Spagnolli G, Rigoli M, Orioli S, Sevillano AM, Faccioli P, Wille H, Biasini E, Requena JR (2019) Full atomistic model of prion structure and conversion. PLoS pathogens 15(7):e1007864

[323] Cobb NJ, Apetri AC, Surewicz WK (2008) Prion protein amyloid formation under native-like conditions involves refolding of the c-terminal α-helical domain. Journal of Biological Chemistry 283(50):34704–34711

[324] Lu X, Wintrode PL, Surewicz WK (2007) β-sheet core of human prion protein amyloid fibrils as determined by hydrogen/deuterium exchange. Proceedings of the National Academy of Sciences 104(5):1510–1515

[325] Apetri AC, Vanik DL, Surewicz WK (2005) Polymorphism at residue 129 modulates the conformational conversion of the d178n variant of human prion protein 90- 231. Biochemistry 44(48):15880–15888

[326] Edwards AM, Arrowsmith CH, Christendat D, Dharamsi A, Friesen JD, Greenblatt JF, Vedadi M (2000) Protein production: feeding the crystallographers and nmr spectroscopists. nature structural biology 7(11):970–972

[327] Krassner SM, Flory B (1971) Essential amino acids in the culture of leishmania tarentolae. The Journal of Parasitology pp 917–920